NCAR | National Center for
UCAR | Atmospheric Research

A Description of the Advanced Research WRF Model Version 4

William C. Skamarock
Joseph B. Klemp
Jimy Dudhia
David O. Gill
Zhiquan Liu
Judith Berner
Wei Wang
Jordan G. Powers
Michael G. Duda
Dale M. Barker
Xiang-Yu Huang

NCAR Technical Notes
NCAR/TN-556+STR

National Center for
Atmospheric Research
P. O. Box 3000
Boulder, Colorado
80307-3000
www.ucar.edu

National Science Foundation
NCAR IS SPONSORED BY THE NSF

NCAR TECHNICAL NOTES

http://library.ucar.edu/research/publish-technote

The Technical Notes series provides an outlet for a variety of NCAR Manuscripts that contribute in specialized ways to the body of scientific knowledge but that are not yet at a point of a formal journal, monograph or book publication. Reports in this series are issued by the NCAR scientific divisions, serviced by OpenSky and operated through the NCAR Library. Designation symbols for the series include:

EDD – Engineering, Design, or Development Reports
Equipment descriptions, test results, instrumentation, and operating and maintenance manuals.

IA – Instructional Aids
Instruction manuals, bibliographies, film supplements, and other research or instructional aids.

PPR – Program Progress Reports
Field program reports, interim and working reports, survey reports, and plans for experiments.

PROC – Proceedings
Documentation or symposia, colloquia, conferences, workshops, and lectures. (Distribution maybe limited to attendees).

STR – Scientific and Technical Reports
Data compilations, theoretical and numerical investigations, and experimental results.

National Center for Atmospheric Research
P. O. Box 3000
Boulder, Colorado 80307-3000

NCAR/TN–556+STR
NCAR TECHNICAL NOTE
July 2021

A Description of the Advanced Research WRF Model Version 4

William C. Skamarock
Joseph B. Klemp
Jimy Dudhia
David O. Gill
Zhiquan Liu
Judith Berner
Wei Wang
Jordan G. Powers
Michael G. Duda
Dale M. Barker
Xiang-Yu Huang

Mesoscale and Microscale Meteorology Laboratory
National Center for Atmospheric Research
Boulder, Colorado, USA

Contents

List of Figures

List of Tables

Preface

The Advanced Research WRF (ARW) model is a configuration of the Weather Research and Forecasting (WRF) model. This technical note describes the scientific and algorithmic approaches in the ARW Version 4, including its dynamical solver, physics options, initialization capabilities, boundary conditions, grid-nesting techniques, and data assimilation capabilities. ARW is supported as a community model by the National Center for Atmospheric Research, facilitating system development and broad use for research, operations, and education. The modeling system supports atmospheric simulations across scales from large-eddy to global. ARW's applications include real-time NWP, weather events and atmospheric-process studies, data assimilation development, parameterized-physics development, regional climate simulation, air quality modeling, atmosphere-ocean coupling, and idealized- atmosphere studies.

This particular version of the Tech Note covers ARW releases up to Version 4.3. This document will be updated as new releases become available and new features are added to the model.

Acknowledgments

The Advanced Research WRF (ARW) Model is a community atmospheric modeling system, and its development and capabilities are the result of the contributions of a host of individuals and institutions from over the years. The features in ARW Version 4 stem from this generous and collaborative approach and offer the community a state-of-the-art numerical weather prediction model reflecting advancements in meteorology, computational science, and data assimilation. Many people have worked on and provided features and improvements for this latest version, particularly in the areas of physics and dynamics, and the authors thank them for their contributions.

The effort to support and maintain ARW is led by the National Center for Atmospheric Research (NCAR), which is primarily supported by the National Science Foundation (NSF). The authors sincerely thank NCAR and NSF for their support of the ARW effort. During the development of Version 4, support in various forms has also been provided by: the National Oceanic and Atmospheric Administration, the U.S. Department of Defense, the Federal Aviation Administration, the U.S. Department of Energy, and the Central Weather Bureau of Taiwan.

Lastly, the authors would like to thank the following individuals for their careful review of this document: George Bryan, Jonathan J. Guerrette, Kevin Manning, Hugh Morrison, Ned Patton, Brian Reen, Juanzhen Sun, Kelly Werner, and May Wong.

Chapter 1

Introduction

The Weather Research and Forecasting (WRF) Model is an atmospheric modeling system designed for both research and numerical weather prediction. WRF is an open-source community model, and it has been adopted for research at universities and governmental laboratories, for operational forecasting by governmental and private entities, and for commercial applications by industry. WRF development began in the latter half of the 1990's with the goals being to build a system shared by research and operations and to create a next-generation numerical weather prediction (NWP) capability. The new modeling system has become a common platform on which the broad research community can develop capabilities that can transition to operations, while the extra scrutiny of performance in operations could guide and accelerate development. The WRF system was developed through a partnership of the National Center for Atmospheric Research (NCAR), the National Oceanic and Atmospheric Administration (NOAA) (represented by the National Centers for Environmental Prediction (NCEP) and the NOAA Earth System Research Laboratory (ESRL)), the United States Air Force, the Naval Research Laboratory, the University of Oklahoma, and the Federal Aviation Administration. For more information on the history of the WRF model development see Powers et al. (2017).

1.1 Advanced Research WRF (ARW)

ARW is a configuration of the WRF system featuring the ARW dynamics solver together with other compatible components to produce a simulation. Thus, it is a subset of the WRF system that, in addition to the specific solver, encompasses physics schemes, numerics/dynamics options, initialization routines, and a data assimilation package (WRFDA). ARW consists of flexible, modular, portable code that is efficient in computing environments ranging from laptops to massively-parallel supercomputers and is readily-configurable for a variety of applications. Its extensive menu of options for physical process schemes and for configuring numerics reflect a history of community input and make it a powerful NWP tool. WRFDA offers a variety of data assimilation approaches and that can ingest a broad array of observation types. In addition, for earth system prediction needs beyond basic weather forecasting, ARW supports a number of tailored capabilities, including WRF-Chem (atmospheric chemistry), WRF-Hydro (hydrological modeling), and WRF-Fire (wildland fire modeling).

ARW is supported as a community model, facilitating system development and broad use for research, operations, and education. It supports atmospheric simulations across scales

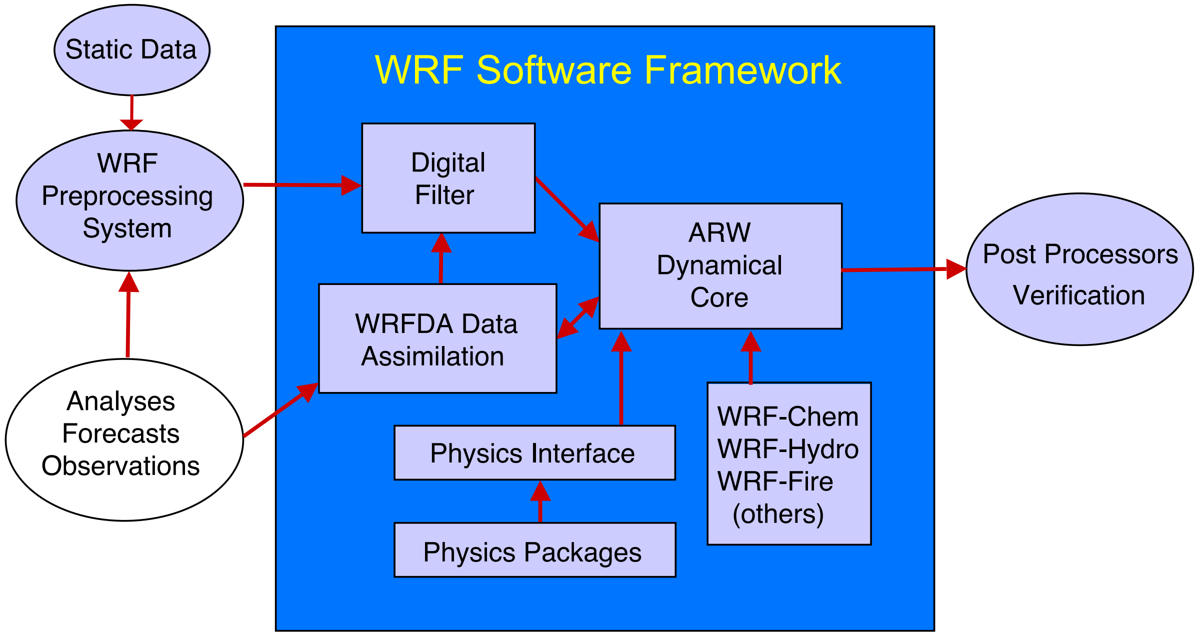

Figure 1.1: Advanced Research WRF system components.

from large-eddy to global. ARW's applications include real-time NWP, weather events and atmospheric-process studies, data assimilation development, parameterized-physics development, regional climate simulation, air quality modeling, atmosphere-ocean coupling, and idealized-atmosphere studies.

Figure 1.1 depicts the principal components of the ARW system. The WRF Software Framework (WSF) is the infrastructure that contains the dynamics solver, physics packages, utilities for initialization, WRFDA, and integrated capabilities such as WRF-Chem, WRF-Hydro, WRF-Fire, etc. The WSF also contains the NMM-E dynamics solver, which is used by NCEP in the operational HWRF model. The Mesoscale and Microscale Meteorology Laboratory of NCAR provides support for the ARW, and oversees the WRF repository and releases.

This technical note focuses on the scientific and algorithmic approaches in the ARW Version 4, including its dynamical solver, physics options, initialization capabilities, boundary conditions, and grid-nesting techniques. The WSF provides the software infrastructure, although this infrastructure is not reviewed in this technical note. Additionally, while WRF-Chem, WRF-Hydro, WRF-Fire, and other tailored systems use the ARW solver, they are also not covered by this technical note. For information on actually running the ARW system, the ARW Version 4 Modeling System User's Guide covers model operation

(http://www2.mmm.ucar.edu/wrf/users/docs/user_guide_V4/WRFUsersGuide.pdf).

The following section highlights the major features of the ARW Version 4, first released in May 2018.

1.2 Major Features of the ARW System, Version 4

ARW Dynamics Solver

- *Equations:* Fully-compressible, Eulerian nonhydrostatic equations solver with a run-time hydrostatic option available. Conserves dry air mass and scalar mass.
- *Prognostic Variables:* Velocity components u and v in Cartesian coordinate, vertical velocity w, perturbation moist potential temperature, perturbation geopotential, and perturbation dry-air surface pressure. Optionally, turbulent kinetic energy and any number of scalars such as water vapor mixing ratio, rain/snow mixing ratio, cloud water/ice mixing ratio, and chemical species and tracers.
- *Vertical Coordinate:* Terrain-following, mass-based, hybrid sigma-pressure vertical coordinate based on dry hydrostatic presure, with vertical grid stretching permitted. Top of the model is a constant pressure surface.
- *Horizontal Grid:* Arakawa C-grid staggering.
- *Time Integration:* Time-split integration using a 2nd- or 3rd-order Runge-Kutta scheme with smaller time step for acoustic and gravity-wave modes. Variable time step capability.
- *Spatial Discretization:* 2nd- to 6th-order advection options in horizontal and vertical.
- *Turbulent Mixing and Model Filters:* Sub-grid scale turbulence formulation in both coordinate and physical space. Divergence damping, external-mode filtering, vertically implicit acoustic step off-centering. Explicit filter option.
- *Initial Conditions:* Three dimensional for real-data, and one-, two- and three-dimensional for idealized data. Digital filtering initialization (DFI) capability available (real-data cases).
- *Lateral Boundary Conditions:* Periodic, open, symmetric, and specified options available.
- *Top Boundary Conditions:* Gravity wave absorbing (diffusion, Rayleigh damping, or implicit Rayleigh damping for vertical velocity). Constant pressure level at top boundary along a material surface. Rigid lid option.
- *Bottom Boundary Conditions:* Frictional or free-slip.
- *Earth's Rotation:* Full Coriolis terms included.
- *Mapping to Sphere:* Four map projections are supported for real-data simulation: polar stereographic, Lambert conformal, Mercator, and latitude-longitude (allowing rotated pole). Curvature terms included.
- *Nesting:* One-way interactive, two-way interactive, and moving nests. Multiple levels and integer ratios.
- *Nudging:* Grid, spectral, and observation nudging capabilities.
- *Global Grid:* Global simulation capability using polar Fourier filter and periodic east-west conditions.
- *Tropical Channel:* Tropical channel capability using periodic east-west and specified north-south lateral boundary conditions.

Model Physics

- *Microphysics:* Schemes ranging from simplified physics suitable for idealized studies to mixed-phase, multi-moment, bin, and aerosol-aware approaches to support process studies and accurate NWP.

- *Cumulus parameterizations:* Deep and shallow convection, adjustment, mass-flux, and scale-aware schemes available.
- *Surface physics:* Multi-layer land surface models ranging from a simple thermal model to full vegetation and soil moisture models, including snow cover and sea ice. Urban parameterizations are available.
- *Planetary boundary layer physics:* Turbulent kinetic energy prediction or non-local K schemes.
- *Atmospheric radiation physics:* Longwave and shortwave schemes with multiple spectral bands and a simple shortwave scheme suitable for climate and weather applications. Cloud effects and surface fluxes are included.

WRFDA System

- Data assimilation capability merged into WRF software framework.
- WRFPlus code (i.e., tangent linear and adjoint versions of WRF) integrated into WRF software package.
- Incremental formulation of the model-space cost function.
- Quasi-Newton or conjugate gradient minimization algorithms.
- Analysis increments on unstaggered Arakawa-A grid.
- Representation of the horizontal component of background error **B** via recursive filters (regional) or power spectra (global). The vertical component is applied through projection onto climatologically-averaged eigenvectors of vertical error. Horizontal/vertical errors are non-separable (horizontal scales vary with vertical eigenvector).
- Background cost function (J_b) preconditioning via a control variable transform U defined as $\mathbf{B} = \mathrm{U}\mathrm{U}^T$.
- Flexible choice of background error model and control variables.
- Background error covariances estimated via either the NMC-method of averaged forecast differences or suitably-averaged ensemble perturbations.
- 3DVAR, 4DVAR, hybrid-3DEnVar, and hybrid-4DEnVar approaches available for deterministic analysis.
- Capability of running hybrid-3D/4DEnVar with a dual-resolution setting (i.e., ensemble input at a lower resolution than that of deterministic background and analysis).
- Capability of computing forecast sensitivity to observations (FSO).
- Ensemble Transform Kalman Filter (ETKF) and ensemble of hybrid-EnVar with perturbed observations for ensemble analysis.
- Flexible choice of observation ingestion from research and operational data sources.
- Two options of fast radiative transfer model (CRTM and RTTOV) for satellite radiance data assiimilation.
- Capability of assimilating all-sky satellite radiance data.
- Multiple options of assimilating radar observations.

WRF Software Framework

- Highly modular, single-source code for maintainability.
- Two-level domain decomposition for distributed- and shared-memory parallel computation.

- Portable across a range of available computing platforms.
- Support for multiple physics modules.
- Separation of scientific codes from parallelization and other architecture-specific aspects.
- Input/output Application Program Interface (API) enabling various external packages to be installed with WRF, thus allowing WRF to easily support various data formats.
- Efficient execution on a range of computing platforms (distributed and shared memory, vector and scalar types).

WRF-Chem, WRF-Hydro and WRF-Fire

WRF-Chem is a full online atmospheric chemistry model with many options and some interactions with the physics via aerosols affecting radiation and microphysics when appropriate options are chosen. Typically it requires emission source maps as additional inputs. Further information on WRF-Chem can be found at https://ruc.noaa.gov/wrf/wrf-chem/

WRF-Hydro is a surface hydrological model that can be run online with WRF or offline, interacting with WRF through the land-surface model. This model can calculate the land water budget terms including streamflow given additional data for routing. It operates on a higher-resolution sub-grid relative to the atmospheric model. Further information on WRF-Hydro can be found at https://ral.ucar.edu/projects/wrf_hydro/overview

WRF-Fire operates as a coupled wildland fire model that keeps track of a fire front at the sub-grid level. It interacts with the model via winds and heat fluxes and requires fuel information as an additional input. Further information concerning WRF-Fire can be found at http://www2.mmm.ucar.edu/wrf/users/fire/wrf-fire.html and in the ARW Users Guide at http://www2.mmm.ucar.edu/wrf/users/docs/user_guide_v4/contents.html

Additionally, a brief description of these components, along with references to further information, can by found in Powers et al. (2017).

Chapter 2

Governing Equations

The ARW dynamics solver integrates the compressible, nonhydrostatic Euler equations. The equations are cast in flux form using variables that have conservation properties, following the philosophy of Ooyama (1990). The equations are formulated using hydrostatic pressure as an independent variable (Laprise, 1992). The vertical coordinate is terrain following, using a hybrid $\sigma - p$ formulation. In this chapter we define the vertical coordinate, present the moist flux-form equations in Cartesian space, and augment the equations to include projections to the sphere.

2.1 Vertical Coordinate and Flux-Form Variables

The ARW equations are formulated using a terrain-following hydrostatic-pressure vertical coordinate denoted by η, which is also referred to a mass vertical coordinate. In previous versions of the ARW, η was defined as

$$\eta = \frac{p_d - p_t}{p_s - p_t}, \tag{2.1}$$

where p_d is the hydrostatic component of the pressure of dry air, and p_s and p_t refer to values of p_d along the surface and top boundaries, respectively. The coordinate definition (2.1), proposed by Laprise (1992) for use with the nonhydrostatic equations, is the traditional sigma coordinate used in many hydrostatic atmospheric models. η varies from a value of 1 at the surface to 0 at the upper boundary of the model domain (Fig. 2.1a).

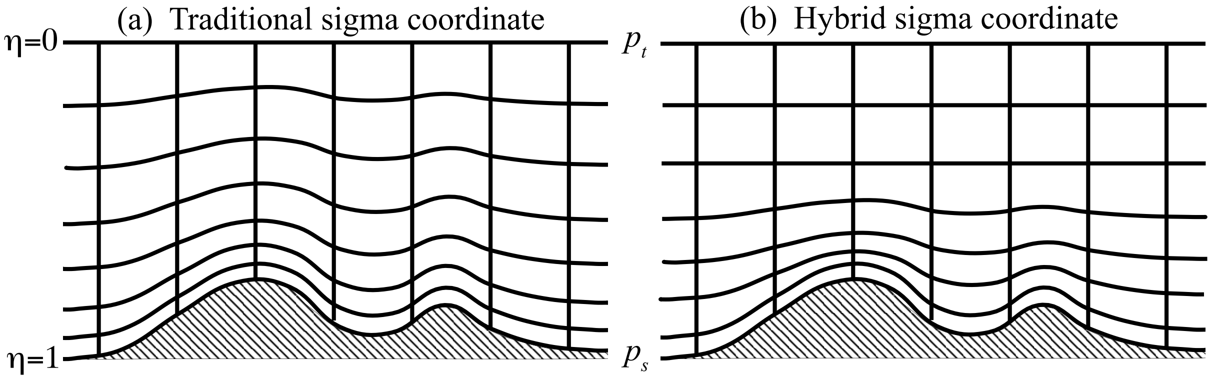

Figure 2.1: ARW η coordinate.

In the ARW Version, 4 the vertical coordinate has been generalized to allow the influence of the terrain on the coordinate surfaces to be removed more rapidly with increasing height above the surface, as illustrated in Fig. 2.1b. For this modified vertical coordinate, we employ a hybrid sigma-pressure vertical coordinate as described by Park et al. (2013), which is similar to that used in the National Center for Atmospheric Research (NCAR) Community Atmospheric Model (CAM),as described in the NCAR CAM3.0 Technical Note:

$$p_d = B(\eta)(p_s - p_t) + [\eta - B(\eta)](p_0 - p_t) + p_t, \tag{2.2}$$

where p_0 is a reference sea-level pressure. (This coordinate representation differs somewhat from CAM in that it is based on dry pressure instead of full pressure and is normalized using p_t such that $\eta = 0$ at $p_d = p_t$.) Here, $B(\eta)$ defines the relative weighting between the terrain-following sigma coordinate and a pure pressure coordinate, such that η corresponds to the sigma coordinate (2.1) for $B(\eta) = \eta$ and reverts to a hydrostatic pressure coordinate for $B(\eta) = 0$. To smoothly transition from a sigma coordinate near the surface to a pressure coordinate at upper levels, $B(\eta)$ is defined by a third order polynomial

$$B(\eta) = c_1 + c_2\eta + c_3\eta^2 + c_4\eta^3 \tag{2.3}$$

(where the subscript η denotes differentiation) subject to the boundary conditions

$$B(1) = 1, \quad B_\eta(1) = 1, \quad B(\eta_c) = 0, \quad B_\eta(\eta_c) = 0, \tag{2.4}$$

such that

$$c_1 = \frac{2\eta_c^2}{(1-\eta_c)^3}, \quad c_2 = \frac{-\eta_c(4+\eta_c+\eta_c^2)}{(1-\eta_c)^3}, \quad c_3 = \frac{2(1+\eta_c+\eta_c^2)}{(1-\eta_c)^3}, \quad c_4 = \frac{-(1+\eta_c)}{(1-\eta_c)^3}, \tag{2.5}$$

where η_c is a specified value of η at which it becomes a pure pressure coordinate.

Figure 2.2 displays the $B(\eta)$ profiles for the traditional sigma coordinate and for the hybrid coordinate for several values of the parameter η_c. Plotted as a function of η (Fig. 2.2a), these profiles depict the form of the polynomial defined in (2.3). However, plotting $B(\eta)$ as a function of height (Fig. 2.2b) provides a better physical sense of the transition toward a pressure coordinate with increasing height. For example, with a model domain having a depth of 30 km, for $\eta_c = 0.2$ the vertical coordinate becomes a pure pressure coordinate at an altitude of about 12 km.

The vertical coordinate metric is defined as

$$\mu_d = \frac{\partial p_d}{\partial \eta} = B_\eta(\eta)(p_s - p_t) + [1 - B_\eta(\eta)](p_0 - p_t). \tag{2.6}$$

Since $\mu_d \Delta\eta = \Delta p_d = -g\rho_d \Delta z$ is proportional to the mass per unit area within a grid cell, the appropriate flux forms for the prognostic variables are defined as

$$\mathbf{V} = \mu_d \mathbf{v} = (U, V, W), \qquad \Omega = \mu_d \omega, \qquad \Theta_m = \mu_d \theta_m, \qquad Q_m = \mu_d q_m. \tag{2.7}$$

Here, $\mathbf{v} = (u, v, w)$ are the covariant velocities in the horizontal and vertical directions, while $\omega = \dot{\eta}$ is the contravariant 'vertical' velocity. $\theta_m = \theta(1 + (R_v/R_d)q_v) \approx \theta(1 + 1.61q_v)$ is the moist potential temperature and $Q_m = \mu_d q_m$, where $q_m = q_v, q_c, q_r...$ represents the mixing ratios of moisture variables (water vapor, cloud water, rain water, ...). Although the geopotential $\phi = gz$ is also a prognostic variable in the governing equations of the ARW, it is not written in flux-form as $\mu_d \phi$ is not a conserved quantity.

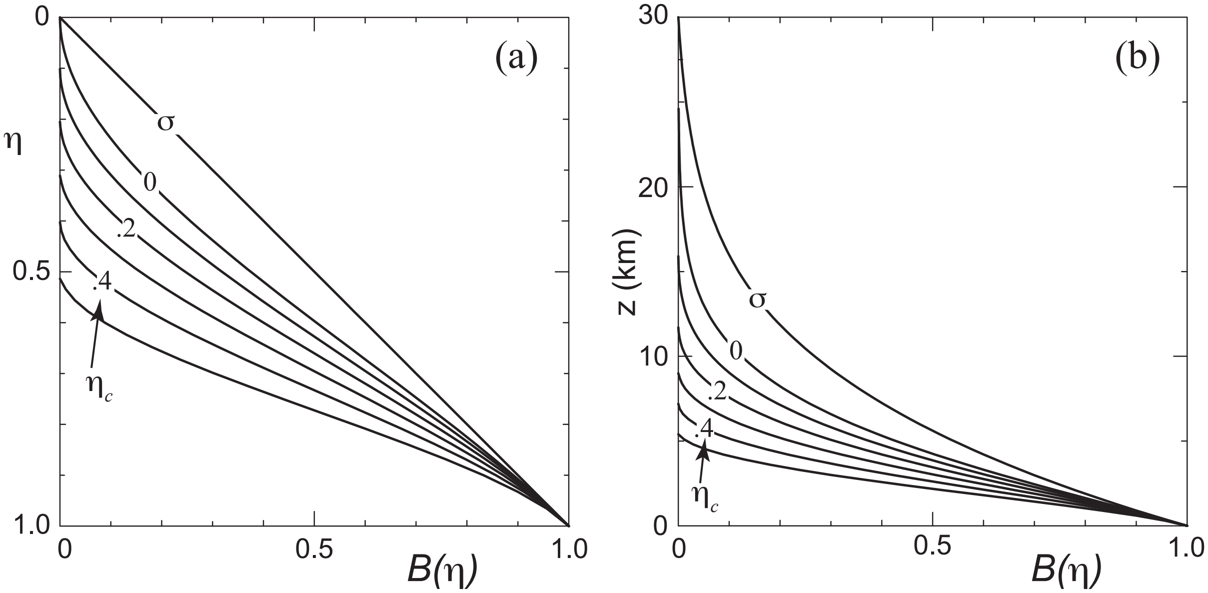

Figure 2.2: B(η) profiles for sigma (σ) coordinate and for hybrid coordinate for η_c = $0., 0.1,$ 0.2, 0.3, 0.4, and 0.5 displayed (a) as a function of η, and (b) as a function of height for a standard atmosphere in a domain with a 30 km upper boundary.

2.2 Flux-Form Euler Equations

Using the variables defined above, the flux-form Euler equations can be written as

$$\partial_t U + (\nabla \cdot \mathbf{V}u) + \mu_d \alpha \partial_x p + (\alpha/\alpha_d)\partial_\eta p \partial_x \phi = F_U \tag{2.8}$$

$$\partial_t V + (\nabla \cdot \mathbf{V}v) + \mu_d \alpha \partial_y p + (\alpha/\alpha_d)\partial_\eta p \partial_y \phi = F_V \tag{2.9}$$

$$\partial_t W + (\nabla \cdot \mathbf{V}w) - g[(\alpha/\alpha_d)\partial_\eta p - \mu_d] = F_W \tag{2.10}$$

$$\partial_t \Theta_m + (\nabla \cdot \mathbf{V}\theta_m) = F_{\Theta_m} \tag{2.11}$$

$$\partial_t \mu_d + (\nabla \cdot \mathbf{V}) = 0 \tag{2.12}$$

$$\partial_t \phi + \mu_d^{-1}[(\mathbf{V} \cdot \nabla \phi) - gW] = 0 \tag{2.13}$$

$$\partial_t Q_m + (\nabla \cdot \mathbf{V}q_m) = F_{Q_m} \tag{2.14}$$

with the diagnostic equation for dry hydrostatic pressure

$$\partial_\eta \phi = -\alpha_d \mu_d \tag{2.15}$$

and the diagnostic relation for the full pressure (dry air plus water vapor)

$$p = p_0 \left(\frac{R_d \theta_m}{p_0 \alpha_d} \right)^\gamma . \tag{2.16}$$

In these equations, α_d is the inverse density of the dry air ($1/\rho_d$) and α is the inverse density taking into account the full parcel density $\alpha = \alpha_d(1 + q_v + q_c + q_r + q_i + ...)^{-1}$.

In (2.8) – (2.14), the subscripts x, y and η denote differentiation,

$$\nabla \cdot \mathbf{V}a = \partial_x(Ua) + \partial_y(Va) + \partial_\eta(\Omega a),$$

and

$$\mathbf{V} \cdot \nabla a = U\partial_x a + V\partial_y a + \Omega\partial_\eta a,$$

where a represents a generic variable. $\gamma = c_p/c_v = 1.4$ is the ratio of the heat capacities for dry air, R_d is the gas constant for dry air, and p_0 is a reference surface pressure (typically 10^5 Pascals). The right-hand-side (RHS) terms F_U, F_V, F_W, and F_{Θ_m} represent forcing terms arising from model physics, turbulent mixing, spherical projections, and the earth's rotation.

In specifying the prognostic set of equations, a prognostic pressure equation could be used in place of (2.13) (see Laprise, 1992). However, pressure is not a conserved variable and with pressure as a prognostic variable we could not use the conservation equation (2.11) for Θ_m because they are linearly dependent. Additionally, prognostic pressure equations have the disadvantage of possessing a mass divergence term multiplied by a large coefficient (proportional to the sound speed) which makes spatial and temporal discretization problematic. It should be noted that the relation for the dry hydrostatic pressure (2.15) does not impose a hydrostatic constraint on the solution, rather it is a diagnostic relation that formally is part of the coordinate definition. In the hydrostatic counterpart to the nonhydrostatic equations, the full hydrostatic equation $\partial_\eta p = \mu_d \alpha_d/\alpha$ replaces the vertical momentum equation (2.10) and enforces a hydrostatic constraint on the solution.

In previous versions of the ARW the prognostic thermodynamic equation was expressed in terms of Θ instead of Θ_m in (2.11). That representation is consistent with the expectation that variations in q_v have little impact during the small acoustic time steps in the split-explicit numerics described in the next chapter, which has proven to be a robust approximation over a wide spectrum of applications. However, in a recent study, Xiao et al. (2015) found that in high-resolution LES with sharp vertical variations in water vapor, WRF simulations exhibited a strong sensitivity to the time step used to accommodate the acoustic modes. Recasting the prognostic thermodynamic equation in terms of Θ_m allowed consistent treatment of moisture in the calculation of pressure during the acoustic time steps, and spurious motions and time-step sensitivity were eliminated. Use of Θ_m as the prognostic thermodynamic variable is also consistent with formulation used in the Model for Prediction Across Scales (MPAS), which utilizes similar split-explicit numerics (Skamarock et al., 2012).

2.3 Map Projections, Coriolis and Curvature Terms

The ARW solver currently supports four projections to the sphere— the Lambert conformal, polar stereographic, Mercator, and latitude-longitude projections. These projections are described in Haltiner and Williams (1980). The transformation is isotropic for three of these projections – the Lambert conformal, polar stereographic, and Mercator grids. An isotropic transformation requires $(\Delta x/\Delta y)|_{earth} =$ constant everywhere on the grid. Only isotropic transformations were supported in the previous ARW releases. Starting with the ARWV3 release, we now support anisotropic projections, in this case the latitude-longitude grid, and with it the full latitude-longitude global model. The ARW implements the projections using map factors, and the generalization to anisotropic transformations introduced in ARW V3 requires that there be map factors for both the x and y components of the transformation from computational to physical space in order to accommodate the anisotropy.

In the ARW's computational space, Δx and Δy are constants. Orthogonal projections to the sphere require that the physical distances between grid points in the projection vary with position on the grid. To transform the governing equations, map scale factors m_x and m_y are defined as the ratio of the distance in computational space to the corresponding distance on the earth's surface:

$$(m_x, m_y) = \frac{(\Delta x, \Delta y)}{\text{distance on the earth}}. \tag{2.17}$$

The ARW solver includes the map-scale factors in the governing equations by redefining the momentum variables as

$$U = \mu_d u/m_y, \quad V = \mu_d v/m_x, \quad W = \mu_d w/m_y, \quad \Omega = \mu_d \omega/m_y.$$

Using these redefined momentum variables, the governing prognostic equations (2.8)-(2.14) including map factors can be written as

$$\begin{aligned}
&\partial_t U + m_x[\partial_x(Uu) + \partial_y(Vu)] \\
&\qquad + \quad \partial_\eta(\Omega u) + (m_x/m_y)[\mu_d \alpha \partial_x p + (\alpha/\alpha_d)\partial_\eta p \partial_x \phi] = F_U && (2.18)\\
&\partial_t V + m_y[\partial_x(Uv) + \partial_y(Vv)] \\
&\qquad +(m_y/m_x)\partial_\eta(\Omega v) + (m_y/m_x)[\mu_d \alpha \partial_y p + (\alpha/\alpha_d)\partial_\eta p \partial_y \phi] = F_V && (2.19)\\
&\partial_t W + m_x[\partial_x(Uw) + \partial_y(Vw)] + \partial_\eta(\Omega w) - m_y^{-1} g[(\alpha/\alpha_d)\partial_\eta p - \mu_d] = F_W && (2.20)\\
&\partial_t \Theta_m + m_x m_y[\partial_x(U\theta_m) + \partial_y(V\theta_m)] + m_y \partial_\eta(\Omega\theta_m) = F_{\Theta_m} && (2.21)\\
&\partial_t \mu_d + m_x m_y[U_x + V_y] + m_y \partial_\eta(\Omega) = 0 && (2.22)\\
&\partial_t \phi + \mu_d^{-1}[m_x m_y(U\partial_x\phi + V\partial_y\phi) + m_y \Omega \partial_\eta \phi - m_y g W] = 0 && (2.23)\\
&\partial_t Q_m + m_x m_y \partial_x(U q_m) + \partial_y(V q_m)] + m_y \partial_\eta(\Omega q_m) = F_{Q_m}, && (2.24)
\end{aligned}$$

which are solved together with the diagnostic equations (2.15) and (2.16).

The right-hand-side terms of the momentum equations (2.18) – (2.20) contain the Coriolis and curvature terms along with mixing terms and physical forcings. Including the map-scale factors (2.17), the Coriolis and curvature terms are cast in the following form:

$$F_{U_{cor}} = +\frac{m_x}{m_y} \left(f + u\frac{m_y}{m_x}\frac{\partial m_x}{\partial y} - v\frac{\partial m_y}{\partial x}\right)V - \left(\frac{u}{r_e} + e\cos\alpha_r\right)W \tag{2.25}$$

$$F_{V_{cor}} = -\frac{m_y}{m_x}\left[\left(f + u\frac{m_y}{m_x}\frac{\partial m_x}{\partial y} - v\frac{\partial m_y}{\partial x}\right)U + \left(\frac{v}{r_e} - e\sin\alpha_r\right)W\right] \tag{2.26}$$

$$F_{W_{cor}} = +e\left(U\cos\alpha_r - \frac{m_x}{m_y}V\sin\alpha_r\right) + \frac{1}{r_e}\left(uU + \frac{m_x}{m_y}vV\right), \tag{2.27}$$

where α_r is the local rotation angle between the y-axis and the meridians, ψ is the latitude, $f = 2\Omega_e \sin\psi$, $e = 2\Omega_e \cos\psi$, Ω_e is the angular rotation rate of the earth, and r_e is the radius of the earth. In this formulation we have approximated the radial distance from the center of the earth as the mean earth radius r_e, and we have not taken into account the change in horizontal grid distance as a function of the radius. The terms containing the map-scale factors represent the horizontal curvature terms, those containing r_e relate to vertical (earth-surface) curvature, and those with e and f are the Coriolis force.

For the isotropic projections (Lambert conformal, polar stereographic, and Mercator), the map-scale factors are the same in both horizontal directions, such that $m_x = m_y = m$, where m typically only varies with latitude. For the anisotropic latitude-longitude grid, $m_x = \sec\psi$ and $m_y = 1$, so that $\partial m_x/\partial y = (1/r_e)\sec\psi\tan\psi$ and $\partial m_y/\partial x = 0$, given that $\partial/\partial y = (1/r_e)\partial/\partial\psi$. For idealized cases on a Cartesian grid, the map-scale factors $m_x = m_y = 1$, f is specified, and e and r_e^{-1} should be zero to remove the curvature terms.

2.4 Perturbation Form of the Governing Equations

Before constructing the discrete solver, it is advantageous to recast the governing equations using perturbation variables to reduce truncation errors in the horizontal pressure gradient calculations in the discrete solver and machine rounding errors in the vertical pressure gradient and buoyancy calculations. For this purpose, new variables are defined as perturbations from a hydrostatically-balanced reference state, and we define reference state variables (denoted by overbars) that are a function of height only and that satisfy the governing equations for an atmosphere at rest. That is, the reference state is in hydrostatic balance and is strictly only a function of $\bar{z}$. In this manner, $p = \bar{p}(\bar{z}) + p'$, $\phi = \bar{\phi}(\bar{z}) + \phi'$, $\alpha = \bar{\alpha}_d(\bar{z}) + \alpha'_d$, and $\mu_d = \bar{\mu}_d(x, y) + \mu'_d$. Because the η coordinate surfaces are generally not horizontal, the reference profiles $\bar{p}$, $\bar{\phi}$, and $\bar{\alpha}$ are functions of (x, y, η). The hydrostatically balanced portion of the pressure gradients in the reference sounding can be removed without approximation to the equations using these perturbation variables. The momentum equations (2.18) – (2.20) are written as

$$
\begin{aligned}
&\partial_t U + m_x\left[\partial_x(Uu) + \partial_y(Vu)\right] + \partial_\eta(\Omega u) \\
&\qquad + (m_x/m_y)(\alpha/\alpha_d)\left[\mu_d(\partial_x\phi' + \alpha_d\partial_x p' + \alpha'_d\partial_x\bar{p}) + \partial_x\phi(\partial_\eta p' - \mu'_d)\right] = F_U \qquad (2.28)\\
&\partial_t V + m_y[\partial_x(Uv) + \partial_y(Vv)] + (m_y/m_x)\partial_\eta(\Omega v) \\
&\qquad + (m_y/m_x)(\alpha/\alpha_d)\left[\mu_d(\partial_y\phi' + \alpha_d\partial_y p' + \alpha'_d\partial_y\bar{p}) + \partial_y\phi(\partial_\eta p' - \mu'_d)\right] = F_V \qquad (2.29)\\
&\partial_t W + m_x[\partial_x(Uw) + \partial_y(Vw)] + \partial_\eta(\Omega w) \\
&\qquad - m_y^{-1}g(\alpha/\alpha_d)[\partial_\eta p' - \bar{\mu}_d(q_v + q_c + q_r)] + m_y^{-1}\mu'_d g = F_W, \qquad (2.30)
\end{aligned}
$$

and the mass conservation equation (2.22) and geopotential equation (2.23) become

$$
\partial_t\mu'_d + m_x m_y[\partial_x U + \partial_y V] + m_y\partial_\eta\Omega = 0 \qquad (2.31)
$$

$$
\partial_t\phi' + \mu_d^{-1}[m_x m_y(U\partial_x\phi + V\partial_y\phi) + m_y\Omega\partial_\eta\phi - m_y g W] = 0, \qquad (2.32)
$$

and the diagnostic equation for dry hydrostatic pressure (2.15) becomes

$$
\partial_\eta\phi' = -\bar{\mu}_d\alpha'_d - \alpha_d\mu'_d. \qquad (2.33)
$$

Additionally, an option is available to use the hypsometric equation for the dry hydrostatic pressure in place of (2.33):

$$
\partial\phi/\partial(\ln p_d) = -p_d(\bar{\alpha}_d + \alpha'_d). \qquad (2.34)
$$

This form of the hydrostatic relation can produce a more accurate discretization compared with (2.33) when the variation with η of temperature ($p_d\alpha_d$) is more linear than that of density

(α_d^{-1}). The conservation equations for the potential temperature (2.21) and the scalar moisture equations (2.24) remain unchanged.

Equations (2.28) – (2.33), together with the equation of state (2.16), represent the equations solved in the ARW. The RHS terms in these equations include the Coriolis terms (2.25) – (2.27), mixing terms (described in Chapter 4), and parameterized physics (described in Chapter 8). Also note that the equation of state (2.16) cannot be written in perturbation form because of the exponent in the expression. For small perturbation simulations, accuracy for perturbation variables can be maintained by linearizing (2.16) for the perturbation variables.

Chapter 3

Model Discretization

3.1 Temporal Discretization

The ARW solver uses a time-split integration scheme. Generally speaking, slow or low-frequency (meteorologically significant) modes are integrated using a third-order Runge-Kutta (RK3) time integration scheme, while the high-frequency acoustic modes are integrated over smaller time steps to maintain numerical stability. The horizontally propagating acoustic modes (including the external mode present in the mass-coordinate equations using a constant-pressure upper boundary condition) and gravity waves are integrated using a forward-backward time integration scheme, and vertically propagating acoustic modes and buoyancy oscillations are integrated using a vertically implicit scheme (using the acoustic time step). The time-split integration for the flux-form equations is described and analyzed in Klemp et al. (2007). The time-splitting is similar to that first developed by Klemp and Wilhelmson (1978) for leapfrog time integration and analyzed by Skamarock and Klemp (1992). This time-split approach was extended to the RK3 scheme as described in Wicker and Skamarock (2002). The primary differences between the earlier implementations described in the references and the ARW implementation are associated with our use of the mass vertical coordinate and a flux-form set of equations, as described in Klemp et al. (2007), along with our use of perturbation variables for the acoustic component of the time-split integration. The acoustic-mode integration is cast in the form of a correction to the RK3 integration.

3.1.1 Runge-Kutta Time Integration Scheme

The RK3 scheme, described in Wicker and Skamarock (2002), integrates a set of ordinary differential equations using a predictor-corrector formulation. Defining the prognostic variables in the ARW solver as $\Phi = (U, V, W, \Theta_m, \phi', \mu'_d, Q_m)$ and the model equations as $\Phi_t = R(\Phi)$, the RK3 integration takes the form of 3 steps to advance a solution $\Phi(t)$ to $\Phi(t + \Delta t)$:

$$\Phi^* = \Phi^t + \frac{\Delta t}{3} R(\Phi^t) \tag{3.1}$$

$$\Phi^{**} = \Phi^t + \frac{\Delta t}{2} R(\Phi^*) \tag{3.2}$$

$$\Phi^{t+\Delta t} = \Phi^t + \Delta t R(\Phi^{**}) \tag{3.3}$$

where Δt is the time step for the low-frequency modes (the model time step). In (3.1) – (3.3), superscripts denote time levels. This scheme is not a true Runge-Kutta scheme *per se* because, while it is third-order accurate for linear equations, it is only second-order accurate for nonlinear equations. With respect to the ARW equations, the time derivatives Φ_t are the partial time derivatives (the leftmost terms) in equations (2.21), (2.24), and (2.28) – (2.32), and $R(\Phi)$ are the remaining terms in those equations.

3.1.2 Acoustic Integration

The high-frequency but meteorologically insignificant acoustic modes would severely limit the RK3 time step Δt in (3.1) – (3.3). To circumvent this time step limitation we use the time-split approach described in Wicker and Skamarock (2002). Additionally, to increase the accuracy of the splitting, we integrate a perturbation form of the governing equations using smaller acoustic time steps within the RK3 large-time-step sequence. To form the perturbation equations for the RK3 time-split acoustic integration, we define small time step variables that are deviations from the most recent RK3 predictor (denoted by the superscript t^* and representing either Φ^t, Φ^*, or Φ^{**} in (3.1) – (3.3)):

$$\begin{aligned} \mathbf{V}'' &= \mathbf{V} - \mathbf{V}^{t^*}, & \Omega'' &= \Omega - \Omega^{t^*}, & \Theta_m'' &= \Theta_m - \Theta_m^{t^*}, \\ \phi'' &= \phi' - {\phi'}^{t^*}, & \alpha_d'' &= \alpha_d' - {\alpha'}_d^{t^*}, & \mu_d'' &= \mu_d' - {\mu'}_d^{t^*}. \end{aligned}$$

The hydrostatic relation (i.e., the vertical coordinate definition) becomes

$$\alpha_d'' = -\frac{1}{\mu_d^{t^*}}\left(\partial_\eta \phi'' + \alpha_d^{t^*}\mu_d''\right). \tag{3.4}$$

Additionally, we also introduce a version of the equation of state that is linearized about t^*,

$$p'' = \frac{c_s^2}{\alpha_d^{t^*}}\left(\frac{\Theta_m''}{\Theta_m^{t^*}} - \frac{\alpha_d''}{\alpha_d^{t^*}} - \frac{\mu_d''}{\mu_d^{t^*}}\right), \tag{3.5}$$

where $c_s^2 = \gamma p^{t^*}\alpha_d^{t^*}$ is the square of the sound speed. The linearized state equation (3.5) and the vertical coordinate definition (3.4) are used to cast the vertical pressure gradient in (2.30) in terms of the model's prognostic variables. By combining (3.5) and (3.4), the vertical pressure gradient can be expressed as

$$\partial_\eta p'' = \partial_\eta(C\partial_\eta \phi'') + \partial_\eta\left(\frac{c_s^2}{\alpha_d^{t^*}}\frac{\Theta_m''}{\Theta_m^{t^*}}\right), \tag{3.6}$$

where $C = c_s^2/\mu_d^{t^*}{\alpha_d^{t^*}}^2$. This linearization about the most recent large time step should be highly accurate over the time interval of the several small time steps.

These variables along with (3.6) are substituted into equations (2.21) and (2.28) – (2.33) and lead to the acoustic time-step equations:

$$\partial_t U'' + (m_x/m_y)(\alpha^{t^*}/\alpha_d^{t^*})\left[\mu_d^{t^*}\left(\alpha_d^{t^*}\partial_x p''^{\tau} + \alpha_d''^{\tau}\partial_x \bar{p} + \partial_x \phi''^{\tau}\right) + \partial_x \phi^{t^*}\left(\partial_\eta p'' - \mu_d''\right)^{\tau}\right] = R_U^{t^*} \tag{3.7}$$

$$\partial_t V'' + (m_y/m_x)(\alpha^{t^*}/\alpha_d^{t^*})\left[\mu_d^{t^*}\left(\alpha_d^{t^*}\partial_y p''^{\tau} + \alpha_d''^{\tau}\partial_y \bar{p} + \partial_y \phi''^{\tau}\right) + \partial_y \phi^{t^*}\left(\partial_\eta p'' - \mu_d''\right)^{\tau}\right] = R_V^{t^*} \tag{3.8}$$

$$\delta_\tau \mu_d'' + m_x m_y[\partial_x U'' + \partial_y V'']^{\tau+\Delta\tau} + m_y \partial_\eta \Omega''^{\tau+\Delta\tau} = {R_\mu}^{t^*} \tag{3.9}$$

$$\delta_\tau \Theta_m'' + m_x m_y[\partial_x(U''\theta_m^{t^*}) + \partial_y(V''\theta_m^{t^*})]^{\tau+\Delta\tau} + m_y \partial_\eta(\Omega''^{\tau+\Delta\tau}\theta_m^{t^*}) = {R_{\Theta_m}}^{t^*} \tag{3.10}$$

$$\delta_\tau W'' - m_y^{-1} g \overline{\left\{(\alpha/\alpha_d)^{t^*}\left[\partial_\eta(C\partial_\eta \phi'') + \partial_\eta\left(\frac{c_s^2}{\alpha^{t^*}}\frac{\Theta_m''}{\Theta_m^{t^*}}\right)\right] - \mu_d''\right\}}^{\tau} = {R_W}^{t^*} \tag{3.11}$$

$$\delta_\tau \phi'' + \frac{1}{\mu_d^{t^*}}\left[m_y \Omega''^{\tau+\Delta\tau}\delta_\eta \phi^{t^*} - m_y \overline{gW''}^{\tau}\right] = {R_\phi}^{t^*}. \tag{3.12}$$

The RHS terms in (3.7) – (3.12) are fixed for the acoustic steps that comprise the time integration of each RK3 sub-step (i.e., (3.1) – (3.3)), and are given by

$$\begin{aligned}
R_U^{t^*} =& - m_x\left[\partial_x(Uu) + \partial_y(Vu)\right] - \partial_\eta(\Omega u) \\
& - (m_x/m_y)(\alpha/\alpha_d)\left[\mu_d(\partial_x \phi' + \alpha_d \partial_x p' + \alpha_d' \partial_x \bar{p}) + \partial_x \phi(\partial_\eta p' - \mu_d')\right] && (3.13) \\
R_V^{t^*} =& - m_y\left[\partial_x(Uv) + \partial_y(Vv)\right] - (m_y/m_x)\partial_\eta(\Omega v) \\
& - (m_y/m_x)(\alpha/\alpha_d)\left[\mu_d(\partial_y \phi' + \alpha_d \partial_y p' + \alpha_d' \partial_y \bar{p}) + \partial_y \phi(\partial_\eta p' - \mu_d')\right] && (3.14) \\
R_{\mu_d}^{t^*} =& - m_x m_y[\partial_x U + \partial_y V] - m_y \partial_\eta \Omega && (3.15) \\
R_{\Theta_m}^{t^*} =& - m_x m_y[\partial_x(U\theta_m) + \partial_y(V\theta_m)] - m_y \partial_\eta(\Omega\theta_m) + F_{\Theta_m} && (3.16) \\
R_W^{t^*} =& - m_x[\partial_x(Uw) + \partial_y(Vw)] - \partial_\eta(\Omega w) \\
& + m_y^{-1} g(\alpha/\alpha_d)[\partial_\eta p' - \bar{\mu}_d(q_v + q_c + q_r)] - m_y^{-1}\mu_d' g + F_W && (3.17) \\
R_\phi^{t^*} =& - \mu_d^{-1}[m_x m_y(U\partial_x \phi + V\partial_y \phi) + m_y \Omega \partial_\eta \phi - m_y g W], && (3.18)
\end{aligned}$$

where all variables in (3.13) – (3.18) are evaluated at time t^* (i.e., using Φ^t, Φ^*, or Φ^{**} for the appropriate RK3 sub-step in (3.1) – (3.3)). Equations (3.7) – (3.12) utilize the discrete acoustic time-step operator

$$\delta_\tau a = \frac{a^{\tau+\Delta\tau} - a^{\tau}}{\Delta\tau},$$

where $\Delta\tau$ is the acoustic time step, and terms averaged in time over an acoustic time step are slightly forward centered using an averaging operator

$$\overline{a}^{\tau} = \frac{1+\beta}{2}a^{\tau+\Delta\tau} + \frac{1-\beta}{2}a^{\tau}, \tag{3.19}$$

where β is a user-specified parameter (see Section 4.3.3).

The integration over the acoustic time steps proceeds as follows. Beginning with the small time-step variables at time τ, (3.7) and (3.8) are stepped forward to obtain $U''^{\tau+\Delta\tau}$ and $V''^{\tau+\Delta\tau}$. Both $\mu''^{\tau+\Delta\tau}$ and $\Omega''^{\tau+\Delta\tau}$ are then calculated from (3.9). This is accomplished by first integrating (3.9) vertically from the surface to the material surface at the top of the domain, which removes the $\partial_\eta \Omega''$ term. Recalling that $\mu_d = \partial p_d/\partial\eta$ and that p_d for the hybrid vertical coordinate is defined by (2.2), the vertical integral of (3.9) becomes,

$$\delta_\tau {p_c}'' = m_x m_y \int_1^0 [\partial_x U'' + \partial_y V'']^{\tau+\Delta\tau} d\eta, \tag{3.20}$$

where $p_c(x, y) = p_s - p_t$ is the dry hydrostatic pressure difference (mass) in the vertical column at (x, y). After computing $\delta_\tau p_c''$ from (3.20), $\Omega''^{\tau+\Delta\tau}$ is obtained by vertically integrating the $\partial_\eta \Omega''$ term (3.9) (with $\delta_\tau \mu = B_\eta \delta_\tau p_c$) using the lower boundary condition $\Omega'' = 0$ at the surface, which yields

$$\Omega''^{\tau+\Delta\tau} = m_y^{-1} \big[1 - B(\eta)\big] \delta_\tau p_c - m_x \int_1^\eta [\partial_x U'' + \partial_y V'']^{\tau+\Delta\tau} d\eta, \tag{3.21}$$

and $\mu_d''^{\tau+\Delta\tau}$ is recovered using (2.2):

$$\mu_d''^{\tau+\Delta\tau}(x, y, \eta) = B_\eta(\eta) p_c''^{\tau+\Delta\tau}(x, y) + \big[1 - B_\eta(\eta)\big](p_0 - p_t). \tag{3.22}$$

From (3.22), it is evident that μ need not be stored as a three-dimensional array, but can be readily constructed when needed from the two-dimensional $p_c(x, y)$ array together with the one-dimensional $B_\eta(\eta)$ profile.

Knowing $\Omega''^{\tau+\Delta\tau}$, (3.10) can be stepped forward to calculate ${\Theta_m''}^{\tau+\Delta\tau}$. Equations (3.11) and (3.12) are combined to form a vertically implicit equation that is solved for $W''^{\tau+\Delta\tau}$ subject to the boundary condition $\Omega = \Omega'' = 0$ at the surface ($z = h(x, y)$) and $p' = 0$ along the model top. $\phi''^{\tau+\Delta\tau}$ is then obtained from (3.12), and $p''^{\tau+\Delta\tau}$ and $\alpha_d''^{\tau+\Delta\tau}$ are recovered from (3.5) and (3.4).

3.1.3 Full Time-Split Integration Sequence

The time-split RK3 integration technique is summarized in Figure 3.1. It consists of two primary loops— an outer loop for the large-time-step Runge-Kutta integration, and an inner loop for the acoustic mode integration.

In the RK3 scheme, physics can be integrated within the RK3 time integration (using a time forward step, i.e., step (1) in Fig. 3.1, or the RK3 time integration if higher temporal accuracy is desired, i.e., in step (2)— implying a physics evaluation every RK3 substep) or external to it using additive timesplitting, i.e., step (9).

Within the acoustic integration, the acoustic time step $\Delta\tau$ is specified by the user through the choice of n_s (see Section 3.3.2). Within the first RK3 substep, however, a single acoustic time step is used to advance the solution regardless of n_s. Within the full RK3-acoustic timesplit integration, this modified acoustic time step does not impose any additional stability constraints (see Wicker and Skamarock, 2002).

The major costs in the model arise from the evaluation of the right hand side terms R^{t^*} in (3.7) – (3.12). The efficiency of the RK3 timesplit scheme arises from the fact that the RK3 time step Δt is much larger than the acoustic time step $\Delta\tau$, hence the most costly evaluations are only performed in the less-frequent RK3 steps.

3.1.4 Diabatic Forcing

Within the RK3 integration sequence outlined in Fig. 3.1, the RHS term $R^{t^*}_{\Theta_m}$ in the thermodynamic equation (3.10) contains contributions from the diabatic physics tendencies that are computed in step (1) at the beginning of the first RK3 step. This diabatic forcing is integrated within the acoustic steps (specifically, in step 4 in the time integration sequence shown in Fig.

```
Begin Time Step
    Begin RK3 Loop: Steps 1, 2, and 3
        (1) If RK3 step 1, compute and store $F_\Phi$
                (i.e., physics tendencies for RK3 step, including mixing).
        (2) Compute $R^{t^*}$, (3.13)–(3.18)
        Begin Acoustic Step Loop: Steps $1 \rightarrow n$,
            RK3 step 1, $n = 1$,       $\Delta\tau = \Delta t/3$;
            RK3 step 2, $n = n_s/2$,   $\Delta\tau = \Delta t/n_s$;
            RK3 step 3, $n = n_s$,     $\Delta\tau = \Delta t/n_s$.
            (3) Advance horizontal momentum, (3.7) and (3.8)
                Global: Apply polar filter to $U''^{\tau+\Delta\tau}$ and $V''^{\tau+\Delta\tau}$.
            (4) Advance $\mu_d$ (3.9) and compute $\Omega''^{\tau+\Delta\tau}$ then advance $\Theta_m$ (3.10)
                Global: Apply polar filter to $\mu_d^{\tau+\Delta\tau}$ and $\Theta_m''^{\tau+\Delta\tau}$.
            (5) Advance $W$ and $\phi$ (3.11) and (3.12)
                Global: Apply polar filter to $W''^{\tau+\Delta\tau}$ and $\phi''^{\tau+\Delta\tau}$.
            (6) Diagnose $p''$ and $\alpha''$ using (3.5) and (3.4)
        End Acoustic Step Loop
        (7) Scalar transport: Advance scalars (2.24)
            over RK3 substep (3.1), (3.2) or (3.3)
            (using mass fluxes $U$, $V$ and $\Omega$ time-averaged over the acoustic steps).
            Global: Apply polar filter to scalars.
        (8) Using updated prognostic variables, compute $p'$ with (2.16) and $\alpha'$ with
            (2.33) or (2.34)
    End RK3 Loop
    (9) Compute non-RK3 physics (currently microphysics), advance variables.
        Global: Apply polar filter to updated variables.
End Time Step
```

Figure 3.1: Time step integration sequence. Here n represents the number of acoustic time steps for a given substep of the RK3 integration, and n_s is the ratio of the RK3 time step to the acoustic time step for the second and third RK3 substeps.

3.1). Additional diabatic contributions are integrated in an additive-time-split manner in step (9) after the RK3 update is complete. Thus, the diabatic forcing computed in step (9) (the microphysics in the current release of the ARW) does not appear in $R^{t^*}_{\Theta_m}$ from (3.10) in the acoustic integration. We have discovered that this time splitting can excite acoustic waves and can give rise to noise in the solutions for some applications. Note that the non-RK3 physics are integrated in step (9) because balances produced in the physics are required at the end of the time step (e.g., the saturation adjustment in the microphysics). So while moving these non-RK3 physics into step (1) would eliminate the noise, the balances produced by these physics would be altered.

We have found that the excitation of the acoustic modes can be circumvented while leaving the non-RK3 physics in step (9) by using the following procedure that is implemented in the ARW. In step (1) of the integration procedure (Fig. 3.1), an estimate of the diabatic forcing in the Θ_m equation arising from the non-RK3 physics in step (9) is included in the diabatic forcing term $R^{t^*}_{\Theta_m}$ in (3.10) (which is advanced in step 4). This estimated diabatic forcing is then removed from the updated Θ_m after the RK3 integration is complete and before the evaluation of the non-RK3 physics in step (9). We use the diabatic forcing from the previous time step as the estimated forcing; hence this procedure results in few additional computations outside of saving the diabatic forcing between time steps.

3.1.5 Hydrostatic Option

A hydrostatic option is available in the ARW solver. The time-split RK3 integration technique summarized in Fig. 3.1 is retained, including the acoustic step loop. Steps (5) and (6) in the acoustic-step loop, where W and ϕ are advanced and p'' and α'' are diagnosed, are replaced by the following three steps. (1) Diagnose the pressure from the full hydrostatic equation (including moisture)

$$\delta_\eta p_h = \frac{\alpha_d}{\alpha}\mu_d = \left(1 + \sum q_m\right)\mu_d.$$

(2) Diagnose α_d using the equation of state (2.16) and the prognosed θ_m. (3) Diagnose the geopotential using the dry hydrostatic equation (2.33). The vertical velocity w can be diagnosed from the geopotential equation, but it is not needed in the solution procedure. The acoustic step loop advances gravity waves, including the external mode, and the Lamb wave when the hydrostatic option is used.

3.2 Spatial Discretization

The spatial discretization in the ARW solver uses a C grid staggering for the variables as shown in Fig. 3.2. That is, normal velocities are staggered one-half grid length from the thermodynamic variables. The variable indices, (i, j, k) indicate variable locations with $(x, y, \eta) = (i\Delta x, j\Delta y, k\Delta\eta)$. We will denote the points where θ is located as being *mass* points, and likewise we will denote locations where u, v, and w are defined as u points, v points, and w points, respectively. Not shown in Fig. 3.2 are the moisture variables q_i, and the coordinate metric μ, defined at the mass points on the discrete grid, and the geopotential ϕ that is defined at the w points. The diagnostic variables used in the model, the pressure p and inverse density α, are

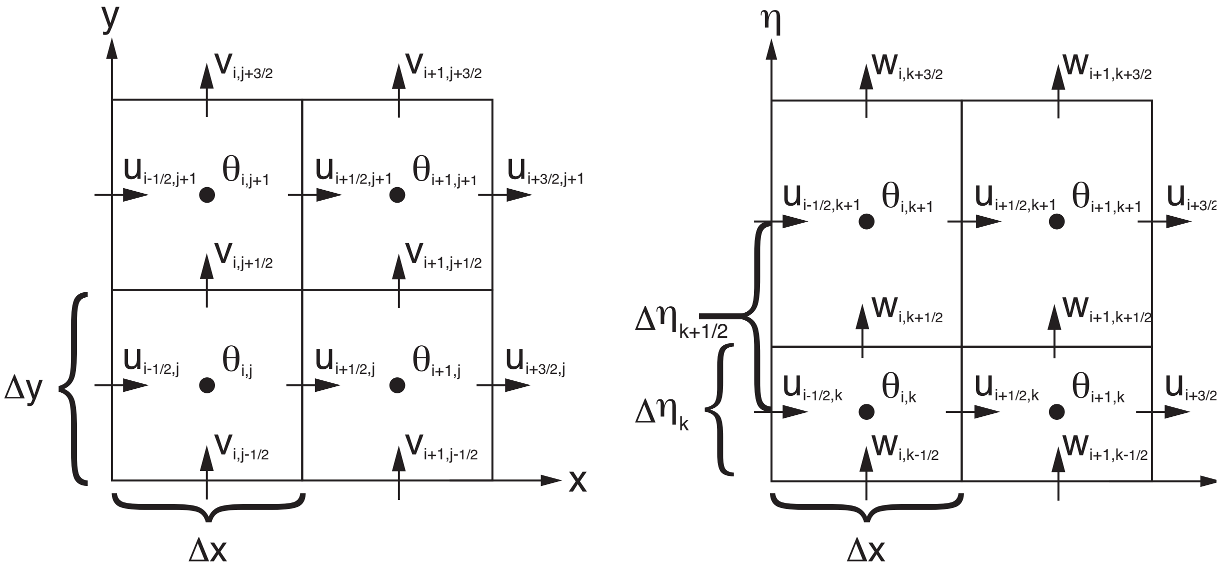

horizontal grid

vertical grid

Figure 3.2: Horizontal and vertical grids of the ARW

computed at mass points. The grid lengths Δx and Δy are constants in the model formulation; changes in the physical grid lengths associated with the various projections to the sphere are accounted for using the map factors introduced in Section 2.3. The vertical grid length $\Delta\eta$ is not a fixed constant; it is specified in the initialization. The user is free to specify the η values of the model levels subject to the constraint that $\eta = 1$ at the surface, $\eta = 0$ at the model top, and η decreases monotonically between the surface and model top. Using these grid and variable definitions, we can define the spatial discretization for the ARW solver.

3.2.1 Acoustic Step Equations

We begin by defining the column-mass-coupled variables relative to the uncoupled variables. The vertical velocity is staggered only in k, so it can be coupled directly to the column mass with no averaging or interpolation. The horizontal velocities are horizontally staggered relative to the column mass such that the continuous variables are represented discretely as

$$U = \frac{\mu_d u}{m_y} \rightarrow \frac{\overline{\mu_d}^x u}{\overline{m_y}^x}, \quad V = \frac{\mu_d v}{m_x} \rightarrow \frac{\overline{\mu_d}^y v}{\overline{m_x}^y},$$

where the discrete operator $\overline{a}^x$ denotes a linear interpolation operator. The grid lengths Δx and Δy are constant, hence in this case the operator reduces to $\overline{a}^x = (a_{i+1/2} + a_{i-1/2})/2$.

Using these definitions, we can write the spatially discrete acoustic step equations

(3.7) – (3.12) as

$$\begin{aligned}
\partial_t U'' + (m_x/m_y)\overline{(\alpha^{t^*}/\alpha_d^{t^*})}^{x}\Bigg[\overline{\mu_d^{t^*}}^{x}\Bigg(\overline{\alpha_d^{t^*}}^{x}\partial_x p''^{\tau} + \overline{\alpha_d''^{\tau}}^{x}\partial_x\overline{p} + \partial_x\overline{\phi''^{\tau}}^{\eta}\Bigg)& \\
+\partial_x\overline{\phi^{t^*}}^{\eta}\Bigg(\partial_\eta\overline{\overline{p''}^{x}}^{\eta} - \overline{\mu_d''}^{x}\Bigg)^{\tau}\Bigg] &= R_U^{t^*} && (3.23)\\
\partial_t V'' + (m_y/m_x)\overline{(\alpha^{t^*}/\alpha_d^{t^*})}^{y}\Bigg[\overline{\mu_d^{t^*}}^{y}\Bigg(\overline{\alpha_d^{t^*}}^{y}\partial_y p''^{\tau} + \overline{\alpha_d''^{\tau}}^{y}\partial_y\overline{p} + \partial_y\overline{\phi''^{\tau}}^{\eta}\Bigg)& \\
+\partial_y\overline{\phi^{t^*}}^{\eta}\Bigg(\partial_\eta\overline{\overline{p''}^{y}}^{\eta} - \overline{\mu_d''}^{y}\Bigg)^{\tau}\Bigg] &= R_V^{t^*} && (3.24)\\
\delta_\tau\mu_d'' + m_x m_y[\delta_x U'' + \delta_y V'']^{\tau+\Delta\tau} + m_y\delta_\eta\Omega''^{\tau+\Delta\tau} &= R_\mu^{t^*} && (3.25)\\
\delta_\tau\Theta_m'' + m_x m_y[\delta_x(U''\overline{\theta_m^{t^*}}^{x}) + \delta_y(V''\overline{\theta_m^{t^*}}^{y})]^{\tau+\Delta\tau} + m_y\delta_\eta(\Omega''^{\tau+\Delta\tau}\overline{\theta_m^{t^*}}^{\eta}) &= {R_{\Theta_m}}^{t^*} && (3.26)\\
\delta_\tau W'' - m_y^{-1}g\overline{\Bigg\{\overline{(\alpha/\alpha_d)^{t^*}}^{\eta}\Bigg[\delta_\eta(C\delta_\eta\phi'') + \delta_\eta\Bigg(\frac{c_s^2}{\alpha^{t^*}}\frac{\Theta_m''}{\Theta_m^{t^*}}\Bigg)\Bigg] - \mu_d''\Bigg\}}^{\tau} &= {R_W}^{t^*} && (3.27)\\
\delta_\tau\phi'' + \frac{1}{\mu_d^{t^*}}[m_y\Omega''^{\tau+\Delta\tau}\delta_\eta\overline{\phi^{t^*}}^{\eta} - m_y g\overline{W''}^{\tau}] &= {R_\phi}^{t^*}, && (3.28)
\end{aligned}$$

where the discrete operator

$$\delta_x a = \Delta x^{-1}(a_{i+1/2} - a_{i-1/2}) \tag{3.29}$$

with the operators δ_y and δ_η similarily defined. Additionally, the operator $\overline{a}^{\eta}$ is a vertical interpolation operator. Using the notation given for the vertically stretched grid depicted in Fig. 3.2, it is defined as

$$\overline{a}^{\eta}|_{k+1/2} = \frac{1}{2}\Bigg(\frac{\Delta\eta_k}{\Delta\eta_{k+1/2}}a_{k+1} + \frac{\Delta\eta_{k+1}}{\Delta\eta_{k+1/2}}a_k\Bigg). \tag{3.30}$$

This operator vertically interpolates variables on mass levels k to the w levels $(k+\frac{1}{2})$. It should be noted that the vertical grid is defined such that vertical interpolation from w levels to mass levels reduces to $\overline{a}_k^{\eta} = (a_{k+1/2} + a_{k-1/2})/2$ (see Fig. 3.2).

The RHS terms in the discrete acoustic step equations for momentum (3.23), (3.24) and (3.27) are discretized as

$$\begin{aligned}
R_U^{t^*} &= -(m_x/m_y)\overline{(\alpha/\alpha_d)}^{x}\Big[\overline{\mu_d}^{x}(\partial_x\overline{\phi'}^{\eta} + \overline{\alpha_d}^{x}\partial_x p' + \overline{\alpha_d'}^{x}\partial_x\overline{p}) + \partial_x\overline{\phi}^{\eta}(\partial_\eta\overline{\overline{p'}^{x}}^{\eta} - \overline{\mu_d'}^{x})\Big] \\
&\qquad + F_{U_{cor}} + \text{advection} + \text{mixing} + \text{physics}, && (3.31)\\
R_V^{t^*} &= -(m_y/m_x)\overline{(\alpha/\alpha_d)}^{y}\Big[\overline{\mu_d}^{y}(\partial_y\overline{\phi'}^{\eta} + \overline{\alpha_d}^{y}\partial_y p' + \overline{\alpha_d'}^{y}\partial_y\overline{p}) + \partial_y\overline{\phi}^{\eta}(\partial_\eta\overline{\overline{p'}^{y}}^{\eta} - \overline{\mu_d'}^{y})\Big] \\
&\qquad + F_{V_{cor}} + \text{advection} + \text{mixing} + \text{physics}, && (3.32)\\
R_W^{t^*} &= \ m_y^{-1}g\overline{(\alpha/\alpha_d)}^{\eta}[\delta_\eta p' + \bar{\mu}_d\overline{q_m}^{\eta}] - m_y^{-1}\mu_d' g \\
&\qquad + F_{W_{cor}} + \text{advection} + \text{mixing} + \text{buoyancy} + \text{physics}. && (3.33)
\end{aligned}$$

3.2.2 Coriolis and Curvature Terms

The terms $F_{U_{cor}}$, $F_{V_{cor}}$, and $F_{W_{cor}}$ in (3.31) – (3.33) represent Coriolis and curvature effects in the momentum equations and are written in continuous form in (2.25) – (2.27). Using the isotropic map projections (Lambert conformal, polar stereographic, and Mercator) where $m_x = m_y = m$, their spatial discretization is

$$F_{U_{cor}} = +\left(\overline{f}^{x} + \overline{\overline{u}^{x}\delta_y m - \overline{v}^{y}\delta_x m}^{x}\right)\overline{V}^{xy} - \overline{e}^{x}\overline{W}^{x\eta}\,\overline{\cos\alpha_r}^{x} - \frac{u\overline{W}^{x\eta}}{r_e}, \tag{3.34}$$

$$F_{V_{cor}} = -\left(\overline{f}^{y} + \overline{\overline{u}^{x}\delta_y m - \overline{v}^{y}\delta_x m}^{y}\right)\overline{U}^{xy} + \overline{e}^{y}\overline{W}^{y\eta}\,\overline{\sin\alpha_r}^{y} - \frac{v\overline{W}^{y\eta}}{r_e}, \tag{3.35}$$

$$F_{W_{cor}} = +e(\overline{U}^{x\eta}\cos\alpha_r - \overline{V}^{y\eta}\sin\alpha_r) + \left(\frac{\overline{u}^{x\eta}\overline{U}^{x\eta} + \overline{v}^{y\eta}\overline{V}^{y\eta}}{r_e}\right). \tag{3.36}$$

Here the operators $\overline{()}^{xy} = \overline{\overline{()}^{x}}^{y}$, and likewise for $\overline{()}^{x\eta}$ and $\overline{()}^{y\eta}$.

For the non-isotropic latitude longitude projection, the Coriolis and curvature terms are discretized as

$$F_{U_{cor}} = \frac{m_x}{m_y}\left[\ \overline{f}^{x}\overline{V}^{xy} + \frac{u\overline{V}^{xy}}{r_e}\tan\psi\right] - \overline{e}^{x}\overline{W}^{x\eta}\,\overline{\cos\alpha_r}^{x} - \frac{u\overline{W}^{x\eta}}{r_e}, \tag{3.37}$$

$$F_{V_{cor}} = \frac{m_y}{m_x}\left[-\overline{f}^{y}\overline{U}^{xy} - \frac{\overline{u}^{xy}\overline{U}^{xy}}{r_e}\tan\psi + \overline{e}^{y}\overline{W}^{y\eta}\overline{\sin\alpha_r}^{y} - \frac{v\overline{W}^{y\eta}}{r_e}\right], \tag{3.38}$$

$$F_{W_{cor}} = +e(\overline{U}^{x\eta}\cos\alpha_r - (m_x/m_y)\overline{V}^{y\eta}\sin\alpha_r) + \left(\frac{\overline{u}^{x\eta}\overline{U}^{x\eta} + (m_x/m_y)\overline{v}^{y\eta}\overline{V}^{y\eta}}{r_e}\right). \tag{3.39}$$

3.2.3 Advection

The advection terms in the ARW solver are in the form of a flux divergence and are a subset of the RHS terms in equations (3.13) – (3.18):

$$R^{t^*}_{U_{adv}} = -\, m_x[\partial_x(Uu) + \partial_y(Vu)] + \qquad\qquad \partial_\eta(\Omega u) \tag{3.40}$$

$$R^{t^*}_{V_{adv}} = -\, m_y[\partial_x(Uv) + \partial_y(Vv)] + (m_x/m_y)\partial_\eta(\Omega v) \tag{3.41}$$

$$R^{t^*}_{\mu_{adv}} = -\, m_x m_y[\partial_x U + \partial_y V] + m_y\partial_\eta\Omega \tag{3.42}$$

$$R^{t^*}_{\Theta_{adv}} = -\, m_x m_y[\partial_x(U\theta_m) + \partial_y(V\theta_m)] - m_y\partial_\eta(\Omega\theta_m) \tag{3.43}$$

$$R^{t^*}_{W_{adv}} = -\, m_x[\partial_x(Uw) + \partial_y(Vw)] + \partial_\eta(\Omega w) \tag{3.44}$$

$$R^{t^*}_{\phi_{adv}} = -\, \mu_d^{-1}[m_x m_y(U\partial_x\phi + V\partial_y\phi) + m_y\Omega\partial_\eta\phi]. \tag{3.45}$$

For the mass conservation equation, the flux divergence is discretized using a 2nd-order centered approximation:

$$R^{t^*}_{\mu_{adv}} = -m_x m_y[\delta_x U + \delta_y V]^{t^*} + m_y\delta_\eta\Omega^{t^*}. \tag{3.46}$$

In the current version of the ARW, the advection of vector quantities (momentum) and scalars is performed using the RK3 time integration as outlined in Fig. 3.1. The spatial discretization used in this approach is outlined in the next section. For many applications it is desirable to use positive definite or monotonic advection schemes for scalar transport.

RK3 Advection

2^{nd} through 6^{th} order accurate spatial discretizations of the flux divergence are available in the ARW for momentum, scalars and geopotential using the RK3 time-integration scheme (scalar advection option 1, step 7 in the time-split integration sequence in Fig. 3.1). The discrete operators can be illustrated by considering the flux divergence equation for a scalar q in its discrete form:

$$R^{t^*}_{q_{adv}} = -m_x m_y [\delta_x(U\overline{q}^{x_{adv}}) + \delta_y(V\overline{q}^{y_{adv}})] - m_y \delta_\eta(\Omega \overline{q}^{\eta_{adv}}). \tag{3.47}$$

As in the pressure gradient discretization, the discrete operator is defined as

$$\delta_x(U\overline{q}^{x_{adv}}) = \Delta x^{-1}\big[(U\overline{q}^{x_{adv}})_{i+1/2} - (U\overline{q}^{x_{adv}})_{i-1/2}\big]. \tag{3.48}$$

The different order advection schemes correspond to different definitions for the operator $\overline{q}^{x_{adv}}$. The even order operators (2^{nd}, 4^{th}, and 6^{th}) are

$$\begin{aligned}
2^{nd}\text{ order:}\quad & (\overline{q}^{x_{adv}})_{i-1/2} = \frac{1}{2}(q_i + q_{i-1}) \\
4^{th}\text{ order:}\quad & (\overline{q}^{x_{adv}})_{i-1/2} = \frac{7}{12}(q_i + q_{i-1}) - \frac{1}{12}(q_{i+1} + q_{i-2}) \\
6^{th}\text{ order:}\quad & (\overline{q}^{x_{adv}})_{i-1/2} = \frac{37}{60}(q_i + q_{i-1}) - \frac{2}{15}(q_{i+1} + q_{i-2}) + \frac{1}{60}(q_{i+2} + q_{i-3}),
\end{aligned}$$

and the odd order operators (3^{rd} and 5^{th}) are

$$\begin{aligned}
3^{rd}\text{ order:}\quad & (\overline{q}^{x_{adv}})_{i-1/2} = (\overline{q}^{x_{adv}})^{4th}_{i-1/2} \\
& \qquad + \operatorname{sign}(U)\frac{1}{12}\big[(q_{i+1} - q_{i-2}) - 3(q_i - q_{i-1})\big] \\
5^{th}\text{ order:}\quad & (\overline{q}^{x_{adv}})_{i-1/2} = (\overline{q}^{x_{adv}})^{6th}_{i-1/2} \\
& \qquad - \operatorname{sign}(U)\frac{1}{60}\big[(q_{i+2} - q_{i-3}) - 5(q_{i+1} - q_{i-2}) + 10(q_i - q_{i-1})\big].
\end{aligned}$$

The even-order advection operators are spatially centered and thus contain no implicit diffusion outside of the diffusion inherent in the RK3 time integration. The odd-order schemes are upwind-biased, and the spatial discretization is inherently diffusive. The behavior of the upwind schemes is easily understood by expanding (3.48) using the 5^{th} order operator, assuming a constant mass flux U and multiplying by the timestep Δt:

$$\begin{aligned}
\Delta t \delta_x(U\overline{q}^{x_{adv}}) &= \Delta t \delta(Uq)|^{6th} - \left|\frac{U\Delta t}{\Delta x}\right| \frac{1}{60}\left(-q_{i-3} + 6q_{i-2} - 15q_{i-1} + 20q_i - 15q_{i+1} + 6q_{i+2} - q_{i+3}\right) \\
&= \Delta t \delta(Uq)|^{6th} - \frac{Cr}{60}\Delta x^6 \frac{\partial^6 q}{\partial x^6} + \text{higher order terms}
\end{aligned}$$

Similarly, we can expand (3.48) using the 3^{rd} order operator:

$$\Delta t \delta_x(U\overline{q}^{x_{adv}}) = \Delta t \delta(Uq)|^{4th} + \frac{Cr}{12}\Delta x^4 \frac{\partial^4 q}{\partial x^4} + \text{higher order terms}$$

As is evident in their formulation, the odd-order schemes are comprised of the next higher (even) order centered scheme plus an upwind term that, for a constant transport mass flux, is a diffusion term of that next higher (even) order with a hyper-viscosity proportional to the Courant number (Cr). The diffusion term is the leading order error term in the flux divergence discretization. Further details concerning RK3 advection can be found in Wicker and Skamarock (2002)

Positive-Definite and Shape-Preserving Limiters for RK3 Advection

Mixing ratios of moisture, chemical species or other tracer species should remain positive-definite, that is, negative masses should not be permitted. Additionally, transport should not introduce any new maxima or minima in the mixing ratios; this property is referred to as shape-preservation also monotonicity. The Runge-Kutta transport integration defined by the timestepping algorithm (3.1) – (3.3), combined with the flux divergence operator (3.47), is conservative but it does not guarantee positive definiteness or shape preservation; any negative values will be offset by positive mass such that mass is conserved, and new maxima and minima may be produced. In many physics options, negative mixing ratios will be set to zero, and this will result in an increase in mass of that species. Both positive-definite and shape-preserving flux renormalizations, applied on the final Runge-Kutta transport step (3.1), can be used to remove these unphysical effects from the RK3 scalar transport scheme. The positive-definite renormalization in the ARW solver is described in Skamarock and Weisman (2008) and the shape-preserving (monotonic) extension is described in Wang et al. (2009), both of which follow an approach first described by Zalesak (1979).

The renormalizations occur as part of the final RK3 time integration step for scalar transport, and the preliminary (i.e. before renormalization) evaluation of the final transport step can be expressed as

$$(\mu\phi)^{t+\Delta t} = (\mu\phi)^t - \Delta t\big\{m_x m_y[\delta_x(U\overline{q}^{x_{adv}}) + \delta_y(V\overline{q}^{y_{adv}})] + m_y\delta_\eta(\Omega\overline{q}^{\eta_{adv}})\big\} + \Delta t\mu S^t_\phi \qquad (3.49)$$

where the flux divergence is evaluated using the (**) time level predicted in RK3 step (3.2). The positive-definite flux renormalization replaces (3.2) with the following two steps. First, the scalar mixing ratio is updated using the tendency derived from the model physics and source/sink terms.

$$(\mu\phi)^{***} = (\mu\phi)^t + \Delta t\mu S^t_\phi \qquad (3.50)$$

where we denote this new predictor as $(\mu\phi)^{***}$. Second, the full update is computed using a flux divergence composed of a first-order upwind flux plus a higher order correction:

$$\begin{aligned}(\mu\phi)^{t+\Delta t} = (\mu\phi)^{***} - \Delta t\big\{\ & m_x m_y\big(\delta_x\left[(U\overline{q}^{x_{adv}})^1 + R(U\overline{q}^{x_{adv}})'\right] \\ & +\delta_y\left[(V\overline{q}^{y_{adv}})^1 + R(V\overline{q}^{y_{adv}})'\right]\big) \\ & +m_y\delta_\eta\left[(\Omega\overline{q}^{\eta_{adv}})^1 + R(\Omega\overline{q}^{\eta_{adv}})'\right]\ \big\}.\end{aligned} \qquad (3.51)$$

In (3.51), $()^1$ denotes a first-order upwind flux and $R()'$ denotes a renormalized higher-order correction flux. The higher-order correction flux is the difference between the full RK3 flux and the first-order upwind flux, that is,

$$(U\overline{q}^{x_{adv}}) = (U\overline{q}^{x_{adv}})^1 + (U\overline{q}^{x_{adv}})', \qquad (3.52)$$

with similar definitions for $(V\overline{q}^{y_{adv}})'$ and $(\Omega\overline{q}^{\eta_{adv}})'$. The correction flux can then be renormalized to achieve positive-definite or shape preserving (monotonic) behavior as follows. First, the upwind fluxes are used to perform a partial update of the scalar mass.

$$(\tilde{\mu\phi}) = (\mu\phi)^{***} - \Delta t\big\{m_x m_y[\delta_x(U\overline{q}^{x_{adv}})^1 + \delta_y(V\overline{q}^{y_{adv}})^1] + m_y\delta_\eta(\Omega\overline{q}^{\eta_{adv}})^1\big\}$$

This update is positive definite (and monotonic) by design because it is a property of the the first-order upwind scheme. Next, a prediction of the minimum and maximum possible values of the new-time-level species mass is computed at each point by using only the outward directed fluxes (fluxes that remove mass from the control volume),

$$(\mu\phi)^{t+\Delta t}_{min} = (\tilde{\mu\phi}) - \Delta t\big\{m_x m_y[\delta_x(U_+\overline{q}^{x_{adv}})' + \delta_y(V_+\overline{q}^{y_{adv}})'] + m_y\delta_\eta(\Omega_+\overline{q}^{\eta_{adv}})'\big\} \tag{3.53}$$

$$(\mu\phi)^{t+\Delta t}_{max} = (\tilde{\mu\phi}) - \Delta t\big\{m_x m_y[\delta_x(U_-\overline{q}^{x_{adv}})' + \delta_y(V_-\overline{q}^{y_{adv}})'] + m_y\delta_\eta(\Omega_-\overline{q}^{\eta_{adv}})'\big\} \tag{3.54}$$

where U_+, V_+ and Ω_+ indicated the use of fluxes out of the control volume only, that is, only those that contribute to lowering the scalar mass, and U_-, V_- and Ω_- indicated the use of fluxes into the control volume only, that is, only those that contribute to rasing the scalar mass.

For the positive-definite renormalization, from (3.53) the scalar mass $(\mu\phi)^{t+\Delta t}_{min} < 0$ if and only if

$$(\tilde{\mu\phi}) < \Delta t\big\{m_x m_y[\delta_x(U_+\overline{q}^{x_{adv}})' + \delta_y(V_+\overline{q}^{y_{adv}})'] + m_y\delta_\eta(\Omega_+\overline{q}^{\eta_{adv}})'\big\}.$$

For each volume where negative mass is indicated by (3.53), the fluxes are renormalized such that the outgoing fluxes and mass in the volume are equivalent.

$$R\,(U_+\overline{q}^{x_{adv}})' = (U_+\overline{q}^{x_{adv}})'\,\frac{\tilde{\mu\phi}}{\Delta t\big\{m_x m_y[\delta_x(U_+\overline{q}^{x_{adv}})' + \delta_y(V_+\overline{q}^{y_{adv}})'] + m_y\delta_\eta(\Omega_+\overline{q}^{\eta_{adv}})'\big\}}$$

with a similar renormalization applied to the $(V_+\overline{q}^{y_{adv}})'$ and $(\Omega_+\overline{q}^{\eta_{adv}})'$.

For the shape-preserving (monotonic) renormalization, the minimum (maximum) value for a cell mixing ratio at the new time level is set as the minimum (maximum) mixing ratio at time t from that cell and its nearest neighbors. This lower bound on the mixing ratio, denoted $(\phi)_{min}$, will be violated when

$$(\tilde{\mu\phi}) - (\mu\phi)_{min} < \Delta t\big\{m_x m_y[\delta_x(U_+\overline{q}^{x_{adv}})' + \delta_y(V_+\overline{q}^{y_{adv}})'] + m_y\delta_\eta(\Omega_+\overline{q}^{\eta_{adv}})'\big\}$$

If the lower bound is violated, the fluxes are renormalized with

$$R\,(U_+\overline{q}^{x_{adv}})' = (U_+\overline{q}^{x_{adv}})'\,\frac{\tilde{\mu\phi} - (\mu\phi)_{min}}{\Delta t\big\{m_x m_y[\delta_x(U_+\overline{q}^{x_{adv}})' + \delta_y(V_+\overline{q}^{y_{adv}})'] + m_y\delta_\eta(\Omega_+\overline{q}^{\eta_{adv}})'\big\}}$$

with a similar renormalization applied to the $(V_+\overline{q}^{y_{adv}})'$ and $(\Omega_+\overline{q}^{\eta_{adv}})'$. A similar limiting process is used to renormalize the fluxes such that the maximum mixing ratio is not exceeded. Note that outgoing fluxes for one cell are inflow fluxes for another, and the renormalized flux used in the update is the minimum flux necessary to satisfy the mimimum or maximum bounds for the two cells utilizing the flux.

The renormalized higher-order-correction fluxes along with the first order fluxes are then used in the update equation (3.51). Note that if no renormalization is needed the scheme (3.51) reverts to the standard RK3 update because of the definition of the higher-order correction (3.52).

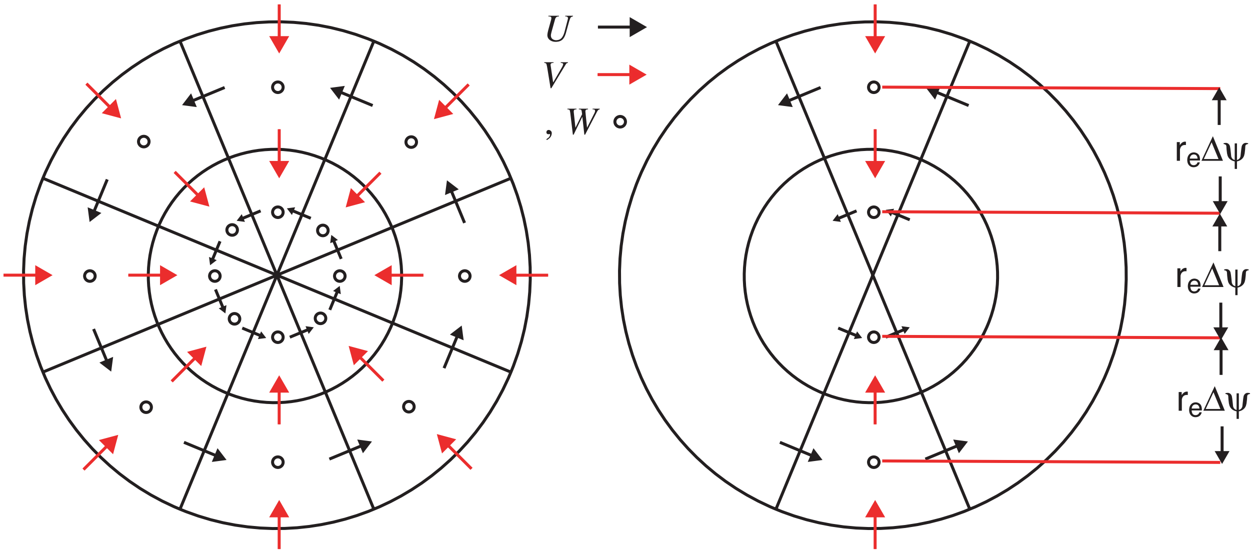

Figure 3.3: Latitude-longitude grid structure in the pole region. In the ARW formulation, $r_e \Delta\psi = \Delta y / m_y$.

3.2.4 Pole Conditions for the Global Latitude-Longitude Grid

The latitude-longitude grid has a singularity at the two poles where the latitude $\psi = \pm 90°$, as illustrated in Figure 3.3. By design, no variable is defined at the pole point. The area of the control volume face at the pole is zero, thus a flux at the pole point is not needed in the solution of any of the prognostic variables. For example, in the finite volume discretization of the mass conservation equation (3.25) for μ in a control volume closest to the pole, the meridional gradient (y gradient) of the mass flux $\delta_y V''$ will use zero for the pole contribution to this term.

The stencils for advection operators higher than 2nd order, described in Section 3.2.3, cross the poles for flux calculations at the control volume faces located $r_e \Delta\psi$ and $2 r_e \Delta\psi$ from the pole point (Figure 3.3, the V flux is indicated in red). In the current implementation of the ARW, we reduce the order of the flux operator at these faces so that their stencils do not extend across the pole point. While this formally reduces the accuracy of the scheme, we have not been able to identify any significant degradation in the ARW solutions.

Coriolis and curvature terms are computed for the vertical momentum equation (3.39) and the horizontal momentum equation for U (3.37). For the W and U points that lie $r_e \Delta\psi / 2$ from the pole, the stencils for these terms require a value of V at the pole point. We set the value of V at the pole equal to the value of V at $\Delta\psi$ to evaluate these operators. This approximation is also used for the meridional advection of V, combined with a lowering of the flux-operator order to avoid differencing across the pole (as with the flux divergence terms for the other prognostic variables).

3.3 Stability Constraints

There are two time steps that a user must specify when running the ARW: the model time step (the time step used by the RK3 scheme, see Section 3.1.1) and the acoustic time step (used in the acoustic sub-steps of the time-split integration procedure, see Section 3.1.2). Both are limited by Courant numbers. In the following sections we describe how to choose time steps for applications.

3.3.1 RK3 Time Step Constraint

The RK3 time step is limited by the advective Courant number $u\Delta t/\Delta x$ and the user's choice of advection schemes— users can choose 2^{nd} through 6^{th} order discretizations for the advection terms. The time-step limitations for 1D advection in the RK3 scheme using these advection schemes is given in Wicker and Skamarock (2002), and is reproduced here.

Time Scheme	Spatial order			
	3rd	4th	5th	6th
Leapfrog	*Unstable*	0.72	*Unstable*	0.62
RK2	0.88	*Unstable*	0.30	*Unstable*
RK3	1.61	1.26	1.42	1.08

Table 3.1: Maximum stable Courant numbers for one-dimensional linear advection. From Wicker and Skamarock (2002).

As is indicated in the table, the maximum stable Courant numbers for advection in the RK3 scheme are almost a factor of two greater than those for the leapfrog time-integration scheme. For advection in three spatial dimensions, the maximum stable Courant number is $1/\sqrt{3}$ times the Courant numbers given in Table 3.1. For stability, the time step used in the ARW should produce a maximum Courant number less than that given by theory. Thus, for 3D applications, the time step should satisfy the following equation:

$$\Delta t_{max} < \frac{Cr_{theory}}{\sqrt{3}} \cdot \frac{\Delta x}{u_{max}}, \tag{3.55}$$

where Cr_{theory} is the Courant number taken from the RK3 entry in Table 3.1 and u_{max} is the maximum velocity expected in the simulation. For example in real-data applications, where jet stream winds may reach as high as 100 ms^{-1}, the maximum time step would be approximately 80 s on a $\Delta x = 10$ km grid using 5^{th} order advection. For convection-permitting resolutions (typically $\Delta x \leq 5$ km), the vertical velocities in convective updrafts produce the stability-limiting Courant numbers. Given the additional constraint from the time splitting, and to provide a safety buffer, we usually choose a time step that is approximately 25% less than that given by (3.55). This time step is typically a factor of two greater than that used in leapfrog-based models. For those users familiar with the MM5 model, the rule of thumb for choosing a time step is that the time step, in seconds, should be approximately 3 times the horizontal grid distance, in kilometers. For the ARW, the time step (in seconds) should be approximately 6 times the grid distance (in kilometers).

3.3.2 Acoustic Time Step Constraint

The forward-backward time integration scheme used in the ARW's 2D explicit acoustic step integration allows a maximum Courant number $Cr_{max} = c_s \Delta\tau/\Delta x < 1/\sqrt{2}$, where c_s is the speed of sound. We typically use a more conservative estimate for this by replacing the limiting value $1/\sqrt{2}$ with $1/2$. Thus, the acoustic time step used in the model is

$$\Delta\tau < \frac{1}{2} \cdot \frac{\Delta x}{c_s}. \tag{3.56}$$

For example, on a $\Delta x = 10$ km grid, using a sound speed $c_s = 300$ ms^{-1}, the acoustic time step given in (3.56) is approximately 17 s. In the ARW, the ratio of the RK3 time step to the acoustic time step must be an even integer. For our example using a $\Delta x = 10$ km grid in a real-data simulation, we would specify the RK3 time step $\Delta t = 60s$ (i.e., 25% less than the 80 s step given by (3.55), and an acoustic time step $\Delta\tau = 15$ s (i.e., 1/4 of the RK3 step, rounding down the $\Delta\tau = 17$ s step given by (3.56)). Note that it is the ratio of the RK3 time step to the acoustic time step that is the required input in the ARW.

3.3.3 Adaptive Time Step

The ARW model is typically integrated with a fixed timestep, that is chosen to produce a stable integration. During any time in the integration, the maximum stable timestep is likely to be larger than the fixed timestep. In ARW Version 3, an adaptive timestepping capability was introduced that chooses the RK3 timestep based on the temporally-evolving wind fields. The adaptively-chosen timestep is usually larger than the typical fixed timestep, hence the dynamics integrates faster and physics are called less often, and the time-to-completion of the simulation can be substantially reduced.

In the adaptive timestep scheme, a target maximum Courant number Cr_{target} is chosen, where typically $1.1 \leq Cr_{target} \leq 1.2$. The maximum Courant number in the domain at a given time (Cr_{domain}), computed for all the velocity components (u, v, w), is then used to compute a new timestep. When the maximum Courant number in the domain is less than the target maximum Courant number ($Cr_{domain} < Cr_{target}$), then the timestep can be increased and the new timestep is computed using

$$\Delta t_{current} = min\left(1 + f_i, \frac{Cr_{target}}{Cr_{domain}}\right) \cdot \Delta t_{previous}, \tag{3.57}$$

where a typical value for the regulated increase is $f_i \leq 5\%$. When the computed maximum domain-wide Courant number exceeds the targeted maximum allowable Courant number ($Cr_{domain} > Cr_{target}$), then the time step is decreased to insure model stability:

$$\Delta t_{current} = max\left(1 - f_d, \frac{Cr_{target} - 0.5(Cr_{domain} - Cr_{target})}{Cr_{domain}}\right) \cdot \Delta t_{previous}, \tag{3.58}$$

where typically the factor to decrease the time step $f_d = 25\%$. Both a lower bound and an upper bound on the time step are enforced based on the initial settings of the time step suggested in section 3.3.1:

$$\Delta t_{init} = 6 \cdot \Delta x, \tag{3.59}$$

$$\Delta t_{min} = 0.5 \cdot \Delta t_{init}, \tag{3.60}$$

$$\Delta t_{max} = 3.0 \cdot \Delta t_{init}, \tag{3.61}$$

$$\Delta t = min(max(\Delta t, \Delta t_{min}), \Delta t_{max}), \tag{3.62}$$

to guard the time step from becoming too small or too large. The computation of the number of acoustic time steps n_s, described in section 3.3.2, is handled during the first of each of the RK3 model integration steps:

$$n_s = max\Big(2 \cdot \lfloor 300 \cdot \frac{\Delta t}{\Delta x} + 1 \rfloor, 4\Big). \tag{3.63}$$

For a simulation using nests, the fine-grid domain must maintain an integer number of time steps within a single model integration step from the parent. At each of the starting model integration steps for the child grid, those integration steps when the time on the fine-grid domain equals the time on the parent's domain, the adaptive time step algorithm is conducted for the fine grid. Note that the ratio of the nominal grid distance between the parent and the child does not necesarily imply that same ratio between the model integration time steps.

3.3.4 Map Projection Considerations

For ARW configurations using the Lambert conformal, polar stereographic, or Mercator projections, the timestep constraints is determined by the smallest physical horizontal grid spacing, i.e. $\min(\Delta x/m_x, \Delta y/m_y)$. For global applications, the grid distance used to determine the timestep should be $\Delta x/m_x$ evaluated at the computational latitude at which the polar filters are activated. Polar filtering is discussed in section 4.1.

Chapter 4

Turbulent Mixing and Model Filters

A number of formulations for turbulent mixing and filtering are available in the ARW solver. Some of these filters are used for numerical reasons. For example, divergence damping is used to filter acoustic modes from the solution and polar filtering is used to reduce the timestep restriction arising from the converging gridlines of the latitude-longitude grid. Other filters are meant to represent sub-grid turbulence processes that cannot be resolved on the chosen grid. These filters typically remove energy from the solution and are formulated in part on turbulence theory and observations, or represent energy sink terms in some approximation to the Euler equation. In this section, we begin by outlining the formulation and discretization of turbulent mixing processes in the ARW solver commonly associated with sub-gridscale turbulence as parameterized in cloud-scale models— the second-order horizontal and vertical mixing. In existing global models and most NWP models, vertical mixing is parameterized within the planetary boundary layer (PBL) physics. Vertical mixing parameterized within the PBL physics is described later in Chapter 8. Here we note that, when a PBL parameterization is used, all other vertical mixing is disabled. Following the outline of turbulent mixing parameterizations in this chapter, other numerical filters available in the ARW solver are described.

4.1 Latitude-Longitude Global Grid and Polar Filtering

In the ARW global model grid configuration, polar filtering is used to reduce the timestep restriction associated with the gridlines that converge as they approach the poles of the latitude-longitude grid; the converging gridlines reduce the longitudinal gridlength, and thus the stable timestep for transport, discussed in Section 3.3.1, and for acoustic waves, discussed in Section 3.3.2, will be reduced.

Polar filtering a given variable is accomplished by first applying a 1D Fourier transform to the variable on a constant computational-grid latitude circle (the forward transform), where the field is periodic. The Fourier coefficients with wavenumbers above a prescribed threshold are truncated, after which a transformation back to physical space is applied (the backward transform), completing the filter step.

A filter application can be written as

$$\hat{\phi}(k)_{filtered} = a(k)\,\hat{\phi}(k), \quad \text{for all } k,$$

where $\hat{\phi}(k)$ and $\hat{\phi}(k)_{filtered}$ are the Fourier coefficients for the generic variable ϕ before and after filtering, and $a(k)$ are the filter coefficients defined as a function of the dimensionless wavenumber k. The ARW polar filter coefficients $a(k)$ for the Fourier amplitudes are

$$a(k) = \min\left[1., \max\left(0., \left(\frac{\cos\psi}{\cos\psi_o}\right)^2 \frac{1}{\sin^2(\pi k/n)}\right)\right]$$

where ψ is the latitude on the computational grid, ψ_o is the latitude above which the polar filter is applied (the filter is applied for $|\psi| > \psi_o$), and n is the number of grid points in the latitude circle. For even n, the grid admits wavenumber $k = 0$ and dimensionless wavenumbers $\pm k$ for $k = 1 \rightarrow n/2 - 1$, and the 2Δ wave $k = n/2$. For odd n, the grid admits wavenumber $k = 0$, and dimensionless wavenumbers $\pm k$ for $k = 1 \rightarrow (n-1)/2$.

Polar filter applications within the split-explicit RK3 time integration scheme are given in Figure 3.1. Within the acoustic steps, the filter is applied to $U''^{\tau+\Delta\tau}$ and $V''^{\tau+\Delta\tau}$ immediately after the horizontal momentum is advanced, to $p_c^{\tau+\Delta\tau}$ and $\Theta_m''^{\,\tau+\Delta\tau}$ immediately after the column mass and the potential temperature are advanced, and to $W''^{\tau+\Delta\tau}$ and $\phi''^{\tau+\Delta\tau}$ after the vertically implicit part of the acoustic step is complete. The polar filter is also applied to the scalars after they are advanced every RK3 sub-step (3.1)-(3.3) and after the microphysics step.

The prognostic variables are coupled with the column mass μ when filtered, and in this way mass is conserved. An exception to this is the geopotential ϕ which is filtered without being coupled. The Fourier filtering is conservative, but it is not monotonic or positive definite. As noted in the ARW stability discussion in Section 3.3.4, timestep stability should be based on the longitudinal gridlength where the polar filters are activated, $(\Delta x/m_x)|_{\psi_o}$. The positive definite transport option, presented in Section 3.2.3, will not necessarily produce positive-definite results because of the converging gridlines and should not be used.

4.2 Explicit Spatial Diffusion

The ARW solver has three formulations for spatial diffusion on coordinate surfaces, diffusion in physical (x, y, z) space, and a sixth-order diffusion applied on horizontal coordinate surfaces. In the following sections we present the diffusion operators for the the first two formulations, followed by the four separate formulations that can be used to compute the eddy viscosities and a description of the prognostic turbulent kinetic energy (TKE) equation used in one set of these formulations. The sixth order spatial filter is described at the end of this section. In these formulations, the horizontal (K_h) and vertical (K_v) eddy viscosities are defined at scalar points on the staggered model grid.

4.2.1 Horizontal and Vertical Diffusion on Coordinate Surfaces

For any model variable, horizontal and vertical second order spatial filtering on model coordinate surfaces is considered part of the RHS terms in the continuous equations (2.8) – (2.14) and can be expressed as follows for a model variable a:

$$\partial_t(\mu_d a) = \ldots\ + \mu_d\big[m_x\partial_x(m_x K_h \partial_x a) + m_y\partial_y(m_y K_h \partial_y a)\big] + g^2(\mu_d\alpha)^{-1}\partial_\eta(K_v\alpha^{-1}\partial_\eta a). \qquad (4.1)$$

For the horizontal and vertical momentum equations, (4.1) is spatially discretized as

$$\begin{aligned}
\partial_t U &= \ldots \; + \overline{\mu_d}^{x}\overline{m_x}^{x}\big[\delta_x(m_x K_h \delta_x u) + \delta_y(\overline{m_y}^{xy}\overline{K_h}^{xy}\delta_y u)\big] + m_y^{-1} g^2 (\overline{\mu_d}^{x}\overline{\alpha}^{x})^{-1}\delta_\eta(\overline{K_v}^{x\eta}(\overline{\alpha}^{x\eta})^{-1}\delta_\eta u),\\
\partial_t V &= \ldots \; + \overline{\mu_d}^{y}\overline{m_y}^{y}\big[\delta_x(\overline{m_x}^{xy}\overline{K_h}^{xy}\delta_x v) + \delta_y(m_y K_h \delta_y v)\big] + m_x^{-1} g^2 (\overline{\mu_d}^{y}\overline{\alpha}^{y})^{-1}\delta_\eta(\overline{K_v}^{y\eta}(\overline{\alpha}^{y\eta})^{-1}\delta_\eta v),\\
\partial_t W &= \ldots \; + \mu_d m_x\big[\delta_x(\overline{m_x}^{x}\overline{K_h}^{x\eta}\delta_x w) + \delta_y(\overline{m_y}^{y}\overline{K_h}^{y\eta}\delta_y w)\big] + m_y^{-1} g^2 (\mu_d\overline{\alpha}^{\eta})^{-1}\delta_\eta(K_v\alpha^{-1}\delta_\eta w).
\end{aligned}$$

The spatial discretization for a scalar q, defined at the mass points, is

$$\partial_t(\mu_d q) = \ldots \; + \mu_d m_x m_y\big[\delta_x(\overline{m_x}^{x}P_r^{-1}\overline{K_h}^{x}\delta_x q) + \delta_y(\overline{m_y}^{y}P_r^{-1}\overline{K_h}^{y}\delta_y q)\big] + g^2(\mu_d\alpha)^{-1}\delta_\eta(\overline{K_v}^{\eta}(\overline{\alpha}^{\eta})^{-1}\delta_\eta q).$$

In the current ARW formulation for mixing on coordinate surfaces, the horizontal eddy viscosity K_h is allowed to vary in space, whereas the vertical eddy viscosity does not vary in space; hence there is no need for any spatial averaging of K_v. Additionally, note that the horizontal eddy viscosity K_h is multiplied by the inverse turbulent Prandtl number P_r^{-1} for horizontal scalar mixing.

4.2.2 Horizontal and Vertical Diffusion in Physical Space

Coordinate Metrics

We use the geometric height coordinate in this physical space formulation. The coordinate metrics are computed using the prognostic geopotential in the ARW solver. At the beginning of each Runge-Kutta time step, the coordinate metrics are evaluated as part of the overall algorithm. The definitions of the metrics are

$$z_x = g^{-1}\delta_x\phi \text{ and } z_y = g^{-1}\delta_y\phi.$$

These metric terms are defined on w levels, and (z_x, z_y) are horizontally coincident with (u,v) points. Additionally, the vertical diffusion terms are evaluated directly in terms of the geometric height, avoiding the need for metric terms in the vertical.

Continuous Equations

The continuous equations for evaluating diffusion in physical space, using the velocity stress tensor, are as follows for horizontal and vertical momentum:

$$\partial_t U = \ldots \; - m_x\big[\partial_x\tau_{11} + \partial_y\tau_{12} - z_x\partial_z\tau_{11} - z_y\partial_z\tau_{12}\big] - \partial_z\tau_{13} \tag{4.2}$$

$$\partial_t V = \ldots \; - m_y\big[\partial_x\tau_{12} + \partial_y\tau_{22} - z_x\partial_z\tau_{12} - z_y\partial_z\tau_{22}\big] - \partial_z\tau_{23} \tag{4.3}$$

$$\partial_t W = \ldots \; - m_y\big[\partial_x\tau_{13} + \partial_y\tau_{23} - z_x\partial_z\tau_{13} - z_y\partial_z\tau_{23}\big] - \partial_z\tau_{33}. \tag{4.4}$$

The stress tensor τ can be written as follows:

$$\begin{aligned}
\tau_{11} &= -\mu_d K_h D_{11}\\
\tau_{22} &= -\mu_d K_h D_{22}\\
\tau_{33} &= -\mu_d K_h D_{33}\\
\tau_{12} &= -\mu_d K_h D_{12}\\
\tau_{13} &= -\mu_d K_v D_{13}\\
\tau_{23} &= -\mu_d K_v D_{23}.
\end{aligned}$$

Symmetry sets the remaining tensor values; $\tau_{21}=\tau_{12}$, $\tau_{31}=\tau_{13}$, and $\tau_{32}=\tau_{23}$. The stress tensor τ is calculated from the deformation tensor D. The continuous deformation tensor is defined as

$$\begin{aligned}
D_{11} &= 2\,m_x m_y\big[\partial_x(m_y^{-1}u) - z_x\partial_z(m_y^{-1}u)\big]\\
D_{22} &= 2\,m_x m_y\big[\partial_y(m_x^{-1}v) - z_y\partial_z(m_x^{-1}v)\big]\\
D_{33} &= 2\,\partial_z w\\
D_{12} &= m_x m_y\big[\partial_y(m_y^{-1}u) - z_y\partial_z(m_y^{-1}u) + \partial_x(m_x^{-1}v) - z_x\partial_z(m_x^{-1}v)\big]\\
D_{13} &= m_x m_y\big[\partial_x(m_y^{-1}w) - z_x\partial_z(m_y^{-1}w)\big]+\partial_z(u)\\
D_{23} &= m_x m_y\big[\partial_y(m_y^{-1}w) - z_y\partial_z(m_y^{-1}w)\big]+\partial_z(v).
\end{aligned}$$

The deformation tensor is symmetric, hence $D_{21}=D_{12}$, $D_{31}=D_{13}$, and $D_{32}=D_{23}$.

The diffusion formulation for scalars is

$$\begin{aligned}
\partial_t(\mu_d q) = \ldots\ + \big[\, & m_x\big(\partial_x - \partial_z z_x\big)\big(\mu_d m_x K_h(\partial_x - z_x\partial_z)\big)+\\
& m_y\big(\partial_y - \partial_z z_y\big)\big(\mu_d m_y K_h(\partial_y - z_y\partial_z)\big) + \partial_z\mu_d K_v\partial_z\big]q.
\end{aligned} \tag{4.5}$$

Spatial Discretization

Using the definition of the stress tensor, the spatial discretization of the ARW physical-space diffusion operators for the horizontal and vertical momentum equations (4.2) - (4.4) are

$$\begin{aligned}
\partial_t U &= \ldots\ - \overline{m_x}^{x}\big[\delta_x\tau_{11} + \delta_y\tau_{12} - \overline{z_x}^{\eta}\delta_z\overline{\tau_{11}}^{x\eta} - \overline{z_y}^{xy\eta}\delta_z\overline{\tau_{12}}^{y\eta}\big] - \delta_z\tau_{13}\\
\partial_t V &= \ldots\ - \overline{m_y}^{y}\big[\delta_y\tau_{22} + \delta_x\tau_{12} - \overline{z_y}^{\eta}\delta_z\overline{\tau_{22}}^{y\eta} - \overline{z_x}^{xy\eta}\delta_z\overline{\tau_{12}}^{x\eta}\big] - \delta_z\tau_{23}\\
\partial_t W &= \ldots\ - m_x\big[\delta_x\tau_{13} + \delta_y\tau_{23} - \overline{z_x}^{x}\delta_z\overline{\tau_{13}}^{x\eta} - \overline{z_y}^{y}\delta_z\overline{\tau_{23}}^{y\eta}\big] - \delta_z\tau_{33}.
\end{aligned}$$

The discrete forms of the stress tensor and deformation tensor are

$$\begin{aligned}
\tau_{11} &= -\mu_d K_h D_{11}\\
\tau_{22} &= -\mu_d K_h D_{22}\\
\tau_{33} &= -\mu_d K_h D_{33}\\
\tau_{12} &= -\overline{\mu_d}^{xy}\,\overline{K_h}^{xy} D_{12}\\
\tau_{13} &= -\overline{\mu_d}^{x}\,\overline{K_v}^{x\eta} D_{13}\\
\tau_{23} &= -\overline{\mu_d}^{y}\,\overline{K_v}^{y\eta} D_{23},
\end{aligned}$$

and

$$\begin{aligned}
D_{11} &= 2\,m_x m_y\big[\delta_x(\overline{m_y^{-1}}^{x}u) - \overline{z_x}^{x\eta}\delta_z(\overline{m_y^{-1}}^{x}u)\big]\\
D_{22} &= 2\,m_x m_y\big[\delta_y(\overline{m_x^{-1}}^{y}v) - \overline{z_y}^{x\eta}\delta_z(\overline{m_x^{-1}}^{y}v)\big]\\
D_{33} &= 2\,\delta_z w\\
D_{12} &= (\overline{m_x m_y}^{xy})\left[\delta_y(\overline{m_y^{-1}}^{x}u) - \overline{z_y}^{x\eta}\delta_z\overline{(\overline{m_y^{-1}}^{x}u)}^{y\eta} + \delta_x(\overline{m_x^{-1}}^{y}v) - \overline{z_x}^{y\eta}\delta_z\overline{(\overline{m_x^{-1}}^{y}v)}^{x\eta}\right]\\
D_{13} &= m_x m_y\left[\delta_x(m_y^{-1}w) - z_x\delta_z\overline{(m^{-1}w)}^{x\eta}\right]+\delta_z u\\
D_{23} &= m_x m_y\left[\delta_y(m_y^{-1}w) - z_y\delta_z\overline{(m_y^{-1}w)}^{y\eta}\right]+\delta_z v.
\end{aligned}$$

The spatial discretization for the scalar diffusion (4.5) is

$$\begin{aligned}\partial_t(\mu_d q) = \ldots \; & + m_x\left[\delta_x\left(\overline{\mu_d}^{x} H_1(q)\right) - \mu_d \overline{z_x}^{x\eta}\delta_z\left(\overline{H_1(q)}^{x\eta}\right)\right] \\ & + m_y\left[\delta_y\left(\overline{\mu_d}^{y} H_2(q)\right) - \mu_d \overline{z_y}^{y\eta}\delta_z\left(\overline{H_2(q)}^{y\eta}\right)\right] \\ & + \mu_d \delta_z\left(\overline{K_v}^{\eta}\delta_z q\right),\end{aligned}$$

where

$$\begin{aligned}H_1(q) &= \overline{m_x}^{x}\overline{K_h}^{x}\left(\delta_x q - z_x\delta_z(\overline{q}^{x\eta})\right), \\ H_2(q) &= \overline{m_y}^{y}\overline{K_h}^{y}\left(\delta_y q - z_y\delta_z(\overline{q}^{y\eta})\right).\end{aligned}$$

4.2.3 Computation of the Eddy Viscosities

There are four options for determining the eddy viscosities K_h and K_v in the ARW solver.

External specification of K_h and K_v

Constant values for K_h and K_v can be input in the ARW namelist.

K_h determined from the horizontal deformation

The horizontal eddy viscosity K_h can be determined from the horizontal deformation using a Smagorinsky first-order closure approach. In this formulation, the eddy viscosity is defined and discretized as

$$K_h = C_s^2\, l^2\left[0.25(D_{11} - D_{22})^2 + \overline{D_{12}^2}^{xy}\right]^{\frac{1}{2}}.$$

The deformation tensor components have been defined in the previous section. The length scale $l = (\Delta x \Delta y)^{1/2}$ and C_s is a constant with a typical value $C_s = 0.25$. For scalar mixing, the eddy viscosity is divided by the turbulent Prandtl number P_r that typically has a value of 1/3 (Deardorff, 1972). This option is most often used with a planetary boundary layer scheme that independently handles the vertical mixing.

3D Smagorinsky Closure

The horizontal and vertical eddy viscosities can be determined using a 3D Smagorinsky turbulence closure. This closure specifies the eddy viscosities as

$$K_{h,v} = C_s^2\, l_{h,v}^2 \max\left[0., \left(D^2 - P_r^{-1}N^2\right)^{\frac{1}{2}}\right], \tag{4.6}$$

where

$$D^2 = \frac{1}{2}\left[D_{11}^2 + D_{22}^2 + D_{33}^2\right] + \left(\overline{D_{12}}^{xy}\right)^2 + \left(\overline{D_{13}}^{x\eta}\right)^2 + \left(\overline{D_{23}}^{y\eta}\right)^2,$$

and N is the Brunt-Väisälä frequency; the computation of N, including moisture effects, is outlined in Section 4.2.4.

Two options are available for calculating the mixing length $l_{h,v}$ in (4.6). An isotropic length scale (appropriate for $\Delta x, \Delta y \simeq \Delta z$) can be chosen where $l_{h,v} = (\Delta x \Delta y \Delta z)^{1/3}$ and thus $K_h = K_v = K$. The anisotropic option (appropriate for $\Delta x, \Delta y >> \Delta z$) sets the horizontal mixing length $l_h = \sqrt{\Delta x \Delta y}$ in the calculation of the horizontal eddy viscosity K_h using (4.6), and $l_v = \Delta z$ for the calculation of the vertical eddy viscosity K_v using (4.6).

Additionally, the eddy viscosities for scalar mixing are divided by the turbulent Prandtl number $P_r = 1/3$.

Prognostic TKE Closure

For the predicted turbulent kinetic energy option (TKE; see section 4.2.4), the eddy viscosities are computed using

$$K_{h,v} = C_k l_{h,v} \sqrt{e},$$

where e is the turbulent kinetic energy (a prognostic variable in this scheme), C_k is a constant (typically $0.15 < C_k < 0.25$), and l is a length scale.

If the isotropic mixing option is chosen then the horizontal and vertical eddy viscosities are equivalent and the length scale is defined as

$$\begin{aligned} l_{h,v} &= \min\left[(\Delta x \Delta y \Delta z)^{1/3}, 0.76\sqrt{e}/N\right] && \text{for } N^2 > 0, \\ l_{h,v} &= (\Delta x \Delta y \Delta z)^{1/3} && \text{for } N^2 \leq 0, \end{aligned}$$

(see section 4.2.4 for the calculation of N^2). Both the horizontal and vertical eddy viscosities are multiplied by an inverse turbulent Prandtl number $P_r^{-1} = 1 + 2l/(\Delta x \Delta y \Delta z)^{1/3}$ for scalar mixing.

If the anisotropic mixing option is chosen, then $l_h = \sqrt{\Delta x \Delta y}$ for the calculation of K_h. For calculating K_v,

$$\begin{aligned} l_v &= \min\left[\Delta z, 0.76\sqrt{e}/N\right] && \text{for } N^2 > 0, \\ l_v &= \Delta z && \text{for } N^2 \leq 0. \end{aligned}$$

The eddy viscosity used for mixing scalars is divided by a turbulent Prandtl number P_r. The Prandtl number is 1/3 for the horizontal eddy viscosity K_h, and $P_r^{-1} = 1 + 2l/\Delta z$ for the vertical eddy viscosity K_v.

4.2.4 TKE equation for the 1.5 Order Turbulence Closure

The prognostic equation governing the evolution of the turbulent kinetic energy e is

$$\partial_t(\mu_d e) + \nabla \cdot \mathbf{V} e = \mu_d(\text{ shear production } + \text{ buoyancy } + \text{ dissipation }). \tag{4.7}$$

The time integration and the transport terms in (4.7) are integrated in the same manner as for other scalars (as described in Chapter 3). The right-hand side source and sink terms for e are given as follows.

Shear Production

The shear production term in (4.7) can be written as

$$\text{shear production} = K_h D_{11}^2 + K_h D_{22}^2 + K_v D_{33}^2 + K_h \overline{D_{12}^2}^{xy} + K_v \overline{D_{13}^2}^{x\eta} + K_v \overline{D_{23}^2}^{y\eta}.$$

Buoyancy

The buoyancy term in the TKE equation (4.7) is written as

$$\text{buoyancy} = -K_v N^2,$$

where the Brunt-Väisälä frequency N is computed using either the formula for a moist saturated or unsaturated environment:

$$\begin{aligned} N^2 &= g\big[A\partial_z\theta_e - \partial_z q_w\big] && \text{if } q_v \geq q_{vs} \text{ or } q_c \geq 0.01 \text{ g/Kg;} \\ N^2 &= g\left[\frac{1}{\theta}\partial_z\theta + 1.61\partial_z q_v - \partial_z q_w\right] && \text{if } q_v < q_{vs} \text{ or } q_c < 0.01 \text{ g/Kg.} \end{aligned}$$

The coefficient A is defined as

$$A = \theta^{-1}\frac{1 + \frac{1.61\epsilon L q_v}{R_d T}}{1 + \frac{\epsilon L^2 q_v}{C_p R_v T^2}},$$

where q_w represents the total water (vapor + all liquid species + all ice species), L is the latent heat of condensation and ϵ is the ratio of the molecular weight of water vapor to the molecular weight of dry air. θ_e is the equivalent potential temperature and is defined as

$$\theta_e = \theta\left(1 + \frac{L q_{vs}}{C_p T}\right),$$

where q_{vs} is the saturation vapor mixing ratio.

Dissipation

The dissipation term in (4.7) is

$$\text{dissipation} = -\frac{C e^{3/2}}{l},$$

where

$$C = 1.9\,C_k + \frac{\max(0,\, 0.93 - 1.9\,C_k)\,l}{\Delta s},$$

$$\Delta s = (\Delta x \Delta y \Delta z)^{1/3},$$

and

$$l = min\big[(\Delta x \Delta y \Delta z)^{1/3}, 0.76\sqrt{e}/N\big].$$

4.2.5 Sixth-Order Spatial Filter on Coordinate Surfaces

A sixth order spatial filter is available that is applied on horizontal coordinate surfaces. The diffusion scheme is that proposed by Xue (2000). Its application in the ARW is described by Knievel et al. (2007). With the release of WRF Version 4, the 6th order filter was recast into conservative form and an optional limiter for diffusive fluxes based on the coordinate surface slope was introduced. For the staggered velocities u and v, and for the cell centered variables a, the filter can be expressed as

$$\partial_t(\mu_d u) = \cdots\ \beta \frac{2^{-6}}{2\Delta t} \Big[\Delta x^6\, \overline{m_x}^x \delta_x\big(\mu_d F_x(u)\big) + \Delta y^6\, \overline{m_y}^x \delta_y\big(\overline{\mu_d}^{xy} F_y(u)\big) \Big], \tag{4.8}$$

$$\partial_t(\mu_d v) = \cdots\ \beta \frac{2^{-6}}{2\Delta t} \Big[\Delta x^6\, \overline{m_x}^y \delta_x\big(\overline{\mu_d}^{xy} F_x(v)\big) + \Delta y^6\, \overline{m_y}^y \delta_y\big(\mu_d F_y(v)\big) \Big], \tag{4.9}$$

$$\partial_t(\mu_d a) = \cdots\ \beta \frac{2^{-6}}{2\Delta t} \Big[\Delta x^6\, m_x \delta_x\big(\overline{\mu_d}^x F_x(a)\big) + \Delta y^6\, m_y \delta_y\big(\overline{\mu_d}^y F_y(a)\big) \Big]. \tag{4.10}$$

β is a user-specified filtering coefficient representing the damping applied to 2Δ waves for each filter application. The diffusive fluxes $\Delta x^5 F_x = \Delta x^5 \delta_x^5(a)$, i.e.

$$\Delta x^5 F_x(a)\Big|_{i+1/2} = \gamma_s \Big\{ 10\big[a(i+1) - a(i)\big] - 5\big[a(i+2) - a(i-1)\big] + \big[a(i+3) - a(i-2)\big] \Big\}.$$

γ_s is a flux limiting factor that reduces the diffusive flux where the terrain slope is steep. $\gamma_s = 1$ if the limiter is inactive. When activated by the user, the flux limiting factor

$$\gamma_s = \max\left(1 - \left| \left(\frac{\partial z}{\partial x}\right) \left(\frac{\partial z}{\partial x}\right)_{cr}^{-1} \right|, 0 \right).$$

(dz/dx) is the slope of the coordinate surface, and it is approximated using the reference state geopotential in WRF. $(dz/dx)_{cr}$ is a user specified critical value of the coordinate surface slope at which the diffusive flux is completely removed. By design, $0 \leq \gamma_s \leq 1$.

The user can choose to enforce monotonicity in the filtering. In the monotonic option, the diffusive fluxes are set to zero if the diffusion is up-gradient, e.g. $F_x(a) = 0$ if $F_x(a)\, \delta_x(a) < 0$ and $F_y(a) = 0$ if $F_y(a)\, \delta_y(a) < 0$.

Note that the diffusive fluxes are computed in computational space; map factors are not taken into account except in the flux divergence terms in (4.8) - (4.10) where they serve to guarantee scalar mass conservation. The filter parameter β is dimensionless, thus the filter scales with the timestep and gridsize. This explicit diffusion acts on all three components of wind, potential temperature, all moisture variables and passive scalars, and subgrid turbulence kinetic energy. Further details can be found in Knievel et al. (2007).

4.3 Filters for the Time-split RK3 scheme

Three filters are used in the ARW time-split RK3 scheme apart from those in the model physics: three-dimensional divergence damping (an acoustic model filter); an external-mode filter that damps vertically-integrated horizontal divergence; and off-centering of the vertically implicit integration of the vertical momentum equation and geopotential equation. Each of these is described in the following sections.

4.3.1 Three-Dimensional Divergence Damping

The damping of the full mass divergence is a filter for acoustic modes in the ARW solver. This 3D mass divergence damping is described in Skamarock and Klemp (1992). The filtering is accomplished by forward weighting the pressure update in the acoustic step loop described in Section 3.1.3, step (6). The linearized equation of state (3.5) is used to diagnose the pressure at the new time τ after the U'', V'', μ_d'', and Θ_m'' have been advanced. Divergence damping consists of using a modified pressure in the computation of the pressure gradient terms in the horizontal momentum equations in the acoustic steps (Equations (3.7) and (3.8)). Denoting the updated value as p^τ, the modified pressure $p^{*\tau}$ used in (3.7) and (3.8) can be written as

$$p^{*\tau} = p^\tau + \gamma_d \big(p^\tau - p^{\tau - \Delta\tau} \big), \tag{4.11}$$

where γ_d is the damping coefficient. This modification is equivalent to inserting a horizontal diffusion term into the equation for the 3D mass divergence, hence the name *divergence damping*. A divergence damping coefficient $\gamma_d = 0.1$ is typically used in the ARW applications, independent of time step or grid size.

4.3.2 External Mode Filter

The external modes in the solution are damped by filtering the vertically-integrated horizontal divergence. This damping is accomplished by adding a term to the horizontal momentum equations. The additional term added to (3.7) and (3.8) are

$$\delta_\tau U'' = \ldots\; - \gamma_e \frac{\Delta x^2}{\Delta\tau} \delta_x (\delta_{\tau - \Delta\tau} \mu_d'') \tag{4.12}$$

and

$$\delta_\tau V'' = \ldots\; - \gamma_e \frac{\Delta y^2}{\Delta\tau} \delta_y (\delta_{\tau - \Delta\tau} \mu_d''). \tag{4.13}$$

The quantity $\delta_{\tau-\Delta\tau}\mu$ is the vertically-integrated mass divergence (i.e., (3.20)) from the previous acoustic step (that is computed using the time τ values of U and V), and γ_e is the external mode damping coefficient. An external mode damping coefficient $\gamma_e = 0.01$ is typically used in the ARW applications, independent of time step or grid size.

4.3.3 Semi-Implicit Acoustic Step Off-centering

Forward-in-time weighting of the vertically-implicit acoustic-time-step terms damps instabilities associated vertically-propagating sound waves. The forward weighting also damps instabilities associated with sloping model levels and horizontally propagating sound waves (see Durran and Klemp, 1983; Dudhia, 1995). The off-centering is accomplished by using a positive (non-zero) coefficient β (3.19) in the acoustic time-step vertical momentum equation (3.11) and geopotential equation (3.12). An off-centering coefficient $\beta = 0.1$ is typically used in the ARW applications, independent of time step or grid size.

4.4 Formulations for Gravity Wave Absorbing Layers

There are three formulations for absorbing vertically-propagating gravity waves so as to prevent unphysical wave reflection off the domain upper boundary from contaminating ARW solutions.

4.4.1 Absorbing Layer Using Spatial Filtering

This formulation of the absorbing layer increases the second-order horizontal and vertical eddy viscosities in the absorbing layer using the following formulation:

$$K_{dh} = \frac{\Delta x^2}{\Delta t}\gamma_g \cos\left(\frac{\pi}{2}\,\frac{z_{top} - z}{z_d}\right),$$

and

$$K_{dv} = \frac{\Delta z^2}{\Delta t}\gamma_g \cos\left(\frac{\pi}{2}\,\frac{z_{top} - z}{z_d}\right).$$

Here γ_g is a user-specified damping coefficient, z_{top} is the height of the model top for a particular grid column, z_d is the depth of the damping layer (from the model top), and K_{dh} and K_{dv} are the horizontal and vertical eddy viscosities for the wave absorbing layer. If other spatial filters are being used, then the eddy viscosities that are used for the second-order horizontal and vertical eddy viscosities are the maximum of (K_h, K_{dh}) and (K_v, K_{dv}). The effect of this filter on gravity waves is discussed in Klemp and Lilly (1978), where guidance on the choice of the damping coefficient γ_g can also be found.

4.4.2 Implicit Rayleigh Damping for the Vertical Velocity

Implicitly damping the vertical velocity within the implicit solution algorithm for the vertically propagating acoustic modes has been found to be a very effective and robust absorbing layer formulation by Klemp et al. (2008). We recommend its use in both large-scale and small-scale applications, and in idealized and real-data applications. It has proven more effective than the spatial-filter-based absorbing layer described in Section 4.4.1, and it is more effective and more generally applicable than traditional Rayleigh damping because of its implicit nature and the fact that it does not need a reference state. This formulation was introduced in WRFV3. It can only be used with the nonhydrostatic dynamics option.

In the vertically-implicit solution procedure for $W''^{\tau+\Delta\tau}$ and $\phi''^{\tau+\Delta\tau}$ in the acoustic step (step 5 in Figure 3.1), equation (3.12) is used to eliminate $\phi''^{\tau+\Delta\tau}$ from (3.11) after which the tridiagonal equation in the vertical direction for $W''^{\tau+\Delta\tau}$ is solved. Afterwards $\phi''^{\tau+\Delta\tau}$ is recovered using (3.12). In the solution procedure that includes the implicit Rayleigh damping for W, after the tridiagonal equation for W'' is solved and before the geopotential ϕ is updated, the implicit Rayleigh damping is included by calculating $W''^{\tau+\Delta\tau}$ using

$$W''^{\tau+\Delta\tau} = \tilde{W}''^{\tau+\Delta\tau} - \tau(z)\Delta\tau W''^{\tau+\Delta\tau} \tag{4.14}$$

where $\tilde{W}''^{\tau+\Delta\tau}$ is the solution to (3.11). The geopotential is then updated as usual using (3.12) with the updated damped vertical velocity from (4.14). The perturbation pressure and specific volume are computed as before using (3.5) and (3.4).

The variable $\tau(z)$ defines the vertical structure of the damping layer, and has a form similar to the Rayleigh damper in Durran and Klemp (1983) and also used in the traditional Rayleigh damping formulation discussed in Section 4.4.3

$$\tau(z) = \begin{cases} \gamma_r \sin^2\left[\frac{\pi}{2}\left(1 - \frac{z_{top}-z}{z_d}\right)\right] & \text{for } z \geq (z_{top} - z_d); \\ 0 & \text{otherwise,} \end{cases}$$

where γ_r is a user specified damping coeficient, z_{top} is the height of the model top for a particular grid column, and z_d is the depth of the damping layer (from the model top). A typical value for the damping coefficient for this formulation is $\gamma_r = 0.2\, s^{-1}$ ($\sim 10N$ for typical stratospheric values of the Brunt-Väisällä frequency). A complete analysis of this filter can be found in Klemp et al. (2008).

4.4.3 Traditional Rayleigh Damping Layer

A traditional Rayleigh damping layer is also available in the ARW solver. This scheme applies a tendency to u, v, w, and θ to gradually relax the variable back to a predetermined reference state value,

$$\begin{aligned} \partial_t u &= -\tau(z)\left(u - \overline{u}\right), \\ \partial_t v &= -\tau(z)\left(v - \overline{v}\right), \\ \partial_t w &= -\tau(z) w, \\ \partial_t \theta &= -\tau(z)\left(\theta - \overline{\theta}\right). \end{aligned}$$

Overbars indicate the reference state fields, which are functions of z only and are typically defined as the initial horizontally homogeneous fields in idealized simulations. The reference state vertical velocity is assumed to be zero. The vertical structure of the damping layer is the same as that used for the implicit vertical velocity damping described in Section 4.4.2. Because the model surfaces change height with time in the ARW solver, the reference state values at each grid point need to be recalculated at every time step. Thus, a linear interpolation scheme is used to calculate updated reference state values based on the height of the model levels at each time step.

The effect of this filter on gravity waves is discussed in Klemp and Lilly (1978), where guidance on the choice of the damping coefficeint γ_r can also be found.

4.5 Other Damping

4.5.1 Vertical-Velocity Damping

This is also called w-damping. In semi-operational or operational NWP applications, the model robustness can be improved by detecting locations where the vertical motion approaches the limiting Courant number for stability, and applying a Rayleigh damping term in the vertical momentum equation to stabilize the motion. This term is non-physical and should only be used in the situation where many, or long, model runs are being done, and there is no option for a re-run with a shorter time-step if a failure occurs due to an excessively strong updraft. This might be the case, for example, in an operational setting where real-time forecasts have to be produced on time to be useful. However, if this term activates frequently, consideration should be given to reducing the model time-step.

The term is calculated from

$$Cr = \left|\frac{\Omega dt}{\mu d\eta}\right|.$$

If $Cr > Cr_\beta$, then

$$\partial_t W = ... - \mu_d \; \text{sign}(W)\gamma_w (Cr - Cr_\beta),$$

where γ_w is the damping coefficient (typically 0.3 ms^{-2}), and Cr_β is the activation Courant number (typically 1.0). The ARW outputs the location of this damping when it is active.

Chapter 5

Initial Conditions

ARW may be run with user-defined initial conditions for idealized simulations, or it may be run using interpolated data from either an external analysis or forecast for real-data cases. Both 2D and 3D test cases are provided for idealized simulations. Several sample cases are provided for real-data simulations, which rely on pre-processing from an external package (usually the WRF Preprocessing System, referred to as WPS) that converts the large-scale GRIB-formatted data into an intermediate format suitable for ingest by the ARW's real-data processor.

The programs that generate the specific initial conditions for the selected idealized or real-data case function similarly. They provide ARW with:

- input data that are correctly staggered for the horizontal and vertical grid;
- hydrostatically balanced reference state and perturbation fields; and
- metadata specifying such information as the date, grid physical characteristics, and projection details.

Neither idealized nor real-data cases use observations to enhance their initial conditions; however, output from the ARW system initial condition program is suitable as input to the WRF Variational Data Assimilation package (see Chapter 11).

5.1 Initialization for Idealized Conditions

Table 5.1 summarizes the names of the ARW ideal test cases that utilize various assumptions of idealized environments. These test cases include a single column model (em_scm_xy), large eddy simulations (em_les), ground fire simulations (em_fire), sea breezes (em_seabreeze2d_x), mountain waves (em_hill2d_x), squall lines (em_squall2d_x, em_squall2d_y), supercell thunderstorms (em_quarter_ss), gravity currents (em_grav2d_x), baroclinic waves (em_b_wave), tropical cyclones (em_tropical_cyclone), convective-radiation equilibrium (em_convrad), and global domains (em_heldsuarez). A brief description of these test cases can be found in the doc/README˙test_cases file provided in the ARW release. Test cases include examples of atmospheric flow at fine scales (e.g., the LES test case has a grid-spacing of 100 meters and a time step of 1 second) and at large scales (e.g., the Held Suarez global test case uses a grid-spacing around 600 km and a time step of 1800 s), in addition to traditional mesoscale and cloud-scale model simulations. The test suite allows an ARW user to easily reproduce these known solutions. The test suite is also the starting point for constructing personalized idealized flow simulations by modifying the existing initializations that closely resemble a desired initialization.

Table 5.1: Ideal Cases. Listed are the available idealized cases for the Advanced Research WRF.

1D	2D	3D
em_scm_xy	em_grav2d_x	em_b_wave
	em_hill2d_x	em_convrad
	em_seabreeze2d_x	em_fire
	em_squall2d_x	em_heldsuarez
	em_squall2d_y	em_les
		em_quarter_ss
		em_tropical_cyclone

Initial conditions for the Held-Suarez test case are analytically defined in the initialization routines. Other than the baroclinic wave case that utilizes a binary file providing a 2D profile specified in $[y, z]$, the remaining idealized ARW cases use as input a 1D sounding specified as a function of geometric height z. The text file defining this 1D sounding may be directly edited by the user. The 1D specification of the sounding in these test files requires surface values of pressure, potential temperature, and water vapor mixing ratio, followed by potential temperature, vapor mixing ratio, and horizontal wind components at some heights above the surface. Initialization programs for each case assume that this moist sounding represents an atmosphere in hydrostatic balance.

Two sets of thermodynamic fields are needed for the model— the reference state and the perturbation state (see Chapter 2 for discussion of the equations). The reference state used in idealized initializations is computed using the input sounding from which moisture is discarded (because the reference state is dry). The perturbation state is computed using the full moist input sounding. The procedure for computing the hydrostatically-balanced ARW reference state and perturbation state variables from the input sounding are as follows. First, density and both a dry and full hydrostatic pressure are computed from the input sounding at the input sounding levels z. This is accomplished by integrating the hydrostatic equation vertically up the column using the surface pressure and potential temperature as the lower boundary condition. The hydrostatic equation is

$$\delta_z p = -\overline{\rho}_d{}^z g(1 + \overline{q}_v{}^z), \tag{5.1}$$

where $\overline{\rho_d}^z$ is a two-point average between input sounding levels, and $\delta_z p$ is the difference of the pressure between input sounding levels, divided by the height difference. Additionally, the equation of state is needed to close the system:

$$\alpha_d = \frac{1}{\rho_d} = \frac{R_d \theta_m}{p_o} \left(\frac{p}{p_o} \right)^{-\frac{c_v}{c_p}}, \tag{5.2}$$

where q_v and θ_m are given in the input sounding. (5.1) and (5.2) are a coupled set of nonlinear equations for p and ρ in the vertical integration, solved by iteration. Dry pressure on input sounding levels is computed by integrating the hydrostatic relation down from the top, excluding the vapor component.

While the full pressure (dry, plus vapor) and dry air pressure are computed on the input sounding levels, the pressure at the model top p_t is computed by linear interpolation in height (or possibly extrapolation), using the height of the model top (which is an input variable). The column mass $p_c = p_s - p_t$ is computed by interpolating the dry air pressure to the surface, and then subtracting p_t. Given the column mass, the dry-air pressure at each η level is known from the hybrid coordinate definition (2.2), and the coordinate metric μ_d is computed from (2.6). Potential temperature from the input sounding is interpolated to each of the model pressure levels, and the equation of state (5.2) is used to compute the inverse density α_d. Finally, ARW's dry hydrostatic relation (2.15) is used to compute the geopotential. This procedure is used to compute the reference state (based on a dry atmosphere) and the full state (using the full moist sounding). Perturbation variables are computed as the difference between the full state and the reference state. It should also be noted that in the nonhydrostatic model integration, inverse density α_d is diagnosed from the geopotential using this dry hydrostatic relation, and pressure is diagnosed from the equation of state using the inverse density α_d and the prognostic potential temperature θ_m. Thus, ARW's prognostic variables μ_d, θ_m, and ϕ are in exact hydrostatic balance (to machine roundoff) with the model equations.

5.2 Initialization for Real-Data Conditions

Initial conditions for real-data cases are pre-processed through a separate package called the WRF Preprocessing System (WPS, see Fig. 5.1). Output from WPS is passed to the ARW real-data pre-processor, program *real*, which generates initial and lateral boundary conditions. This section is primarily about the steps taken to build the initial and lateral boundary conditions for a real-data case. Even though the WPS is outside of the ARW system, a brief description is appropriate to show the method for bringing raw meteorological and static terrestrial data into the model for real-data cases.

5.2.1 Use of the WRF Preprocessing System by ARW

The WPS is a set of programs that takes terrestrial and meteorological data (typically in GRIB format) and transforms them for input to the ARW pre-processor program for real-data cases (*real*). Figure 5.1 shows the flow of data into and out of WPS. The first step for the WPS is to define a physical grid (including the projection type, location on the globe, number of grid points, nest locations, and grid distances) and to interpolate static fields to the prescribed domain. Independent of the domain configuration, an external analysis or forecast is processed by the WPS GRIB decoder, which diagnoses required fields and reformats GRIB data into an internal binary format. With a specified domain, WPS horizontally interpolates meteorological data onto the projected domain(s). WPS output data (which is sent to the ARW pre-processor program for real-data cases) supplies a complete 3-dimensional snapshot of the atmosphere on the selected model grid's horizontal staggering, at the selected time slices.

Input to the ARW real-data processor from WPS contains surface and 3-dimensional fields of temperature (K), relative humidity (%), geopotential height (m), pressure (Pa), and the horizontal components of wind speed (m/s, already rotated to the model projection). The 2-dimensional static terrestrial fields include albedo, Coriolis parameters, terrain elevation, vegetation/land-use

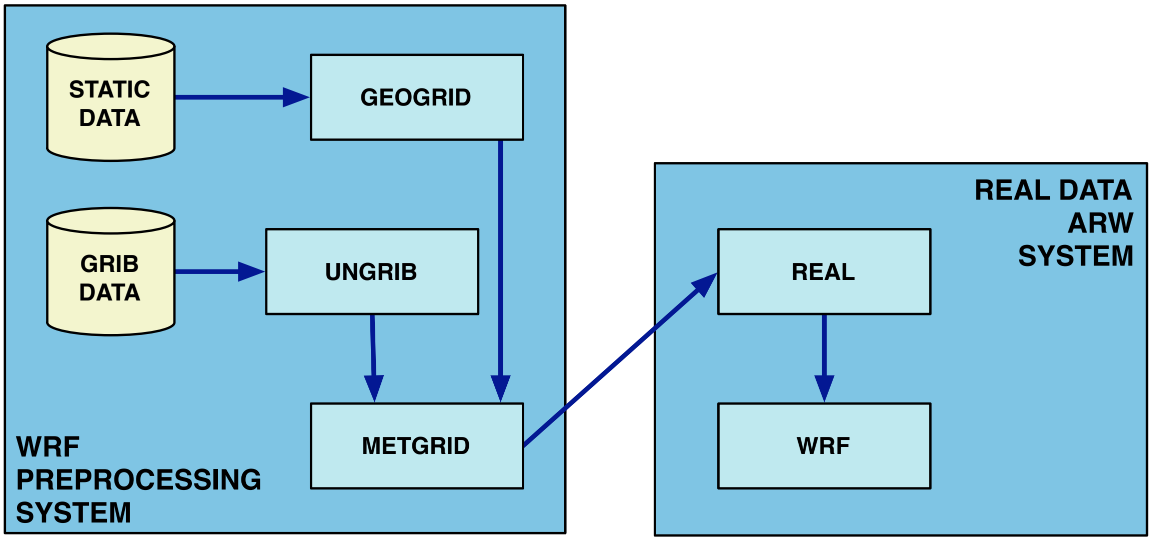

Figure 5.1: Schematic showing data flow and program components in WPS, and how WPS feeds initial data to ARW. Text in the rectangular boxes indicates program names. GEOGRID: defines the model domain and creates static files of terrestrial data. UNGRIB: decodes GRIB-formatted data. METGRID: interpolates meteorological data to the model domain.

type, land/water mask, map scale factors, map rotation angle, soil texture category, vegetation greenness fraction, annual mean temperature, and latitude/longitude. After WPS processing, the 2-dimensional time-dependent fields from the external model include surface pressure and sea-level pressure (Pa), layers of soil temperature (K) and soil moisture (kg/kg, either total moisture, or binned into total and liquid content), snow depth (m), skin temperature (K), sea surface temperature (K), and a sea ice flag.

5.2.2 Reference State

Identical to idealized initializations, there is a partitioning of some meteorological data into reference and perturbation fields. For real-data cases, the reference state is defined by terrain elevation and several user-definable constants:

- p_0 (10^5 Pa) reference sea level pressure;
- T_0 (usually 270 to 300 K) reference sea level temperature;
- A (50 K) temperature difference between the pressure levels of p_0 and p_0/e;
- T_{min} (200 K) minimum temperature permitted;
- γ_{strat} (-11 K) standard stratosphere lapse rate;
- p_{strat} (0 Pa) pressure at which stratospheric warming begins.

Using these parameters, the dry reference state surface pressure is

$$\bar{p}_s = p_0 \; exp\left(\frac{-T_0}{A} + \sqrt{\left(\frac{T_0}{A}\right)^2 - \frac{2\phi_{sfc}}{A \; R_d}} \right). \tag{5.3}$$

From (5.3), the 3-dimensional reference pressure (dry hydrostatic pressure p_d) is computed as a function of the vertical coordinate η levels and the model top p_t:

$$\overline{p}_d = B(\eta)\ (\bar{p}_s - p_t) + [\eta - B(\eta)](p_0 - p_t) + p_t. \tag{5.4}$$

With (5.4), the reference temperature, though not permitted to get colder than T_{min}, is a straight line on a skew-T plot, defined as

$$\overline{T}_d = \max\ \left(T_{min}\ ,\ T_0 + A\ ln\frac{\overline{p}_d}{p_0} \right).$$

For vertical locations where the $\overline{p}_d < p_{strat}$, the reference profile warms:

$$\overline{T}_d = T_{min} + \gamma_{strat}\ ln\frac{\overline{p}_d}{p_{strat}}.$$

The isobaric temperature and the stratospheric correction supply a reasonable reference temperature up to approximately 100 Pa. From the reference pressure and the final reference temperature, the reference potential temperature is then defined as

$$\overline{\theta}_d = \overline{T}_d \left(\frac{p_0}{\overline{p}_d}\right)^{\frac{R_d}{C_p}}, \tag{5.5}$$

and the reciprocal of the reference density using (5.4) and (5.5) is given by

$$\overline{\alpha}_d = \frac{1}{\overline{\rho}_d} = \frac{R_d\ \overline{\theta}_d}{p_0} \left(\frac{\overline{p}_d}{p_0}\right)^{-\frac{C_v}{C_p}}. \tag{5.6}$$

Using (5.4), the base state coordinate metric is given as

$$\bar{\mu}_d = \frac{\partial \bar{p}_d}{\partial \eta} = B_\eta(\eta)(\bar{p}_s - p_t) + \big[1 - B_\eta(\eta)\big](p_0 - p_t). \tag{5.7}$$

From (5.6) and (5.7), the reference state geopotential defined from the hydrostatic relation is

$$\delta_\eta \overline{\phi} = -\overline{\alpha}_d\ \overline{\mu}_d.$$

5.2.3 Vertical Interpolation and Extrapolation

The ARW real-data preprocessor, *real*, vertically interpolates 3D input fields using functions of dry pressure. Input data from WPS contain both a total pressure and a moisture field (typically relative humidity). Starting at the top of each column of input pressure data, integrated moisture is subtracted from the pressure field, step-wise, down to the surface. This total dry surface pressure p_s (diagnosed from WPS) defines the vertical coordinate metric

$$\mu_d = \overline{\mu}_d + \mu_d' = B_\eta(\eta)(p_s - p_t) + \big[1 - B_\eta(\eta)\big](p_0 - p_t). \tag{5.8}$$

With the ARW vertical coordinate η, the model lid p_t, and the column dry pressure known at each (i, j, k) location, the 3-dimensional arrays are interpolated.

Vertical calculations are always interpolations in the free atmosphere, up to the model lid; however, near the model surface, it is possible to have an inconsistency between the input surface pressure (which is largely based on the input surface elevation) and the ARW surface pressure (which could have a significantly higher-resolution topography). These inconsistencies may lead to an extrapolation. The default behavior for extrapolating the horizontal winds and the relative humidity below the known surface keeps the values constant, with zero vertical gradient. For potential temperature, a default of 6.5 K/km lapse rate is applied. Vertical interpolation of the geopotential field is optional and is handled separately. Since a known lower boundary condition exists (the geopotential is defined as zero at the pressure at sea-level), no extrapolation is required.

5.2.4 Perturbation State

In the real-data preprocessor, first a topographically defined reference state is computed, then the input 3-dimensional data are vertically interpolated in dry pressure space. With the potential temperature θ and mixing ratio q_v available on each η level, pressure, density, and height diagnostics are handled. The perturbation μ'_d, given the reference value $\overline{\mu}_d$ defined in (5.7) and the vertical coordinate metric μ_d defined in (5.8), is defined as

$$\mu'_d = \mu_d - \overline{\mu}_d, \tag{5.9}$$

Starting with the reference state fields (5.4, 5.6, and 5.7) and the perturbation (5.9), the perturbation fields for pressure and inverse density are diagnosed. The pressure perturbation includes moisture, and is diagnosed from the hydrostatic equation

$$\delta_\eta p' = \mu'_d \left(1 + \overline{q_v}^\eta \right) + \overline{q_v}^\eta \, \overline{\mu}_d,$$

which is integrated down from the model top (where $p' = 0$) to recover p'. The total dry inverse density is given as

$$\alpha_d = \frac{R_d}{p_0} \, \theta_m \left(\frac{p'_d + \overline{p}_d}{p_0} \right)^{-\frac{C_v}{C_p}},$$

which defines the perturbation field for inverse density

$$\alpha'_d = \alpha_d - \overline{\alpha}_d.$$

The perturbation geopotential is diagnosed from the hydrostatic relation

$$\delta_\eta \phi' = -\left(\mu_d \alpha'_d + \mu'_d \overline{\alpha}_d \right)$$

by upward integration, using the terrain elevation as the lower boundary condition.

5.2.5 Generating Lateral Boundary Data

This section deals with generating the separate lateral boundary condition file used exclusively for real-data cases. For information on which lateral boundary options are available for both idealized and real-data cases, see Chapter (6).

For real-data cases, the specified lateral boundary condition for the coarse grid is supplied by an external file that is generated by program *real*. This file contains records for the fields u, v, θ, q_v, ϕ', and μ_d' that are used by ARW to constrain the lateral boundaries (other fields are in the boundary file, but are not used). The lateral boundary file holds one less time period than was processed by WPS. Each of these variables has both a valid value at the initial time of the lateral boundary time, and a tendency term to get to the next boundary time period. For example, assuming a 3-hourly availability of data from WPS, the first time period of the lateral boundary file for u would contain data for both coupled u (map scale factor and μ_d interpolated to the variable's staggering) at the 0 h time

$$U_{0h} = \left. \frac{\overline{\mu_d}^x u}{\overline{m}^x} \right|_{0h},$$

and a tendency value defined as

$$U_t = \frac{U_{3h} - U_{0h}}{3h},$$

which would take a grid point from the initial value to the value at the 3-hour simulation time. The horizontal momentum fields are coupled both with μ_d and the inverse map factor. The other 3-dimensional fields (θ, q_v, and ϕ') are coupled only with μ_d. The μ_d' lateral boundary field is not coupled.

Each lateral boundary field is defined along the four sides of the rectangular grid (loosely referred to as the north, south, east, and west sides). Boundary values and tendencies for vertical velocity and the non-vapor moisture species are included in the external lateral boundary file, but act as place-holders for the nested boundary data for the fine grids. The width of the lateral boundary zone along each of the four sides is user-selectable at run-time (as shown in Fig. 6.1).

5.2.6 Masking of Surface Fields

Some of the meteorological and static fields are masked. A masked field is one in which values are typically defined only over water (e.g., sea surface temperature) or defined only over land (e.g., soil temperature). The need to match all of the masked fields consistently to each other requires additional steps for real-data cases due to the masked data's presumed use in various physics packages in the soil, at the surface, and in the boundary layer. If the land/water mask for a location is flagged as a water point, then vegetation and soil categories must also recognize the location as the special water flag for each of their respective categorical indices. Similarly, if the land/water mask is flagged as a land point, vegetation and soil categories must be assigned to one of the available land indices.

Values for soil temperature and soil moisture come from WPS, and are on the native levels originally defined for those variables by an external model. WPS does not vertically interpolate soil data. While it is typical to attempt to match the ARW soil scheme with the incoming data, that is not a requirement. Pre-processor *real* will vertically interpolate (linear in depth below the ground) from the incoming levels to the requested soil layers to be used within the model.

5.3 Digital Filtering Initialization

ARW provides a digital filtering initialization (DFI) to remove noise from the model initial state. This noise results from imbalances between the interpolated mass and wind fields, and the differences between the coarser topography of the first-guess data set and relatively higher resolution topography of ARW. DFI is applied to output from the *real* preprocessor before the model simulation begins. If data assimilation is performed using WRF-Var, DFI is applied to analysis produced by the WRF-Var system, rather than the output of program *real*.

Under the assumption that any noise is of higher frequency than meteorologically significant modes, DFI attempts to remove this noise by filtering all oscillations above a specified cutoff frequency. Accordingly, filters in the ARW DFI are low-pass digital filters, which are applied to time-series of model fields. The *initialized* model state is the output of the filter at some prescribed time, (e.g., the analysis time). Time series of model states are generated through combinations of integration types that may include adiabatic, backward integration and diabatic, and/or forward integration in the model, along with the chosen DFI scheme (which determines the specific combination of integration). Three DFI schemes are available: digital filter launch (DFL; Lynch and Huang (1994)), diabatic DFI (DDFI; Huang and Lynch (1993)), and twice DFI (TDFI; Lynch and Huang (1994)).

5.3.1 Filter Design

In ARW DFI, either nonrecursive (i.e., finite impulse response) digital filters or a recursive (i.e., infinite impulse response) digital filter may be used. Coefficients for the nonrecursive digital filters may be computed according to one of two methods, while coefficients for the recursive filter are computed according to a single method.

A general nonrecursive digital filter is of the form

$$y_n = \sum_{k=-N}^{N} h_k x_{n-k}, \tag{5.10}$$

where y_n is the output of the filter at time n, the h_k are the coefficients of the filter, and $\{\ldots, x_{n-1}, x_n, x_{n+1}, \ldots\}$ is the sequence of input values to be filtered; such a filter is said to have span $2N + 1$.

One method for deriving the coefficients of a nonrecursive digital filter is the windowed-sinc method, described in the context of DFI by Lynch and Huang (1992). In the ARW DFI, either the Lanczos, Hamming, Blackman, Kaiser, Potter, or Dolph-Chebyshev windows may be used; the Dolph-Chebyshev window is described by Lynch (1997). However, when a filter with a shorter span is desired, another nonrecursive digital filter - the Dolph filter - may be used. Lynch (1997) describes the construction of the Dolph filter, and demonstrates that this filter has properties nearly indistinguishable from those of an optimal filter, which minimizes the maximum difference between a filter's transfer function and an ideal transfer function in the pass and stop bands.

The only recursive filter in ARW DFI is the second-order Quick-Start filter of Lynch and Huang (1994). In general, a recursive digital filter that depends only on past and present values of input, and on past values of output, is of the form

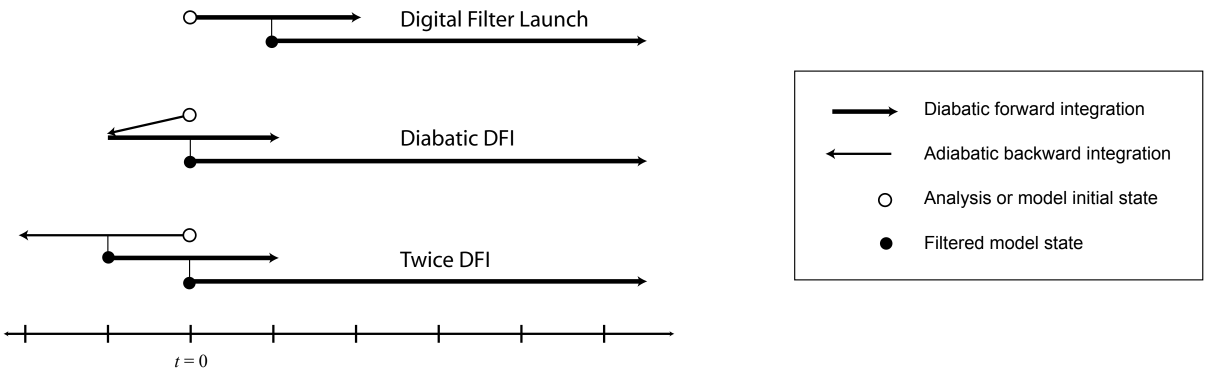

Figure 5.2: An illustration showing the three available DFI schemes: digital filter launch, diabatic digital filter initialization, and twice digital filter initialization.

$$y_n = \sum_{k=0}^{N} h_k x_{n-k} + \sum_{k=1}^{N} b_k y_{n-k}. \tag{5.11}$$

However, this form is inconvenient when inputs to the filter consist of model states, and storing many such states should be avoided. Lynch and Huang (1994) show how this type of recursive filter can be reformulated to the same form as a nonrecursive filter, and thus, the second-order Quick-Start filter follows the same form as (5.10).

5.3.2 DFI Schemes

ARW supports three different DFI schemes, illustrated graphically in Fig. 5.2. The DFL scheme produces an initialized model state valid some time after the model analysis time, while the DDFI and TDFI schemes produce initialized states valid at the analysis time.

DFL

In the DFL scheme, forward integration with full model physics and diffusion begins at the initial time and continues for $2N$ time steps, during which time a filtered model state valid N time steps beyond the analysis time is computed as in (5.10). Then, the initialized simulation is launched from the midpoint of the filtering period. For any model state $\mathbf{X}$, let $[\mathbf{X}]_n^D$ give the model state after diabatically integrating n time steps forward in time; we emphasize that the superscript D indicates diabatic integration, in contrast to adiabatic integration. Then, the DFL scheme is expressed as

$$\mathbf{X}_{ini} = \sum_{n=0}^{2N} h_n \left[\mathbf{X}_{ana}\right]_n^D , \tag{5.12}$$

where $\mathbf{X}_{ini}$ is the initialized model state, $\mathbf{X}_{ana}$ is the model analysis or model initial state generated by the *real* preprocessor, and h_n represents filter coefficients.

DDFI

To produce an initialized state valid at the model analysis time, the DDFI scheme begins with an adiabatic, backward integration for N time steps, followed by a diabatic, forward integration for $2N$ time steps, during which filtering takes place. This filtered state is valid at the model analysis time. Letting $[\mathbf{X}_{ana}]^A_{-n}$ denote the model state after adiabatic, backward integration for n time steps from the model analysis or model initial state, $\mathbf{X}_{ana}$, the DDFI scheme is expressed as

$$\mathbf{X}_{ini} = \sum_{n=0}^{2N} h_n \left[[\mathbf{X}_{ana}]^A_{-n} \right]^D_n , \tag{5.13}$$

where $\mathbf{X}_{ini}$ is the initialized model state valid at the model analysis time.

TDFI

The TDFI scheme involves two applications of the digital filter. Adiabatic, backward integration proceeds from the model initial time for $2N$ time steps, during which a filter is applied. The filtered state is valid at time $-N\Delta t$. From this filtered state, a forward, diabatic integration is launched. The second integration proceeds for $2N$ time steps, during which a second filter is applied, giving a filtered model state valid at this model analysis time. The TDFI scheme is expressed as

$$\mathbf{X}_{ini} = \sum_{n=0}^{2N} h_n \left[\sum_{n'=0}^{2N} h_{n'} \, [\mathbf{X}_{ana}]^A_{-n} \right]^D_n . \tag{5.14}$$

5.3.3 Backward Integration

To diabatically integrate backward in time, it suffices to disable all diabatic processes and to negate the model time step Δt as well as the sign of the horizontal velocity U in the odd-order advection operators of Section 3.2.3, which become

$$\begin{aligned}
3^{rd} \text{ order:} \quad (\overline{q}^{x_{adv}})_{i-1/2} &= (\overline{q}^{x_{adv}})^{4^{th}}_{i-1/2} \\
&\quad - \operatorname{sign}(U)\frac{1}{12}\big[(q_{i+1} - q_{i-2}) - 3(q_i - q_{i-1})\big] \\
5^{th} \text{ order:} \quad (\overline{q}^{x_{adv}})_{i-1/2} &= (\overline{q}^{x_{adv}})^{6^{th}}_{i-1/2} \\
&\quad + \operatorname{sign}(U)\frac{1}{60}\big[(q_{i+2} - q_{i-3}) - 5(q_{i+1} - q_{i-2}) + 10(q_i - q_{i-1})\big].
\end{aligned}$$

When specified boundary conditions are used, as in Section 6.4, the model boundaries before the model initial time are taken to be the same as those valid at the model initial time. We note that, with a negated time step, the linear ramping functions F_1 and F_2 of (6.1) change sign, and, consequently, so does the sign of the tendency for a prognostic variable ψ.

Chapter 6

Lateral Boundary Conditions

ARW provides several lateral boundary conditions suitable for idealized flow, in addition to a specified lateral boundary condition for real-data simulations. These choices are handled via a run-time option in the Fortran namelist file. For nesting, all fine domains use the nest time-dependent lateral boundary condition where the outer row and column of the fine grid are specified from the parent domain, described in Section 7.3. The remaining lateral boundary options are exclusively for use by the outer-most parent domain.

6.1 Periodic Lateral Boundary Conditions

Periodic lateral boundary conditions in ARW can be specified as periodic in x (west-east), y (south-north), or doubly periodic in (x, y). The periodic boundary conditions constrain the solutions to be periodic; that is, a generic model state variable ψ will follow the relation

$$\psi(x + nL_x, y + mL_y) = \psi(x, y)$$

for each integer (n, m). The periodicity lengths (L_x, L_y) are
[(dimension of the domain in x) - 1]Δx and [(dimension of the domain in y) - 1]Δy.

6.2 Open Lateral Boundary Conditions

Open lateral boundary conditions, also referred to as gravity-wave radiating boundary conditions, can be specified for the west, east, north, or south boundary, or any combination thereof. The gravity wave radiation conditions follow the approach of Klemp and Lilly (1978) and Klemp and Wilhelmson (1978).

There are a number of changes in the base numerical algorithm described in Chapter 3 that accompany the imposition of these conditions. First, for the normal horizontal velocities along a boundary on which the condition is specified, the momentum equation for the horizontal velocity, (3.7) or (3.8), is replaced by

$$\delta_\tau U'' = -U^* \delta_x u,$$

where $U^* = \min(U - c_b, 0)$ at the $x = 0$ (western) boundary, $U^* = \max(U + c_b, 0)$ at the $x = L$ (eastern) boundary, and likewise for the south and north boundaries for the V momentum. The horizontal difference operator δ_x is evaluated in a one-sided manner using the difference between the boundary value and the value one grid-point into the grid, from the boundary. c_b is the phase speed of the gravity waves that are to be radiated; it is specified as a model constant (for more details see Klemp and Lilly, 1978; Klemp and Wilhelmson, 1978).

For scalars and non-normal momentum variables, the boundary-perpendicular flux divergence term is replaced with

$$\delta_x(U\psi) = U^*\delta_x\psi + \psi\ \delta_x U,$$

where $U^* = \min(U, 0)$ at the $x = 0 + \Delta x/2$ (western) scalar boundary, $U^* = \max(U, 0)$ at the $x = L - \Delta x/2$ (eastern) boundary, and likewise for the south and north boundaries, using V. As was the case for the momentum equations, the horizontal difference operator δ_x is evaluated in a one-sided manner using the difference between the boundary value and the value one grid-point into the grid from the boundary.

6.3 Symmetric Lateral Boundary Conditions

Symmetry lateral boundary conditions can be specified for the west, east, north, or south boundary, or any combination thereof. The symmetry boundaries are located on the normal-velocity planes at the lateral edges of the grids. The normal velocities are zero at these boundaries, and on either side of the boundary the normal velocity satisfies the relation

$$U_\perp(x_b - x) = -U_\perp(x_b + x),$$

where x_b is the location of the symmetry boundary. All other variables satisfy the relation

$$\psi(x_b - x) = \psi(x_b + x).$$

6.4 Specified Lateral Boundary Conditions

Primarily for real-data cases, the specified boundary condition is also referred to as a relaxation, or nudging, boundary condition. There are two uses of specified boundaries in ARW: for the outer-most coarse grid or for the time-dependent boundaries supplied to a nested grid. The specified lateral boundary conditions for the nest are automatically selected for all of the fine grids, even if the coarse grid is using combinations of the symmetry, periodic, or open options. If the specified lateral boundary condition is selected for the coarse grid, then all four grid sides (west, east, north, and south) use specified lateral conditions. However, in tropical channel mode, where the domain wraps completely around the equator, it is possible to combine specified boundary conditions with periodic conditions in the x-direction. Note that care is needed in setting up the domain so that the points exactly match the longitude at the east and west boundaries when periodic conditions are used in real-data cases. Also, note that a Mercator projection is needed to make this possible.

The coarse grid specified lateral boundary is comprised of both a specified and a relaxation zone (as shown in Fig. 6.1). For the coarse grid, the specified zone is determined entirely by temporal interpolation from an external forecast or analysis (supplied by WPS). The width of the specified zone is run-time configurable, but is typically set to 1 (i.e., the last row and column

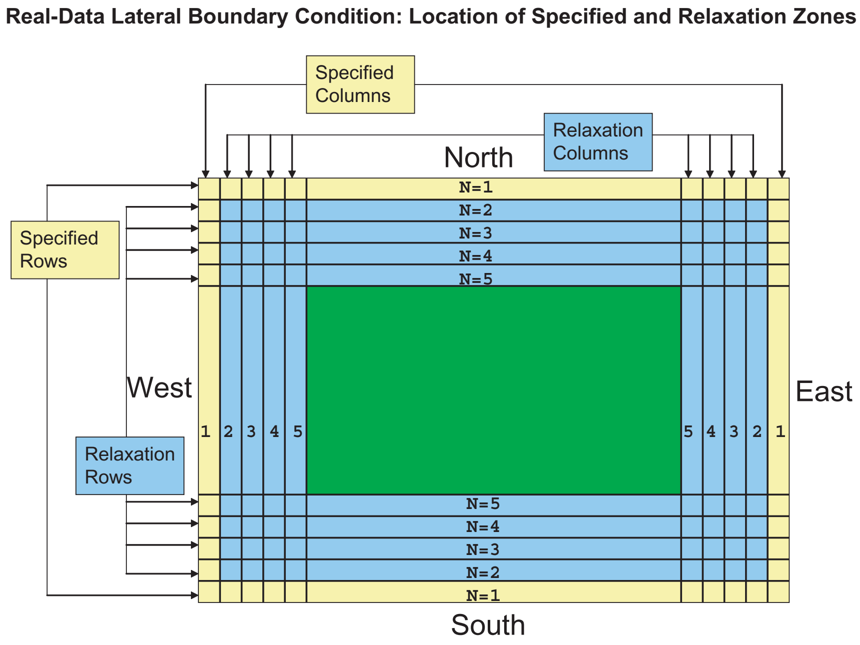

Figure 6.1: Specified and relaxation zones for a grid with a single-specified row and column, plus four rows and columns for the relaxation zone. These are typical values used for a specified lateral boundary condition for a real-data case. In this figure, the weight of the relaxation term would be identically zero for the fifth row or column in from the boundary edge.

along the outer edge of the outer-most grid is entirely specified by temporal interpolation, using data from an external model). The second region of the lateral boundary for the coarse grid is the relaxation zone, which is where the model is nudged or relaxed towards the large-scale forecast (e.g., rows and columns 2 through 5 in Fig. 6.1). The size of the relaxation zone is a run-time option.

The specified lateral boundary condition for the coarse grid requires an external file, generated during the same pre-processing as the initial condition file. Let ψ be any prognostic value having a lateral boundary entry, after Davies and Turner (1977),

$$\partial_t \psi \big|_n = F_1(\psi_{LS} - \psi) - F_2 \Delta^2 (\psi_{LS} - \psi), \tag{6.1}$$

where n is the number of grid points in from the outer row or column along the boundary ($SpecZone + 1 \leq n \leq SpecZone + RelaxZone - 1$; see Fig. 6.1) and ψ_{LS} is the large-scale value obtained by spatial and temporal interpolation from the external analysis or model forecast by WPS . Δ^2 is a 5-point horizontal smoother applied along η-surfaces. The weighting function coefficients F_1 and F_2 in (6.1) are given by

$$F_1 = \frac{1}{10\Delta t} \frac{SpecZone + RelaxZone - n}{RelaxZone - 1},$$

$$F_2 = \frac{1}{50\Delta t} \frac{SpecZone + RelaxZone - n}{RelaxZone - 1},$$

where n extends only through the relaxation zone ($SpecZone{+}1 \leq n \leq SpecZone{+}RelaxZone{-}1$). F_1 and F_2 are linear ramping functions with a maximum at the first relaxation row or column nearest to the coarse-grid boundary (just inside the specified zone). These linear functions can optionally be multiplied by an exponential function for smoother behavior when broad boundary zones are needed. This is achieved through an extra factor.

$$F_1 = \frac{1}{10\Delta t} \frac{SpecZone + RelaxZone - n}{RelaxZone - 1} \exp[-SpecExp(n - SpecZone - 1)]$$

$$F_2 = \frac{1}{50\Delta t} \frac{SpecZone + RelaxZone - n}{RelaxZone - 1} \exp[-SpecExp(n - SpecZone - 1)]$$

where $SpecExp$ is an inverse length scale in grid lengths.

On the coarse grid, the specified boundary condition applies to the horizontal wind components, potential temperature, ϕ', μ'_d, and water vapor. The lateral boundary file contains enough information to update boundary zone values through the entire simulation period. The momentum fields are coupled with μ_d and the inverse map factor (both at the specific variable's horizontal staggering location), and the other 3-dimensional fields are coupled with μ_d. The μ'_d field is not coupled in the lateral boundary file.

Several fields within the model have specified lateral boundary conditions that are associated particularly with a known variable. Vertical velocity has a zero gradient boundary condition applied in the specified zone (the outer-most row and column). Users are able to control the behavior of the treatment of the lateral boundary conditions for scalar variables that are subject to transport. By default, microphysical variables (except vapor) and all other scalars (such as chemistry constituents, passive tracers, scheme-specific aerosols, and number concentration fields) have flow-dependent boundary conditions applied in the specified zone. This boundary condition is defined as zero-value on inflow and zero-gradient on outflow. Since these boundary conditions require only information from the interior of the grid, these scalar variables are not required to be in the lateral boundary condition file. If sufficient scalar data is provided to the lateral boundary condition file, the same technique of relaxation towards temporally-interpolated variables is employed, identically as with the dynamic variables.

6.5 Polar Conditions

See subsection 3.2.4 for details on how the polar boundary condition is applied.

Chapter 7

Nesting

ARW provides the capability to focus the area of a simulation via nesting options. ARW supports horizontal nesting that allows resolution to be enhanced over a region of interest by introducing an additional grid (or grids) into the simulation. This subdomain with increased horizontal resolution is completely contained within the parent domain (this is also commonly referred to as the coarse domain and abbreviated CG). The subdomain is commonly referred to as the child domain or the fine grid (FG). Vertical refinement options are available, where a child domain may have a different vertical structure than the parent domain. Parent and child domains always extend from the lower model surface, through to the upper model lid. In this way, the vertical capability is more accurately referred to as a refinement, as opposed to nesting. In practice, both of these terms will be used interchangeably when referring to a child domain that has enhanced vertical resolution, compared to the parent domain.

As with all domains within ARW, the horizontally or vertically nested grids (child domains, fine-grid domains) are rectangular and are aligned with the parent (coarser) grid within which they are nested. The horizontal nested grids allow any integer spatial ($\Delta x_{coarse}/\Delta x_{fine}$) and temporal refinements of the parent grid (the spatial and temporal refinements are usually, but not necessarily the same). The vertical refinement capability offers two options: either an integer factor of the number of levels in the parent to define the child domain's vertical structure (for example, a doubling or tripling of the vertical resolution), or a completely independent set of vertical levels prescribed for the parent and the child domain. The horizontal nesting capability is, in many ways, similar to implementations provided in other mesoscale and cloud-scale models (e.g. MM5, ARPS, COAMPS). Vertical refinement options are described in Mahalov and Moustaoui (2009) and Daniels et al. (2016).

In this chapter we describe the various horizontal and vertical nesting options available in ARW and the exchange of data between the grids.

7.1 Horizontal Nesting Options

1-Way and 2-Way Grid Nesting

Nested grid simulations can be produced using either 1-way nesting or 2-way nesting as outlined in Fig. 7.1. The 1-way and 2-way nesting options refer to the way in which a coarse grid and fine grid interact. In both 1-way and 2-way simulation modes, the fine-grid boundary conditions (i.e., the lateral boundaries) are interpolated from the coarse-grid forecast domain. In a 1-way

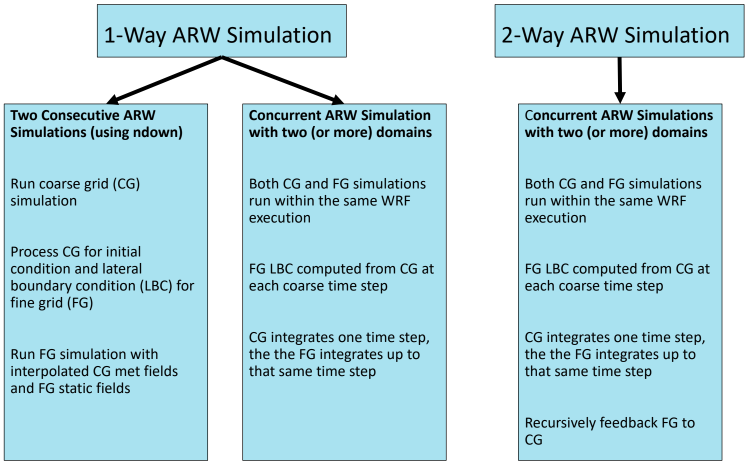

Figure 7.1: 1-way (parent provides boundary data to child) and 2-way (parent provides boundary data to child, then child feeds information back to the parent) nesting options in ARW.

nest, the only information exchange is from the coarse grid to the fine grid; hence, the name *1-way nesting*. In 2-way nest integration, the fine-grid solution replaces the coarse-grid solution for coarse grid points that lie inside the fine grid. This information exchange between the grids is now in both directions (coarse-to-fine for the fine-grid lateral boundary computation, and fine-to-coarse during the feedback at each coarse-grid time step); hence, the name *2-way nesting*.

The 1-way nest set-up may be run in one of two different methods. One option is to produce the nested simulation as two separate ARW simulations, as described in the leftmost box in Fig. 7.1. In this mode, the coarse grid is integrated first and once the coarse-grid time step is completed, output from the coarse-grid integration is processed to provide boundary conditions for the nested run (usually at a much lower temporal frequency than the coarse-grid time step). This is followed by the complete time integration of the fine (nested) grid. Hence, this 1-way option is equivalent to running two separate simulations with a processing step in between. Also, with separate grid simulations, an intermediate re-analysis (such as via WRFDA, see Section 11) may be included.

The second 1-way option (lockstep, with no feedback), depicted in the middle box in Fig. 7.1, is run as a traditional simulation with two (or more) grids integrating concurrently, except with the feedback runtime option turned off. This option provides lateral boundary conditions to the fine grid at each coarse-grid time step, which is an advantage of the concurrent 1-way method (no feedback).

Fine Grid Initialization Options

ARW supports several strategies to horizontally refine a coarse-grid simulation with the introduction of a nested grid. When using concurrent 1-way and 2-way nesting, several options for initializing the fine grid are provided.

- All fine-grid variables (both meteorological and terrestrial) are interpolated from the coarse grid, which is useful when a fine grid starts later in the coarse-grid forecast.
- All fine-grid variables are input from an external file that has high-resolution information for both the meteorological and terrestrial fields. This is a standard set-up when the fine-grid terrestrial fields are expected to impact the forecast.
- The fine grid may have some of the variables initialized with a high-resolution external data set, while other variables are interpolated from the coarse grid (for example, this would permit the improved analysis from the WRFDA initialization of the coarse grid's meteorological fields to remain consistent with the fine grid). This option allows the fine grid to start later in the coarse grid's forecast, but with the advantage of higher-resolution static fields.
- For a moving nest, external orography and landuse files may be used to update the fine-grid domain as it moves over land.

These fine-grid initialization settings are user-specified at run-time, and ARW allows nested grids to instantiate and cease during any time that the fine grid's parent is still integrating. While cost savings are evident when starting the fine-grid domain at a later time, that advantage must be weighed against the impact of relatively coarse and inconsistent fields for both masked and meteorological variables on the fine grid.

Possible Grid Configurations

A simulation involves one outer grid and may contain multiple inner nested grids. In ARW, each nested region is entirely contained within a single coarser grid, referred to as the *parent* grid. The finer nested grids are referred to as *child* grids. Using this terminology, child domains may also be parent domains when multiple levels of nesting are used. The fine grids may be telescoped to any depth (i.e., a parent grid may contain one or more child grids, each of which in turn may successively contain one or more child grids; Fig. 7.2a), and several fine grids may share the same parent at the same level of nesting (Fig. 7.2b). Currently, the software limit for subdomains is ten levels of nesting, but the practical limit is much smaller. Any valid fine grid may either be a static domain or a moving nest (with either prescribed incremental shifts or with automatic moves via a vortex-following algorithm, such as tracking the minimum of the 500 hPa height). ARW does not permit overlapping grids, where a coarse grid point is contained within more than a single child grid (i.e., both of which are at the same nest level with respect to the parent; Fig. 7.2c). In addition, no grid can have more than a single parent (Fig. 7.2d). For global domains, a fine grid domain cannot cross the periodic lateral boundary of the parent domain (for example, a global domain may not have a nested tropical channel at the equator that uses periodic east-west boundaries in the nest.)

For both 1-way and 2-way nested grid simulations, the ratio of the parent horizontal grid distance to the child horizontal grid distance (the spatial refinement ratio) must be an integer. For 2-way and concurrent 1-way nesting, this is also true for the time steps (the temporal

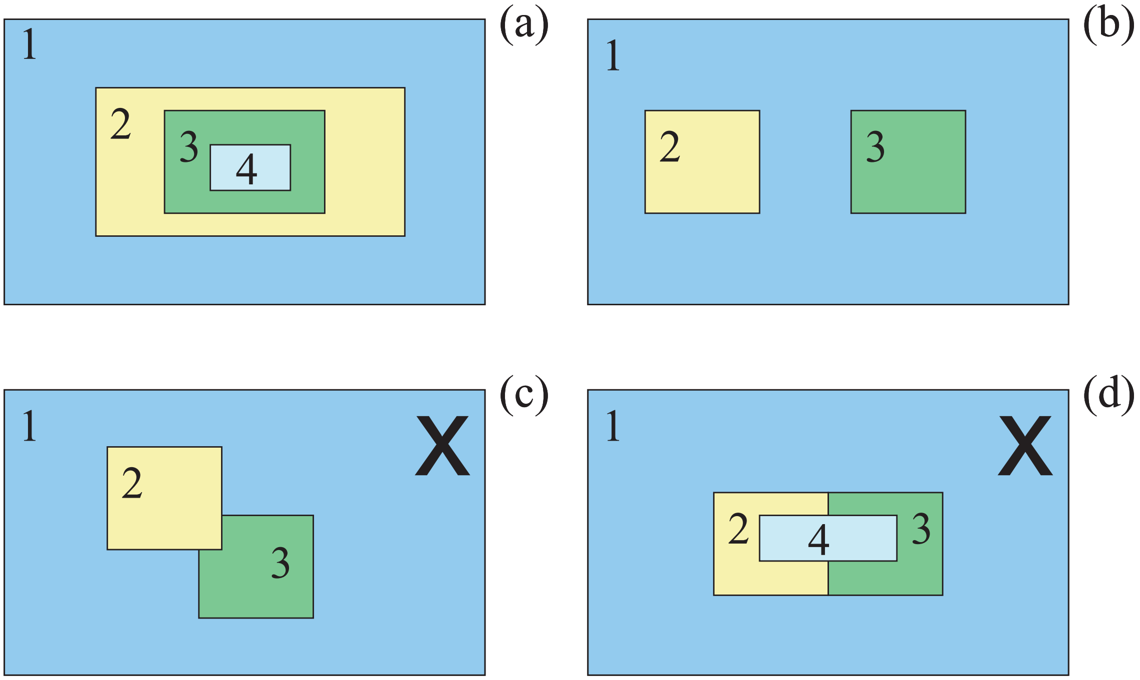

Figure 7.2: Various nest configurations for multiple grids. (a) Telescoping nests. (b) Nests at the same level with respect to a parent grid. (c) Overlapping grids: not allowed with feedback activated. (d) Inner-most grid has more than one parent grid: not allowed

refinement ratio), though the model does allow the time step refinement ratio to differ from the spatial refinement ratio. Also, nested grids on the same level (i.e., children who have the same parent) may have different spatial and temporal refinement ratios. For example, in Fig. 7.2b, the horizontal grid resolution for domain 1 may be 90 km, while domain 2 may be 45 km, and domain 3 may be 30 km.

Moving Nests

The moving nest capabilities in ARW are simply extensions to the suite of nesting options. All descriptions covering the specifics for fine-grid domains (initialization, feedback, configurations, staggering, lateral boundaries, etc.) also apply to moving nests. In general, all nests in an ARW forecast are eligible to be moving nests. ARW provides two methods to allow nests to move during model integration: specified and automatic. For both types of moving nests, multiple levels of domains may move.

For a specified move, the timing of a nest move and the extent of each lateral move is defined entirely by the user through the namelist. This manual process is tedious and cumbersome, and is rarely used in practice. This capability was required to eventually develop a fully functioning moving nest capability that automatically tracks a cyclone.

For the automatically moving nest, the fine grid is initialized to cover a well-defined vortex, and the nest moves to maintain this vortex in the center of the fine grid. The fine grid follows a height minimum, and is constrained so as to not too closely approach the parent boundary. This option provides a substantial cost savings when the area of horizontal refinement is reduced in size to cover only the physical extent of a cyclone, and not the much larger domain necessary to contain a moving system. The typical instance for utilizing a moving nest is during tropical cyclone tracking via the automatic vortex-following technique. With this automated cyclone tracking, the inner-most domain is responsible for steering the movement of the coarser, moving grids.

After a nested domain has moved a parent grid-cell distance, the majority of the fine-grid data in the domain is still valid. Data that are not along the outer row or column of the nested domain is shifted to the new location in that domain; not interpolated from the parent domain. Once a domain moves, data in the outer row or column fall into one of two categories: discarded data on the trailing edge, or horizontally interpolated data on the leading edge in the direction of the nest move. Only elevation of the topography and landuse categories are eligible to be used as input from high-resolution files, instead of being interpolated from the parent domain.

7.2 Staggering and Feedback

ARW uses an Arakawa-C grid staggering. As shown in Fig. 7.3, the u and v components of horizontal velocity are normal to the respective faces of the grid cell, and the mass/thermodynamic/scalar/chemi variables are located in the center of the cell.

The variable staggering has an additional column of u in the x-direction and an additional row of v in the y-direction because the normal velocity points define the grid boundaries. The horizontal momentum components reflect an average across each cell-face, while each mass/thermodynamic/scalar/chemistry variable is the representative mean value throughout the cell. Feedback is handled to preserve these mean values: the mass/thermodynamic/scalar/chemistry fields are fed back with an average from within the entire coarse grid point (Fig. 7.3), and the horizontal momentum variables are averaged along their respective normal coarse grid cell faces. Horizontal interpolation from the coarse grid at each time step produces the lateral boundary conditions for the fine-grid domain, and horizontal interpolation may entirely instantiate several fields on the fine-grid domain. Not all horizontal interpolation techniques used within the model necesssarily conserve mass.

The horizontal interpolation (to instantiate a grid and to provide time-dependent lateral boundaries) does not conserve mass. The feedback mechanism, for most of the unmasked fields, uses cell averages (for mass/thermodynamic/scalar/chemistry quantities) and cell-face averages for the horizontal momentum fields.

Staggering defines the way that the fine grid is situated on top of the coarse grid. For all odd grid-distance ratios (for example, a 3:1 ratio could have a parent with a 90 km grid distance and a child with a 30 km grid distance) there is a coincident point for each variable: a location that has the coarse grid and the fine grid at the same physical point. The location of this point depends on the variable, whether the variable is located at the cell center (mass variable) or along the cell face (momentum variable). In each of the coarse-grid cells with an odd ratio, the middle fine-grid cell is the coincident point with the coarse grid point for all of the mass-staggered fields (Fig. 7.3). For horizontal momentum variables, the normal velocity has coincident points along the grid boundaries for odd ratios.

Using the 3:1 grid-distance ratio from the example shown in Fig. 7.3, during feedback, the mean of the nine mass/thermodynamic/scalar/chemistry fine-grid points is fed back to

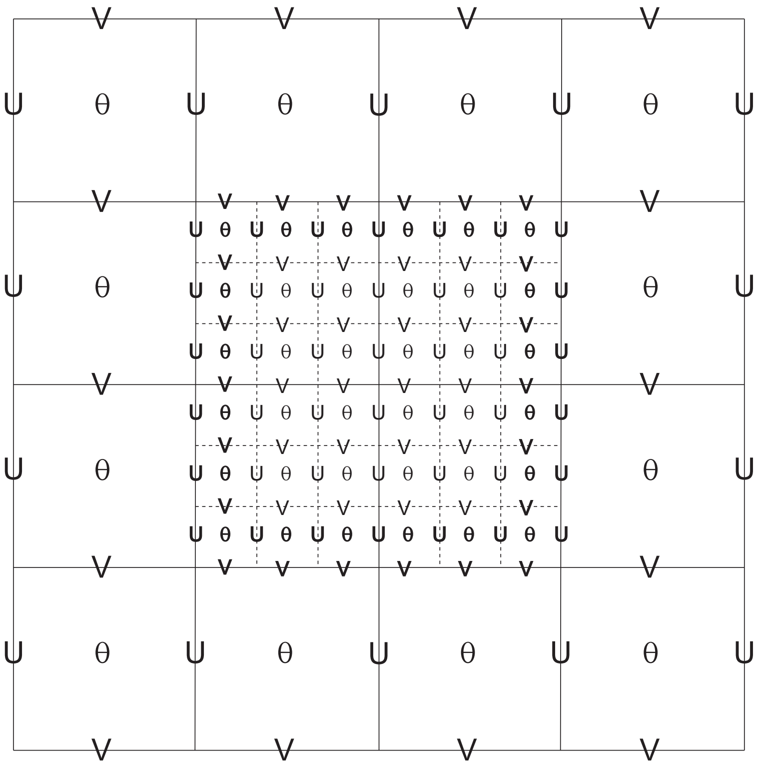

Figure 7.3: Arakawa-C grid staggering for a portion of a parent domain, with an imbedded nest domain using a 3:1 grid size ratio. Solid lines denote coarse grid cell boundaries, and dashed lines are the boundaries for each fine grid cell. The horizontal components of velocity (“U” and “V”) are defined along the normal cell face, and the thermodynamic variables (“θ”) are defined at the center of the grid cell (each square). The bold typeface variables along the interface, between the coarse and the fine grid, define the locations where the specified lateral boundaries for the nest are in effect.

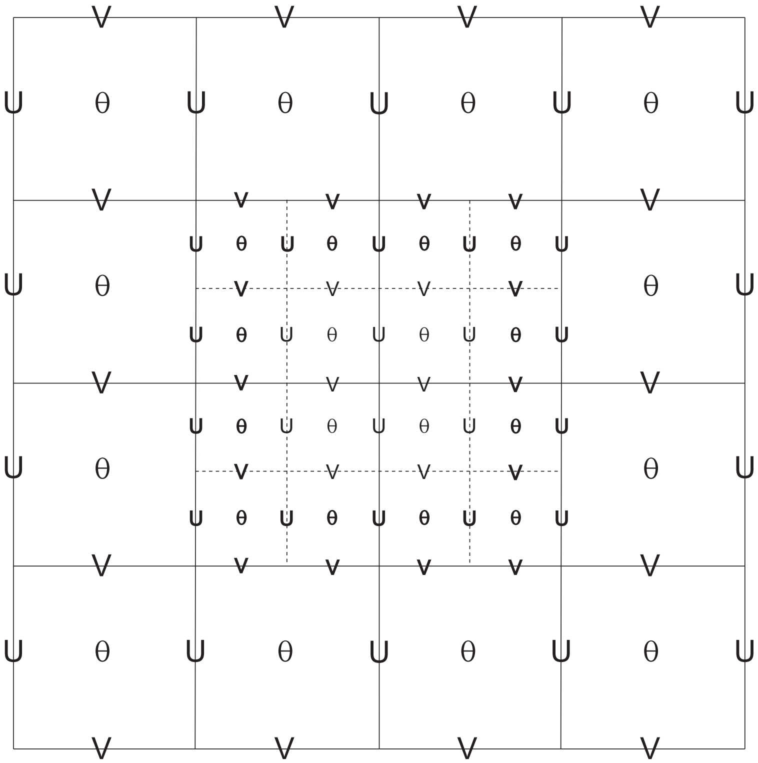

Figure 7.4: Similar to Fig. 7.3, but with a 2:1 grid-distance ratio.

the coarse grid. These fields include most 3-dimensional and 2-dimensional arrays. For the horizontal momentum fields averaged back to the coarse grid in the feedback, the mean of three (for example, due to the 3:1 grid-distance ratio in the example shown in Fig. 7.3) fine grid points is fed back to the coarse grid from along the coincident cell face. When using odd ratios, fields that are masked due to the land/sea category are fed back directly from the coincident points. Masked fields include soil temperature and sea ice. It is not reasonable to average neighboring locations of soil temperature on the fine grid if the coarse grid point to which values are being fed back is a water value. Similarly, averaging several sea ice values on the fine grid does not make sense if some of the neighboring points included in the mean are fine grid land points. Only masked fields use the feedback method in which a single point (such as for land use category) or a mean of valid points (such as for soil temperature) from the fine grid is assigned to the coarse grid.

One difference between odd and even grid-distance ratios is in the feedback from the fine grid to the coarse grid. No coincident points exist for the single point feedback mechanisms for even grid distance ratios (such as is used for the land/sea masked 2D fields). For a 2:1 even grid distance ratio, Figure 7.4 shows that each coarse grid point has four fine grid cells that are equally close, and therefore four equally-eligible grid points for use as the single fine-grid point that feeds back to the coarse grid. The single-point feedback is arbitrarily chosen as the south-west corner of the four neighboring points. This arbitrary assignment to masked fields implies that even grid distance ratios are better suited for idealized simulations where masked fields are less important.

7.3 Nested Lateral Boundary Conditions

For the fine grid with 2-way nesting or 1-way nesting (using a concurrent ARW simulation, see Fig. 7.1), boundary conditions are specified by the parent grid at every coarse-grid time step. The nest lateral boundary condition behaves similarly to the specified boundary condition for real-data cases (see Section 6.4), but the relaxation zone is not active. Prognostic variables are entirely specified in the outer row and column of the fine grid through spatial and temporal interpolation from the coarse grid (the coarse grid is stepped forward in time, prior to advancement of any child grid of that parent).

7.4 Steps to Generate a Nest Grid

Only the concurrent 1-way nest option or the 2-way nest option is considered in this section. The 1-way nest option (using two consecutive ARW simulations, see Fig. 7.1) is functionally similar to two separate, single-grid simulations and does not fit the description in this section. For a multiple-grid simulation within a single model run, there are some additional infrastructure steps that are required (briefly described in Fig. 7.5). While the following text details a simulation with a single coarse grid and a single fine grid, this implies no lack of generality when handling multiple grid levels or multiple grids on the same level.

Nest Instantiation

The fine grid is instantiated as a child of a parent grid at the requested start time. This initialization is within the integration step for the parent grid, meaning that no child grid integration can begin if the parent is not active. To fill in the correct meteorological fields, a default initialization routine is called to horizontally interpolate coarse-grid data to the fine-grid locations using a monotone interpolation scheme (described in Smolarkiewicz and Grell, 1992) for most fields (i.e., the same scheme employed for generating the fine grid lateral boundary conditions) and a simple linear interpolation, or averaging scheme, for masked or categorical fields. For fields that are masked with the land/sea background, such as land-only fields (e.g., snow), or water-only fields (e.g., sea ice), the interpolator needs to know what field defines the template for masking (such as for the land use category). Part of the automatic code generation handles calling each field with its associated interpolator.

Fine Grid Input

After horizontal interpolation is completed, a few orographic-based variables are saved so that they may be used to blend the lateral boundaries along the coarse-grid/fine-grid interface. The terrain elevation $\overline{\mu}_d$ and reference geopotential $\overline{\phi}$ are stored for later use. The fields selected as input from the fine grid input file (for concurrent 1-way and 2-way forecast methods shown in Fig. 7.1) are ingested, and they overwrite the arrays that were horizontally interpolated from the coarse grid. No quality control for data consistency is performed for the fine grid input. All such masked checks are completed by the ARW real-data pre-processor *real*.

```
Integrate parent grid one time step
    If nest grid start time
        (1) Horizontally interpolate parent to child grid
        (2) Optionally input high-resolution child data
        (3) Compute child reference state
        (4) Feedback Child Initial Data to Parent Grid
        (5) Recompute parent reference state
    End If nest grid start time
    Solve time step for parent grid (see Fig. 3.1)
    If nest grid move time and FG away from CG boundary
        (1) Move nest grid (vortex following or prescribed)
        (2) Horizontally translate data due to grid shift
        (3) Horizontally interpolate parent to child grid (along new boundary)
        (4) Optionally input high-resolution child topo-landuse data
        (5) Compute child reference state
        (6) Feedback child initial data to parent grid
        (7) Recompute parent reference state
    End If nest grid move time
    While existing nest grids to integrate
        (1) Lateral forcing from parent grid to child
        (2) Integrate child grid to current time of parent grid
        (3) Feedback child grid information to parent grid
    End While existing nest grids to integrate
End Grid Integrate
```

Figure 7.5: Nest grid integration sequence.

Interface Blended Orography

To reduce lateral boundary noise entering the fine grid, the fine-grid topography has two zones of smoothing, as seen in Fig. 7.1. The first zone is along the outer edge of the fine domain and extends into the nest, with a defined width identical to the number of coarse grid points in the width of the lateral boundary file. In this first zone, the topography is horizontally interpolated from the coarse grid. The second zone extends inward from the first zone, with a user-defined width. Topography is linearly weighted between the interpolated coarse-grid topography and the fine-grid topography, and it ramps from 100% coarse-grid topography (at the interface between the first and second zones) to 100% fine-grid topography interior to the second zone. Assuming a width of 5 fine-grid cells, the weighting scheme in the second zone is given as:

- row/column 1: 100% interpolated coarse grid, 0% fine grid,
- row/column 2: 75% interpolated coarse grid, 25% fine grid,
- row/column 3: 50% interpolated coarse grid, 50% fine grid,
- row/column 4: 25% interpolated coarse grid, 75% fine grid, and

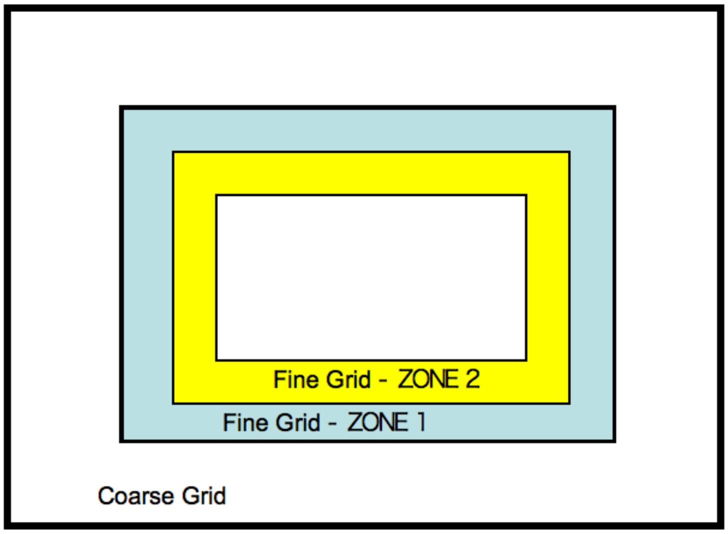

Figure 7.6: Zones of topographic blending for a fine grid. In the fine grid, the first zone is entirely interpolated from the coarse-grid topography. In the second zone, the topography is linearly weighted between the coarse grid and the fine grid.

- row/column 5: 0% interpolated coarse grid, 100% fine grid,

where row=1 is the first row in the second zone, and the row or column nearest the outer edge takes precedence in ambiguous corner zones. The reference variables computed from the topography, $\overline{\mu}_d$ and $\overline{\phi}$, are similarly-treated. Blended arrays are required to compute the reference state for the fine grid. The blending along the inner rows and columns ramps the coarse-grid reference state to the fine-grid reference state for a smooth transition between grids.

Feedback

So that the coarse grid and fine grid are consistent at coincident points, the fine grid values are fed back to the coarse grid. There are two available options for feedback: either the mean of all fine-grid cells contained within each coarse-grid cell (or cell faces in the case of the horizontal momentum fields) is fed back, or a single-point feedback is selected for masked or categorical fields.

Subsequent to the feedback step, the coarse grid may be optionally smoothed in the area of the fine grid. Two smoothers are available: a 5-point 1-2-1 smoother, and a smoother-desmoother with a similar stencil size. Both the feedback and the smoothers are run one row and column in from the interface row and column of the coarse grid (the coarse grid provides the lateral boundary conditions to the fine grid, so the outer-most row cannot be modified).

Reference State

When the nest is instantiated, the initial feedback ensures that the coarse grid is consistent with the fine grid, particularly with regards to topography and the reference state fields inside the blended region, and for such terrestrial features as coasts, lakes, and islands. The adjustment of elevation in the coarse grid forces a base state recalculation. The fine grid needs an initial base state calculation, and after the terrain feedback, the coarse grid is also in need of a base state recalculation. Note that with horizontal interpolation of the coarse grid to the fine grid, and feedback of the fine grid to the coarse grid, the coarse-grid base state is recomputed even without a separate fine-grid initial data file, since the coarse-grid topography is adjusted.

With completed base state computations, which follow similarly to that described for the real-data initialization in section 5.2.2, routines return back to the integration step for the coarse and fine grids. The fine-grid data are now properly initialized for integration and can be advanced forward one time step.

Integration

The integration by grid is recursive. At the end of each grid's time step, a check is made to determine if a child grid exists for that parent and if the current time is bracketed by the child's start/end time. This is shown in Fig. 7.5. The integration process for the nest (step 2 under the while loop) recursively calls the top step in the overall sequence as a parent grid itself. This is a "depth first" traversal of the tree of grids. If a child grid does exist, that child grid is integrated up through the current time of the parent grid.

Interpolation Options

Fields from the parent domain (coarse grid, CG) are interpolated to the child domain (fine grid, FG) prior to the CG data being used by the FG. There are several occurrences of this interpolation.

- At initialization, or upon a domain move, horizontally interpolate all non-masked fields from CG to FG.
- At initialization or upon a domain move, topography (and fields derived from topography) within the FG domain are blended with data from the CG, as shown in Fig. 7.6.
- At the completion of each CG timestep, CG fields are interpolated for use by the FG. This is primarily for the construction of lateral boundary conditions for the FG domain; however, optional interpolations are available for the fields that are only computed on the coarsest grid (examples include stochastic forcing and simple ocean models that are only defined on the outer-most domain).

ARW supports a number of horizontal interpolation options, available via the user-defined namelist.

Chapter 8

Physics

This chapter outlines the physics options available in the ARW. The WRF physics options fall into several categories, each containing several choices. The physics categories are (1) microphysics, (2) cumulus parameterization, (3) planetary boundary layer (PBL), (4) land-surface model, and (5) radiation. Diffusion, which may also be considered part of the physics, is described in Chapter 4.

The physics section is separated from the dynamics in the solver by the use of physics drivers. These drivers are between dynamical-core-dependent parts of the solver: a pre-physics preparation of variables and post-physics modifications of the tendencies. The physics preparation involves filling arrays with physics-required variables that include the temperature, pressure, heights, layer thicknesses, and other state variables in MKS units at half-level grid points and on full levels. The velocities are also de-staggered so that the physics part is independent of the dynamical solver's velocity staggering. Physics packages compute tendencies for the velocity components (un-staggered), potential temperature, and moisture fields. A post-physics step will re-stagger these tendencies as necessary, couple tendencies with coordinate metrics, and convert to variables or units appropriate to the dynamics solver.

In the first Runge-Kutta step, prior to the acoustic steps (see Fig. 3.1, step(1)), tendencies are computed for radiation, surface, PBL, and cumulus physics. These tendencies are then held fixed through the Runge-Kutta steps. Microphysics is computed after the last Runge-Kutta step (see Fig. 3.1, step (9)) in order to ensure proper saturation conditions at the end of the time-step.

The initialization of the physics is called prior to the first model step. This initialization may include reading in data files for physics tables or calculating look-up tables of functions. Each physics module includes an initialization routine for this purpose. Often physics packages will have many of their own constants that are included in their own module, while common physical constants are passed in from the physics drivers.

8.1 Microphysics

Microphysics includes explicitly resolved water vapor, cloud, and precipitation processes. The model is general enough to accommodate any number of mass mixing-ratio variables, and other quantities such as number of particles per unit dry air mass. Four-dimensional arrays with three spatial indices and one species index are used to carry such scalars. Memory, i.e., the size of the fourth dimension in these arrays, is allocated depending on the needs of the scheme chosen, and advection of the species also applies to all those required by the microphysics option. In the current version of ARW, microphysics is carried out at the end of the time-step as an adjustment process, and so does not provide tendencies but directly updates the state variables. The rationale for this is that condensation adjustment should be at the end of the time-step to guarantee that the final saturation balance is accurate for the updated temperature and moisture. However, it is also important to have the latent heating forcing for potential temperature during the dynamical sub-steps, and this is done by saving the microphysical heating as an approximation for the next time-step as described in Section 3.1.4.

Currently, the sedimentation process is accounted for inside the individual microphysics modules, and, to prevent instability in the calculation of the vertical flux of precipitation, either a smaller time step is allowed or a Lagrangian scheme is used. The saturation adjustment is also included inside the microphysics. In the future, however, it might be separated into an individual subroutine to enable the remaining microphysics to be called less frequently than the model's advection step for efficiency.

The various microphysics options have differing numbers of moisture variables, depending on the ice-phase and mixed-phase processes included. Mixed-phase processes are those that result from the interaction of ice and water particles, such as riming that produces graupel or hail. As a general rule, for grid sizes less than 10 km, where updrafts may be resolved, mixed-phase schemes should be used, particularly in convective or icing situations. For coarser grids it may not be worth the added expense of these schemes because riming is not likely to occur with the relatively weak vertical motion that is resolved. Many schemes are also double-moment for some species and include number per unit dry air mass for those as extra advected variables.

8.1.1 Kessler scheme

This scheme (Kessler, 1969), which was taken from the COMMAS model (Wicker and Wilhelmson, 1995), is a simple warm cloud scheme that includes water vapor, cloud water, and rain. The microphysical processes included are: the production, fall, and evaporation of rain; the accretion and autoconversion of cloud water; and the production of cloud water from condensation.

8.1.2 Purdue Lin scheme

Six classes of moisture variables are included: water vapor, cloud water, rain, cloud ice, snow, and graupel. All parameterization production terms are based on Lin et al. (1983) and Rutledge and Hobbs (1984) with some modifications, including condensation adjustment with saturation assumptions following Tao et al. (1989) and ice sedimentation. Compared to Kessler, the treatment of ice processes in this and all the other microphysics options increases the level of sophistication, and makes it more generally suitable for use in research studies. The scheme is taken from the Purdue cloud model, and the details can be found in Chen and Sun (2002).

8.1.3 WRF Single-Moment 3-class (WSM3) scheme

The WRF single-moment 3-class microphysics scheme follows Hong et al. (2004) including ice sedimentation and other new ice-phase parameterizations. A major difference from other approaches is that a diagnostic relation is used for ice number that is based on ice mass content rather than temperature. The computational procedures are described in Hong and Lim (2006). As with WSM5 and WSM6, the fall terms are computed using a Lagrangian technique instead of time-splitting that was used in earlier versions of these schemes. The WSM3 scheme predicts three categories of moist variables: water vapor, cloud water/ice, and rain/snow, making it a so-called simple-ice scheme. It follows Dudhia (1989) in assuming cloud water and rain for temperatures above freezing, and cloud ice and snow for temperatures below freezing. This scheme is computationally efficient for the inclusion of ice processes, but lacks supercooled water and gradual melting rates.

8.1.4 WSM5 scheme

This scheme is similar to the WSM3 simple ice scheme. However, water vapor, rain, snow, cloud ice, and cloud water are held in five different arrays. Note that the numbering of these schemes includes water vapor as a class which is different from other numbering conventions. Thus, it allows supercooled water to exist, and a gradual melting of snow falling below the melting layer. Details can be found in Hong et al. (2004), and Hong and Lim (2006). As with WSM6, the saturation adjustment follows Dudhia (1989) and Hong et al. (1998) in separately treating ice and water saturation processes, rather than a combined saturation such as the Purdue Lin (above) and Goddard (Tao et al., 1989) schemes. This scheme is efficient in intermediate grids between the mesoscale and cloud-resolving grids.

8.1.5 WSM6 scheme

The six-class scheme extends the WSM5 scheme to include graupel and its associated processes. Some of the graupel-related terms follow Lin et al. (1983), but its ice-phase behavior is much different due to the changes of Hong et al. (2004). A new method is introduced for representing mixed-phase particle fall speeds for the snow and graupel particles by assigning a single fallspeed to both that is weighted by the mixing ratios, and applying that fallspeed to both sedimentation and accretion processes (Dudhia et al., 2008). The behavior of the WSM3, WSM5, and WSM6 schemes differ little for coarser mesoscale grids, but they work differently on cloud-resolving grids. Of the three WSM schemes, the WSM6 scheme is the most suitable for cloud-resolving grids, considering the efficiency and theoretical backgrounds (Hong and Lim, 2006). All of the WSM and WDM schemes compute effective radii for ice, snow and cloud water to interact with RRTMG radiation. All except WSM3 compute reflectivity diagnostics.

8.1.6 WDM5 and WDM6 schemes

These schemes have the same ice-phase processes as WSM5 and WSM6, but warm-rain processes are now double-moment calculations (Lim and Hong, 2010) with number for cloud and rain being calculated as prognostic variables. The schemes are therefore also sensitive to cloud-condensation nuclei (CCNs) numbers that are also advected, but these are initialized with a constant value. As with all the WSM schemes, sedimentation is handled with a Lagrangian scheme. Also as with WSM5 and WSM6, the method of Dudhia et al. (2008) is used to provide a combined fallspeed for snow and graupel.

8.1.7 WSM7 and WDM7 schemes

The extension of WSM6 and WDM6 to include hail as a separate category from graupel is also available as a choice in WRF as WSM7 and WDM7 respectively (Bae et al., 2018). These schemes, by allowing for hail, also can give more intense precipitation rates. As with the other WDM schemes, WDM7 only affects the cloud and rain water processes.

8.1.8 Eta Grid-scale Cloud and Precipitation (2001) scheme

This is also known as EGCP01 or the Eta Ferrier scheme. The scheme predicts changes in water vapor and condensate in the forms of cloud water, rain, cloud ice, and precipitation ice (snow/graupel/sleet). The individual hydrometeor fields are combined into total condensate, and it is the water vapor and total condensate that are advected in the model. Local storage arrays retain first-guess information that extract contributions of cloud water, rain, cloud ice, and precipitation ice of variable density in the form of snow, graupel, or sleet. The density of precipitation ice is estimated from a local array that stores information on the total growth of ice by vapor deposition and accretion of liquid water. Sedimentation is treated by partitioning the time-averaged flux of precipitation into a grid box between local storage in the box and fall out through the bottom of the box. This approach, together with modifications in the treatment of rapid microphysical processes, permits large time steps to be used with stable results. The mean size of precipitation ice is assumed to be a function of temperature following the observational results of Ryan (1996). Mixed-phase processes are now considered at temperatures warmer than -30°C (previously -10°C), whereas ice saturation is assumed for cloudy conditions at colder temperatures. Further description of the scheme can be found in Sec. 3.1 of the November 2001 Technical Procedures Bulletin (TPB). An advection option has been added for this scheme that explicitly advects cloud water, rain and ice and includes a rimed fraction.

8.1.9 Thompson et al. and aerosol-aware Thompson-Eidhammer schemes

This is a bulk microphysics scheme that has double-moment ice and rain and has been updated as described by Thompson et al. (2008). The aerosol-aware scheme (Thompson and Eidhammer, 2014) additionally has prognostic variables for ice-friendly and water-friendly nuclei that are initialized from a global monthly climatology based on aerosols. The scheme has been developed for midlatitude convective, orographic and snowfall conditions especially at convection-permitting grid scales. It is used operationally in the RAP/HRRR forecasting system. The ice, snow, and cloud droplet radii are passed to the RRTMG radiation schemes along with the clear-sky aerosols for optical depth calculations. Reflectivity is also diagnosed.

8.1.10 Goddard Cumulus Ensemble Model scheme

The Goddard Cumulus Ensemble (GCE) models (Tao and Simpson, 1993) one-moment bulk microphysical schemes are mainly based on Lin et al. (1983) with additional processes from Rutledge and Hobbs (1984). However, the Goddard microphysics schemes have several modifications.

First, there is an option to choose either graupel or hail as the third class of ice in the so-called 3ICE scheme (McCumber et al., 1991). Graupel has a relatively low density and a high intercept value (i.e., more numerous small particles). In contrast, hail has a relative high density and a low intercept value (i.e., more numerous large particles). These differences can affect not only the description of the hydrometeor population and formation of the anvil-stratiform region but also the relative importance of the microphysical-dynamical-radiative processes.

Second, new saturation techniques (Tao et al., 1989, 2003) were added. These saturation techniques are basically designed to ensure that super saturation (sub-saturation) cannot exist at a grid point that is clear (cloudy).

Third, all microphysical processes that do not involve melting, evaporation or sublimation (i.e., transfer rates from one type of hydrometeor to another) are calculated based on one thermodynamic state. This ensures that all of these processes are treated equally.

Fourth, the sum of all sink processes associated with one species will not exceed its mass. This ensures that the water budget will be balanced in the microphysical calculations .

The Goddard microphysics has a simpler option, which is equivalent to a two-ice (2ICE) scheme having only cloud ice and snow. This option may be sufficient for coarse resolution simulations (i.e., $>$ 10 km grid size). The two-class ice scheme could be applied for winter and frontal convection.

8.1.11 Goddard 4ICE scheme

The new Goddard 4ICE scheme (Lang et al., 2014; Tao et al., 2016) is a significant improvement over the previous Goddard 3ICE WRF scheme. The new 4ICE scheme explicitly predicts the evolution of hail in addition to the traditional ice, snow, and graupel categories available in the 3ICE scheme. The 4ICE scheme was built upon improved versions of the Goddard 3ICE scheme developed for the Goddard Cumulus Ensemble model and includes dozens of new/modified functions regarding ice microphysics and unique particle-size mapping and observation-driven snow density.

8.1.12 Morrison et al. 2-Moment scheme

The Morrison et al. (2008) scheme is based on the two-moment bulk microphysics scheme of Morrison et al. (2005) and Morrison and Pinto (2006). Five species of hydrometeor are included with water vapor: cloud droplets, cloud ice, rain, snow, and graupel/hail. The code has a user-specified switch to include either graupel or hail. Prognostic variables include number and mass mixing ratios of cloud ice, rain, snow, and graupel/hail, and mixing ratios of cloud droplets and water vapor (total of 10 variables). The prediction of two-moments (i.e., both number and mass mixing ratio) allows for a more robust treatment of the particle size distributions, which are a key for calculating the microphysical process rates and cloud/precipitation evolution. Several liquid, ice, and mixed-phase processes are included. Particle size distributions are treated using gamma functions, with the associated intercept and slope parameters derived from the predicted mixing ratio and number. The scheme has been extensively tested and compared with both idealized and real case studies covering a wide range of conditions.

8.1.13 Milbrandt-Yau Double-Moment scheme

The Milbrandt and Yau (2005) scheme is a fully double-moment scheme that carries graupel and hail as separate species. It therefore has 12 prognostic variables in addition to water vapor.

8.1.14 CAM Morrison-Gettelman scheme

The Morrison and Gettelman (2008) scheme matches the microphysics used in the CESM CAM5.1 climate model. It is added as part of the CAM suite of physics. It carries cloud water, ice, rain and snow as double-moment prognostic variables. It is primarily designed for global low resolution applications.

8.1.15 Stony-Brook University Lin-Colle scheme

A single-moment bulk microphysics scheme (Lin and Colle, 2011) that predicts cloud water, rain, ice and snow and also carries riming intensity to represent graupel densities.

8.1.16 NSSL microphysics schemes

There are multiple National Severe Storms Laboratory (NSSL) options by Mansell et al. (2010) ranging from single-moment with graupel properties specified (Gilmore et al., 2004) or predicted with hail added to double-moment of all species with or without hail and also optionally adding CCNs.

8.1.17 HUJI spectral bin microphysics schemes

The Hebrew University of Jerusalem, Israel, (HUJI) spectral bin microphysics (SBM) scheme has “fast” and “full” versions. Both resolve size distributions into 33 mass-doubling size bins for each type of particle. The fast scheme (Khain et al., 2010) has four particle types cloud/rain, ice/snow, graupel and aerosols, while the full scheme (Khain et al., 2004) has eight types cloud/rain, snow, graupel, aerosols, ice plates, columns and dendrites and hail. The aerosols are cloud condensation nuclei. Note that each bin variable is advected making these schemes computationally an order of magnitude more costly than bulk microphysics options. Also cloud-resolving to LES scales are required to represent the details of motion and supersaturation that such schemes require.

8.1.18 Predicted Particle Properties (P3) scheme

The P3 scheme (Morrison and Milbrandt, 2015) uses a novel approach for predicting properties of ice particles as they transition to snow and may rime into graupel. The scheme has double-moment rain with an option for double-moment cloud to handle aerosol effects. The ice is also double-moment, but also has associated scalars for rimed mass and volume that allow the ice-particle properties to evolve rather than imposing categories like snow, graupel and hail.

8.1.19 Jensen ISHMAEL microphysics

The ISHMAEL (Ice-Spheroids Habit Model with Aspect-ratio EvoLution) scheme (Jensen et al., 2017) can predict ice-particle habits that are defined by their aspect ratios and volumes and how these develop through deposition and riming. Up to three independent habits are carried which contain generalized particles that represent the whole evolution from ice to snow to graupel together with their numbers per unit dry air mass.

8.1.20 National Taiwan University (NTU) microphysics scheme

The NTU scheme is a multi-moment microphysics scheme (Tsai and Chen, 2020). It is double-moment for liquid phase and triple moment for ice phase hydrometeors with additional consideration of ice crystal shape and density variations. The condensation nuclei and ice nuclei are tracked separately in the processes of cloud/rain activation and ice deposition-nucleation using predicted supersaturation. The triple-moment (the zeroth, second and third moments) closure is applied to the evolution of ice particle's spectrum. The classification for solid-phase hydrometeors (pristine ice, snow aggregate, rimed ice and hailstone) is redefined according to their key formation mechanisms, while the shape and apparent density of ice crystals are allowed to evolve gradually according to the growth conditions. The fall speed of each frozen particle depends on its shape and density.

8.2 Cumulus Parameterization

These schemes are responsible for the sub-grid-scale effects of convective and/or shallow clouds. The schemes are intended to represent vertical fluxes due to unresolved updrafts and downdrafts and compensating motion outside the clouds. They operate only on individual columns where the scheme is triggered and provide vertical heating and moistening profiles. Some schemes additionally provide cloud and precipitation field tendencies in the column, and some provide momentum tendencies due to convective transport of momentum. The schemes all provide the convective component of surface rainfall.

Cumulus parameterizations are theoretically only valid for coarser grid sizes, (e.g., greater than 10 km), where they are necessary to properly release convective available potential energy on a realistic time scale in the convective grid columns. While the assumptions about the convective eddies being entirely sub-grid-scale break down for finer grid sizes, sometimes these schemes have been found to be helpful in triggering convection in 5–10 km grid applications. Generally, they should not be used when the model can resolve the deep convective updrafts itself (e.g., ≤ 4 km grid).

A few schemes have developed capability to adapt to finer grid sizes. As the grid sizes decrease, these schemes will reduce the effect of deep convection accordingly, or gradually turn off deep convection and let the shallow convection take over.

Note that some cumulus schemes include both deep and shallow convection, while others only include deep convection.

8.2.1 Kain-Fritsch schemes

Modified Kain-Fritsch Scheme

The modified version of the Kain-Fritsch scheme (Kain, 2004) is based on Kain and Fritsch (1990) and Kain and Fritsch (1993), but has been modified based on testing within the Eta model. As with the original KF scheme, it utilizes a simple cloud model with moist updrafts and downdrafts, including the effects of detrainment, entrainment, and relatively simple microphysics. It differs from the original KF scheme in the following ways:

- A minimum entrainment rate is imposed to suppress widespread convection in marginally unstable, relatively dry environments.
- Shallow (non precipitating) convection is allowed for any updraft that does not reach minimum cloud depth for precipitating clouds; this minimum depth varies as a function of cloud-base temperature.
- The entrainment rate is allowed to vary as a function of low-level convergence.
- Downdraft changes:
  - Source layer is the entire 150 – 200 mb deep layer just above cloud base.
  - Mass flux is specified as a fraction of updraft mass flux at cloud base. Fraction is a function of source layer RH rather than wind shear or other parameters, i.e., old precipitation efficiency relationship not used.
  - Detrainment is specified to occur in updraft source layer and below.
- A new way to compute perturbation temperature added to the testing updraft parcel is implemented based on Ma and Tan (2009). This perturbation temperature is a function of horizontal and vertical moisture advection, rather than vertical velocity. This changes the trigger function in the original scheme to work better in a weakly forced environment.
- Subgrid cloud fraction due to both deep and shallow convection is estimated and passed to the radiation schemes (Alapaty et al., 2012).

Multi-Scale Kain-Fritsch Scheme

This is based on the original Kain-Fritsch scheme, and modified to allow the scheme to adapt when the grid-size decreases from the mesoscale range (a few tenths of kilometers) to convective scales (a few kilometers) (Zheng et al., 2016). The main modification includes a dynamic adjustment time scale for CAPE removal, a modified scale-dependent minimum entrainment rate, and an enhanced grid-scale vertical motion using subgrid scale updraft mass fluxes. The scheme also includes an option to interact with climatological aerosol through an addition of subgrid-scale cloud microphysics (Glotfelty el al., 2019).

Kain-Fritsch Cumulus Potential Scheme

In this version of the Kain-Fritsch scheme, the trigger function in the original scheme is replaced by a method that relates the initiation of convection to the distribution of temperature and moisture in the boundary layer via probability density functions (PDFs) (Berg et al., 2013). The scheme has tunable parameters to set for the critical cumulative frequency of bins in order to trigger deep convection, and minimum frequency of a bin within the PDF required to form shallow convection. The scheme also computes the cumulus cloud fraction due to shallow convection and feeds it into the radiation physics. In addition, the scheme can include vertical transport of trace gases and aerosols, aqueous chemistry, wet removal and aerosol effect on cloud drop number when activated with the MOSAIC chemistry (Berg et al., 2015).

8.2.2 Betts-Miller-Janjic scheme

The Betts-Miller-Janjic (BMJ) scheme (Janjic, 1994, 2000) was derived from the Betts-Miller (BM) convective adjustment scheme (Betts, 1986; Betts and Miller, 1986). However, the BMJ scheme differs from the Betts-Miller scheme in several important aspects. The deep convection profiles and the relaxation time are variable and depend on the cloud efficiency, a nondimensional parameter that characterizes the convective regime (Janjic, 1994). The cloud efficiency depends on the entropy change, precipitation, and mean temperature of the cloud. The shallow convection moisture profile is derived from the requirement that the entropy change be small and nonnegative (Janjic, 1994). The BMJ scheme has been optimized over years of operational application at NCEP, so that, in addition to the described conceptual differences, many details and/or parameter values differ from those recommended in Betts (1986) and Betts and Miller (1986). Recently, attempts have been made to refine the scheme for higher horizontal resolutions, primarily through modifications of the triggering mechanism. In particular:

- A floor value for the entropy change in the cloud is set up below which the deep convection is not triggered;
- In searching for the cloud top, the ascending parcel mixes with the environment; and
- The work of the buoyancy force on the ascending parcel is required to exceed a prescribed positive threshold.

8.2.3 Grell Schemes

Grell-Devenyi Ensemble Scheme

Grell and Devenyi (2002) introduced an ensemble cumulus scheme in which effectively multiple cumulus schemes and variants are run within each grid box and then the results are averaged to give the feedback to the model. In principle, the averaging can be weighted to optimize the scheme, but the default is an equal weight. The schemes are all mass-flux type schemes, but with differing updraft and downdraft entrainment and detrainment parameters, and precipitation efficiencies. These differences in static control are combined with differences in dynamic control, which is the method of determining cloud mass flux. The dynamic control closures are based on convective available potential energy (CAPE or cloud work function), low-level vertical velocity, or moisture convergence. Those based on CAPE either balance the rate of change of CAPE or relax the CAPE to a climatological value, or remove the CAPE in a convective time scale. The moisture convergence closure balances the cloud rainfall to the integrated vertical advection of moisture. Another control is the trigger, where the maximum cap strength that permits convection can be varied. These controls typically provide ensembles of 144 members.

Grell-3 Scheme

The Grell-3 scheme was first introduced in Version 3.0. It shares a lot in common with the Grell-Devenyi in scheme, being based on an ensemble mean approach, but the quasi-equilibrium approach is no longer included among the ensemble members. The scheme is distinguished from other cumulus schemes by allowing subsidence effects to be spread to neighboring grid columns, making the method more suitable to grid sizes less than 10 km, while it can also be used at larger grid sizes where subsidence occurs within the same grid column as the updraft.

Grell-Freitas Scheme

The Grell-Freitas scheme (Grell and Freitas, 2014) is based on Grell-Devenyi scheme which considers a stochastic approach to cumulus convection, and modified to work across grid-sizes from mesoscale to convective scales. The scheme relates the convective updraft fraction to the entrainment rate, which in turn is related the cloud radius. As the grid size decreases, the fractional updraft area increases, which is equivalent to decreasing the unit mass flux required to stabilize the atmosphere.

8.2.4 Simplified Arakawa-Schubert Schemes

This group of schemes is based on simplified Arakawa-Schubert scheme (SAS) (Grell, 1993) which considers only one type of cloud instead of an ensemble. They all use the quasi-equilibrium closure. They vary by how they handle convective downdrafts, shallow convection, momentum transport (all three not included in the original AS and last two not in SAS), entrainment/detrainment and scale-aware aspects.

Original SAS Scheme

This is the convective scheme used by GFS from 1995 to 2000 (Pan and Wu, 1995). This version includes a moist convective downdraft, has a shallow component that uses an eddy diffusion approach, and considers convective momentum transport which depends on vertical wind shear. However the convective momentum transport was not implemented in ARW.

New SAS Scheme

The so-called NSAS scheme is an updated SAS scheme operational in GFS since July 2010 (Han and Pan, 2011). In this version, the shallow convection using an eddy diffusion approach is replaced by a mass-flux scheme similarly formulated to deep convection, with entrainment/detrainment following LES studies. The deep convection is made stronger by removing random cloud-top selection and increasing the maximum allowable mass-flux at the cloud base. The entrainment and detrainment are modified to be dependent on environmental relative humidity as in the new Tiedtke scheme. The trigger function is modified to have some dependency on large-scale vertical velocity and subcloud layer environmental moisture. The scheme uses a similar convective momentum transport formulation, but with a reduced effect.

Scale-aware SAS Scheme

This variation of the SAS scheme is based on NSAS, but with scale-aware features added. The fractional area occupied by the deep convection increases based on updraft radius which is in turn dependent on entrainment. This is similar to the assumption used by the Grell-Freitas scheme, but using the actual entrainment rate at cloud base. This scheme is currently employed in Hurricane WRF.

KIAPS Scale-aware SAS Scheme

This is another variation of the updated NCEP SAS scheme from 2010, with an added scale-aware dependency (Kwon and Hong, 2017). The scale-awareness is implemented by considering the fractional updraft area to increase as the grid size decreases. Two factors determine the increase: one is empirical and the other is dependent on the ratio of grid vertical velocity over convective updraft velocity. In addition to mass-flux dependency on the grid size, the convective inhibition and convective cloud water detrainment are also made to depend on grid size. Note that this is a deep-only scheme and designed to be run with the separate shallow NSAS cumulus scheme.

8.2.5 Zhang-McFarlane Scheme

The Zhang-McFarlane scheme is a mass-flux scheme and it is only for deep convection (Zhang and McFarlane, 1995). It follows the ideas of Arakawa-Schubert, but makes simplified assumptions. One of the assumptions is that instead of using a spectrum of cloud plumes, it specifies the distribution of the updraft assuming that they all have the same cloud base mass flux, but each has a characteristic entrainment rate. It also assumes that the convection removes CAPE at an exponential rate with a specified adjustment time scale. The scheme detrains cloud liquid and ice, and considers momentum transport. The scheme is ported from CAM4, and tested with other CAM physics. For example, it can be used together with Park-Bretherton shallow convection option and CAM microphysics.

8.2.6 Tiedtke Schemes

There are two versions of the original Tiedtke scheme (Tiedtke, 1989) in ARW. The first version is based on an earlier version of the scheme from ECMWF, and the newer version is closer to the code in recent IFS by ECMWF.

Tiedtke Scheme

The Tiedtke scheme is a mass-flux scheme, and it parameterizes deep, shallow and midlevel convection. It represents the cloud ensemble by a bulk cloud model, and considers entrainment and detrainment and downdrafts. It uses a CAPE closure to determine the strength of the deep and midlevel convection, and surface evaporation for shallow convection. In the version implemented in WRF (Zhang and Wang, 2011), turbulent entrainment and detrainment are added and turbulent entrainment for shallow convection is increased to promote boundary layer cloud formation. Another modification is to change how detrained cloud at the top is treated: in the original scheme, it evaporates immediately; and in the current scheme, it is added to the grid scale. To limit the deep convection in drier regions, a minimum relative humidity of 80% is imposed for the mean RH between cloud base and top.

New Tiedtke Scheme

This is an updated version of Tiedtke scheme, and it is closer to the one used in the recent ECMWF IFS (Zhang and Wang, 2017). The updates include trigger functions for deep and shallow convection, closures for deep and shallow convection, convective adjustment time scale, entrainment and detrainment rates for all types of convection, conversion from cloud water/ice to rain/snow and options for momentum transport. The entrainment for deep convection is made to depend on environmental moisture which helps the simulated tropical systems. The updated CAPE closure for deep convection relaxes to CAPE generated in the planetary boundary layer which improves the diurnal precipitation over land. The convective adjustment time is no longer a constant, but it depends on the vertical velocity averaged in the updraft and cloud depth.

8.3 Shallow Cumulus Parameterization

Similar to the deep cumulus parameterization, these schemes represent the sub-grid-scale transport of heat and moisture in shallow, and sometimes non-precipitating, clouds. Since the scale of shallow convective cloud is generally smaller than its deep counterpart, it should be used in models when a deep cumulus scheme is turned off. These stand-alone shallow schemes can therefore serve that purpose.

8.3.1 University of Washington Scheme

The University of Washington shallow convection scheme is a mass flux scheme (Park and Bretherton, 2009) using moist adiabatically conserved variables of total specific humidity and liquid water potential temperature. The scheme allows for precipitation, considers momentum mixing, and an entrainment formulation that depends on the vertical velocity of the updraft. The scheme's closure is controlled by convective inhibition. This scheme is adopted from CAM4.

8.3.2 GRIMs Scheme

The GRIMs (The Global and Regional Integrated Model System) shallow convection scheme (Hong and Jang, 2018) is based on the shallow convection scheme of Tiedtke and uses an eddy-diffusivity method. The modification to the Tiedtke scheme includes defining the cloud base at the top of the PBL and diffusion coefficient as a function of relative humidity, mixed-layer vertical velocity scale and the entrainment depth at the PBL top. The scheme is non-precipitating and can only be used with YSU PBL scheme.

8.3.3 NSAS Scheme

This shallow convection scheme is the same as the shallow component in the NSAS scheme.

8.3.4 Deng Scheme

The Deng scheme (Deng et al., 2003) is a mass flux scheme. It considers both buoyant updraft and cloud with nearly neutral buoyancy. The scheme triggers convection based on the turbulent kinetic energy (TKE) in the boundary layer, and its closure uses a hybrid formulation that depends on both boundary layer TKE as well as CAPE. In conditionally unstable environment, the scheme transitions to the Kain-Fritsch deep convective scheme. The scheme also predicts cloud fraction and cloud liquid content from the detrained convective updraft air.

8.4 Surface Layer

The surface layer schemes calculate friction velocities and exchange coefficients that enable the calculation of surface heat and moisture fluxes by the land-surface models and surface stress in the planetary boundary layer scheme. Over water surfaces, the surface fluxes and surface diagnostic fields are computed in the surface layer scheme itself. The schemes provide no tendencies, only the stability-dependent information about the surface layer for the land-surface and PBL schemes. Currently, each surface layer option is tied to particular boundary-layer options, but in the future more interchangeability and options may become available. Note that some boundary layer schemes (ACM2 and MRF) require the thickness of the surface layer in the model to be representative of the actual surface layer (e.g. 50-100 meters) while most others can have thin surface layers. The schemes use Monin-Obukhov similarity theory with variations in the stability functions and methods for computing roughness lengths. Similarity theory relates the information at the lowest model level to the surface via a stability dependent, approximately log, profile of wind and scalars. Diagnostic outputs of 2m and 10m quantities are consistently computed with the profiles of these schemes.

8.4.1 Revised MM5 similarity theory

Jimenez et al. (2012) revised the previous MM5 similarity theory by improving the consistency between Ri and z/L and removing limits by using new stability functions for stable and unstable conditions that also include the extra term $\psi(z_0/L)$. The scheme gives largely similar results to the old option but shows some improvement in the transition periods. Both the MM5-based schemes have the same thermal roughness length options in addition to convective velocity. The thermal roughness length allows for a reduced roughness length in the calculation of θ_* while the convective velocity adds to u_* for the purposes of scalar fluxes but not friction. Over the ocean, options for tropical cyclones include a Donelan-based formulation for wave roughness and a Garratt formulation or constant z_{0q} for enthalpy fluxes.

8.4.2 Similarity theory (MYJ/Eta)

The Eta surface layer scheme (Janjic, 1996, 2002) is based on similarity theory (Monin and Obukhov, 1954). The scheme includes parameterizations of a viscous sub-layer. Over water surfaces, the viscous sub-layer is parameterized explicitly following Janjic (1994). Over land, the effects of the viscous sub-layer are taken into account through variable roughness height for temperature and humidity as proposed by Zilitinkevich (1995). The Beljaars (1994) correction is applied in order to avoid singularities in the case of an unstable surface layer and vanishing wind speed. The surface fluxes are computed by an iterative method. This surface layer scheme must be run in conjunction with the Eta (Mellor-Yamada-Janjic) PBL scheme, and is therefore sometimes referred to as the MYJ surface scheme.

8.4.3 QNSE similarity theory

This should be used with the Quasi-Normal Scale Elimination (QNSE) PBL scheme (Sukoriansky et al., 2005) named for a theoretical technique employed to derive sub-grid mixing properties of stratified turbulence. The theory provides effective viscosity and diffusivity as a function of Richardson number that are used in the stable PBL regime and the surface layer similarity functions for stable conditions. The scheme is also distinguished by have a Prandtl number of 0.7 instead of a value near 1.

8.4.4 MYNN surface layer

The MYNN surface-layer scheme includes several forms for stability functions with Dyer and Hicks (1970) used by default. There are also several options for handling thermal roughness lengths and the fluxes over water. It is to be used with the MYNN PBL options that is part of the RAP/HRRR physics suite.

8.4.5 Similarity theory (PX)

The PX surface layer scheme (Pleim, 2006) was developed as part of the PX LSM but can be used with any LSM or PBL model. This scheme is based on similarity theory and includes parameterizations of a viscous sub-layer in the form of a quasi-laminar boundary layer resistance accounting for differences in the diffusivity of heat, water vapor, and trace chemical species. The surface layer similarity functions are estimated by analytical approximations from state variables.

8.4.6 TEMF surface layer

This surface layer scheme is designed to work with the Total Energy Mass Flux (TEMF) PBL scheme (Angevine et al., 2010). The similarity functions used in this scheme are functions of Ri for stable conditions, and consider unstable conditions similarly to neutral conditions.

8.4.7 Similarity theory (MM5) – old version

This scheme is now superseded by the Revised MM5 similarity theory scheme (see above) but still available as an option. This scheme uses stability functions from Paulson (1970), Dyer and Hicks (1970), and Webb (1970) to compute surface exchange coefficients for heat, moisture, and momentum. A convective velocity following Beljaars (1994) is used to enhance surface fluxes of heat and moisture. A Charnock relation relates roughness length to friction velocity over water. There are four stability regimes following Zhang and Anthes (1982). This surface layer scheme must be run in conjunction with the MRF or YSU PBL schemes. Since Version 3, there has been an option to replace the Charnock relation for roughness length with a Donelan relation that has lower drag at hurricane-force wind speeds, and may be more suitable for hurricane simulations. Also for water points, the Beljaars formulation for convective velocity is replaced by one proportional only to the vertical thermal gradient to help in weak-wind situations.

8.5 Land-Surface Model and Other Surface Options

The land-surface models (LSMs) use atmospheric information from the surface layer scheme, radiative forcing from the radiation scheme, and precipitation forcing from the microphysics and convective schemes, together with internal information on the land's state variables and land-surface properties, to provide heat and moisture fluxes over land points and sea-ice points. These fluxes provide a lower boundary condition for the vertical transport done in the PBL schemes (or the vertical diffusion scheme in the case where a PBL scheme is not run, such as in large-eddy mode). The land-surface models have various degrees of sophistication in dealing with thermal and moisture fluxes in multiple layers of the soil and also may handle vegetation, root, and canopy effects and surface snow-cover prediction. The land-surface model provides no tendencies, but does update the land's state variables which include the ground (skin) temperature, soil temperature profile, soil moisture profile, snow cover, and possibly canopy properties. There is no horizontal interaction between neighboring points in the LSM, so it can be regarded as a one-dimensional column model for each WRF land grid-point.

8.5.1 5-layer thermal diffusion

This simple LSM is based on the MM5 5-layer soil temperature model. Layers are 1, 2, 4, 8, and 16 cm thick. Below these layers, the temperature is fixed at a deep-layer average. The energy budget includes radiation, sensible, and latent heat flux. It also allows for a snow-cover flag, but the snow cover is fixed in time. Soil moisture is also fixed with a landuse- and season-dependent constant value, and there are no explicit vegetation effects.

8.5.2 Noah LSM

The Noah LSM is the successor to the OSU LSM described by Chen and Dudhia (2001). The scheme was developed jointly by NCAR and NCEP, and is a unified code for research and operational purposes, being almost identical to the code used in the NCEP North American Mesoscale Model (NAM). This has the benefit of being consistent with the time-dependent soil fields provided in the analysis datasets. This is a 4-layer soil temperature and moisture model with canopy moisture and snow cover prediction. The layer thicknesses are 10, 30, 60 and 100 cm (adding to 2 meters) from the top down. It includes root zone, evapotranspiration, soil drainage, and runoff, taking into account vegetation categories, monthly vegetation fraction, and soil texture. The scheme provides sensible and latent heat fluxes to the boundary-layer scheme. The Noah LSM additionally predicts soil ice, and fractional snow cover effects, is linked to urban model options, and considers surface emissivity properties, which are all new since the OSU scheme. There is a sub-tiling (mosaic) option for this LSM (Li et al., 2013) that allows fractional areas of different land-use categories within a grid cell.

8.5.3 NoahMP LSM

This model follows on from the Noah LSM and is a large collaborative effort (Niu et al., 2011; Yang et al., 2011) to allow for multiple parameterization options for each part of the LSM physics making it a multi-parameterization (MP) scheme. The sub-options within this scheme include dynamic vegetation, stomatal resistance, runoff/groundwater, soil permeability, radiative transfer, soil and snow options and surface evaporation resistance options. The scheme has 4 soil layers and 3 snow layers. There are also a crop model options. NoahMP is linked to all the urban options like Noah (UCM, BEP and BEM).

8.5.4 Rapid Update Cycle (RUC) Model LSM

The RUC LSM has a multi-level soil model (6 levels is default, could be 9 or more) with higher resolution in the top part of soil domain (0, 5, 20, 40, 160, 300 cm is default). The soil model solves heat diffusion and Richards moisture transfer equations, and in the cold season takes into account phase changes of soil water (Smirnova et al., 1997, 2000). The RUC LSM also has a multi-layer snow model with changing snow density, refreezing liquid water percolating through the snow pack, snow depth and temperature dependent albedo, melting algorithms applied at both snow-atmosphere interface and snow-soil interface, and simple parameterization of fractional snow cover with possibility of grid averaged skin temperature going above freezing. It also includes vegetation effects and canopy water. The RUC LSM has a layer approach to the solution of energy and moisture budgets. The layer spans the ground surface and includes half of the first atmospheric layer and half of the top soil layer with the corresponding properties (density, heat capacity, etc.) The residual of the incoming fluxes (net radiation, latent and sensible heat fluxes, soil heat flux, precipitation contribution into heat storage, etc.) modifies the heat storage of this layer. An implicit technique is applied to the solution of these equations. Prognostic variables include soil temperature, volumetric liquid, frozen and total soil moisture contents, surface and sub-surface runoff, canopy moisture, evapotranspiration, latent, sensible and soil heat fluxes, heat of snow-water phase change, skin temperature, snow depth and density, and snow temperature. This option also has a sub-grid mosaic sub-option to allow for fractional areas of different land-use categories.

8.5.5 Pleim-Xiu LSM

The PX LSM (Pleim and Xiu, 1995; Xiu and Pleim, 2001), originally based on the ISBA model of Noilhan and Planton (1989), includes a 2-layer force-restore soil temperature and moisture model. The top layer is taken to be 1 cm thick, and the lower layer is 99 cm. The PX LSM features three pathways for moisture fluxes: evapotranspiration, soil evaporation, and evaporation from wet canopies. Evapotranspiration is controlled by bulk stomatal resistance that is dependent on root zone soil moisture, photosynthetically active radiation, air temperature, and the relative humidity at the leaf surface. Grid aggregate vegetation and soil parameters are derived from fractional coverages of land use categories and soil texture types. There are two indirect nudging schemes that correct biases in 2-m air temperature and RH by dynamic adjustment of soil moisture (Pleim and Xiu, 2003) and deep soil temperature (Pleim and Gilliam, 2008). Note that a small utility program (ipxwrf) can be used to propagate soil moisture and temperature between consecutive runs to create a continuous simulation of these quantities. The scheme also allows for sub-grid variability by averaging grid-cell properties from sub-grid fractions.

8.5.6 Community Land Model (CLM4)

CLM4 is a version of the land component of the Coupled Earth System Model (CESM) that is used for climate modeling (Oleson et al., 2010; Lawrence et al., 2011). The model has 10 soil layers and 5 snow layers. The scheme allows for sub-grid tiling by 5 main categories (glacier, wetland, vegetated, lake and urban), and 4 vegetated sub-tiles of different "plant functional types" (PFTs). This has a rather comprehensive set of physics related to land-surface, soil, hydrology, and vegetation processes, also including urban areas, glaciers, and a multi-layer lake model that is also an option to run with other LSMs in WRF.

8.5.7 Simplified Simple Biosphere Model (SSiB)

SSiB (Xue et al., 1991; Sun and Xue, 2001), the LSM from the UCLA GCM as another climate option for land-surface physics. It has a 2-layer bulk soil temperature model, vegetation effects at the surface, 3 layers of soil moisture with a root zone, and a 4-layer snow treatment. It also predicts canopy temperature and moisture.

8.5.8 Urban Canopy Model

This can be run as an option with the Noah and NoahMP LSMs. In order to represent the city scale effects on the mesoscale, an urban canopy model (UCM) originally developed by Kusaka et al. (2001) and Kusaka and Kimura (2004) and later on modified by Chen et al. (2006), is coupled to the WRF model via Noah Land surface model. In the UCM, all the urban effects in the vertical are assumed to be subgrid scale meaning that the urban processes are occurring below the lowest model level. The urban canopy model includes:

- Parameterization of street canyons to represent the urban geometry
- Shadowing from building and radiation reflection
- An exponential wind profile in the canopy layer
- A multilayer heat equation for roof, wall and road surfaces

The urban canopy model estimates the surface temperature and heat fluxes from the roof, wall and road surface. It also calculates the momentum exchange between the urban surface and the atmosphere. If they are available, the UCM can take three different densities of urban development using special land-use categories. Since Version 3, an anthropogenic heating diurnal cycle has been added as an option.

8.5.9 Building Environment Parameterization (BEP)

This is an urban option that also aims to account for more of the dynamical effects of buildings on the flow (Martilli et al., 2002). The option is available for the Noah and NoahMP LSMs. The buildings are allowed to directly impact more than the lowest model layer with suitable choices of PBL schemes (MYJ and Bougeault-Lacarrere). The scheme is also adaptable to more detailed urban morphology datasets such as NUDAPT and WUDAPT.

8.5.10 Building Energy Model (BEM)

An urban option that builds on BEP to include a building energy budget including heat transfer through walls, windows, floors, roofs, etc., and effects of air conditioning in controlled environments and other anthropogenic internal heating in addition to the external urban canyon representations that exist in other urban schemes (Salamanca and Martilli, 2010). This model allows for a prediction of energy consumption. This option is also available with the Noah and NoahMP LSMs.

8.5.11 Ocean Mixed-Layer Model

This can be selected as an independent option for water surfaces, and is designed for hurricane modeling in order to simulate the cooling of the ocean underneath hurricanes. The ocean mixed-layer model is based on that of Pollard et al. (1973). Each column is independently coupled to the local atmospheric column, so the model is one-dimensional. The ocean part consists of a time-varying layer, representing the variable-depth mixed layer over a fixed layer acting as a reservoir of cooler water with a specified thermal lapse rate. In the mixed layer, the prognostic variables are its depth, vector horizontal current, and mean temperature taken to be the sea-surface temperature (SST). The hurricane winds drive the current, which in turn leads to mixing at the base of the mixed layer when the Richardson number becomes low enough. This mixing deepens and cools the mixed layer, and hence the cooler sea-surface temperature impacts the heat and moisture fluxes at the surface, and has a negative feedback on hurricane intensity. The model includes Coriolis effects on the current, which are important in determining the location of maximum cooling on the right side of the hurricane track. It also includes a mixed-layer heat budget, but the surface fluxes and radiation have much less impact than the hurricane-induced deep mixing on the thermal balance at the time scales considered during a forecast. The ocean mixed-layer model is initialized using the observed SST for the mixed layer, and with a single depth representative of known conditions in the hurricane's vicinity that may be replaced with a map of the mixed-layer depth, if available. The initial current is set to zero, which is a reasonable assumption given that the hurricane-induced current is larger than pre-existing ones.

8.5.12 3-D Ocean Model

This is a three-dimensional ocean model with configurable layers (Price et al., 1994; Lee and Chen, 2012), but is simple in the sense of having a fixed flat bathymetry so that all the layers are at fixed depths. It applies to water surfaces and therefore can be used with any LSM. The model predicts temperature, salinity, and currents at each point along with advective effects. However, currents are typically initialized to zero and this model would require additional data to be initialized from real ocean data. Its main use is as added sophistication for a mixed layer model that responds to the atmosphere and includes three-dimensional dynamical ocean effects driven by the atmospheric stress which can improve over the one-dimensional approach.

8.5.13 CLM4.5 Lake Model

This is a standalone option in WRF that can be used with LSMs other than CLM4. It is based on Subin et al. (2012) and has a one-dimensional mass and energy balance scheme with 20-25 model layers, including up to 5 snow layers on the lake ice, 10 water layers, and 10 soil layers on the lake bottom. The lake scheme is used with actual lake points and lake depth data where available (WPS has a bathymetry dataset for many lakes), and it also can be used with user defined lake points and lake depth in WRF.

8.5.14 Sea-Ice Treatment

Most of the land models (CLM, Noah, NoahMP, RUC, PX) also consider sea-ice surfaces, and the model surface-layer schemes can also consider fractional sea-ice cover within a grid-cell where the fluxes are combined with those of open water. Usually the depth is considered fixed and the fraction may be updated with the sea-surface temperature periodically during the simulation as the model has no prognostic equation for sea-ice amounts. The sea ice in Noah and NoahMP considers 4 layers each 1 meter thick for the sea-ice energy budget.

8.5.15 Updating Lower Boundary Conditions

For long simulation periods, in excess of about a week, as in applications such as regional climate, ARW has a capability to specify lower boundary conditions on non-prognostic fields as a function of time. Foremost among these is the specification of the sea-surface temperature during the simulation. The Noah, RUC and PX LSMs also need to consider variations in vegetation fraction and albedo with season, so interpolated monthly data are read in with the lower boundary file. Sea-ice cover variation can also be specified by this method since Version 3. The lower boundary conditions are simply read in typically at the same frequency as the lateral boundary conditions, and the fields are updated with new current values at each read.

8.6 Planetary Boundary Layer

The planetary boundary layer (PBL) scheme is responsible for vertical sub-grid-scale fluxes due to eddy transports in the whole atmospheric column, not just the boundary layer. Thus, when a PBL scheme is activated, explicit vertical diffusion is de-activated with the assumption that the PBL scheme will handle this process. The most appropriate horizontal diffusion choices (Section 4.2.3) are those based on horizontal deformation or constant K_h values where horizontal and vertical mixing are treated independently. The surface fluxes are provided by the surface layer and land-surface schemes. The PBL schemes determine the flux profiles within the well-mixed boundary layer and the stable layer, and thus provide atmospheric tendencies of temperature, moisture (including clouds), and horizontal momentum in the entire atmospheric column. Most PBL schemes consider dry mixing, but can also include saturation effects in the vertical stability that determines the mixing. The schemes are one-dimensional, and assume that there is a clear scale separation between sub-grid eddies and resolved eddies. Also for schemes where TKE is prognostic it is independent between columns and not advected except for an option in the MYNN PBL. These columnwise independence assumptions of PBL schemes become less justifiable at grid sizes below a few hundred meters, where boundary layer eddies may start to be resolved, and in these situations the scheme should be replaced by a fully three-dimensional local sub-grid turbulence scheme such as the TKE diffusion scheme (Section 4.2.4.)

8.6.1 Yonsei University (YSU) PBL

The Yonsei University PBL (Hong et al., 2006) is the next generation of the MRF PBL, which also uses countergradient terms to represent fluxes due to non-local gradients. This scheme adds to the MRF PBL (Hong and Pan, 1996) an explicit treatment of the entrainment layer at the PBL top. The entrainment is made proportional to the surface buoyancy flux in line with results from studies with large-eddy models (Noh et al., 2003). The PBL top is defined using a critical bulk Richardson number of zero (compared to 0.5 in the MRF PBL), so is effectively dependent on the buoyancy profile, in which the PBL top is defined at the maximum entrainment layer (compared to the layer at which the diffusivity becomes zero). A smaller magnitude of the counter-gradient mixing in the YSU PBL produces a well-mixed boundary-layer profile, whereas there is a pronounced over-stable structure in the upper part of the mixed layer in the case of the MRF PBL. Details are available in Hong et al. (2006), including the analysis of the interaction between the boundary layer and precipitation physics.

Topographic drag effects were added as an option to this PBL scheme by Jimenez and Dudhia (2012) and improved by Lorente-Plazas et al. (2016) which modifies the model drag according to sub-grid variance in terrain elevation and also resolved local variability.

Top-down mixing was added as an option (Wilson and Fovell, 2018) to allow for radiative-driven downward mixing that helps the life-cycle of stratocumulus clouds and fog.

8.6.2 Mellor-Yamada-Janjic (MYJ) PBL

This parameterization of turbulence in the PBL and in the free atmosphere (Janjic, 1990, 1996, 2002) represents a nonsingular implementation of the Mellor-Yamada Level 2.5 turbulence closure model (Mellor and Yamada, 1982) through the full range of atmospheric turbulent regimes. In this implementation, an upper limit is imposed on the master length scale. This upper limit depends on the TKE as well as the buoyancy and shear of the driving flow. In the unstable range, the functional form of the upper limit is derived from the requirement that the TKE production be nonsingular in the case of growing turbulence. In the stable range, the upper limit is derived from the requirement that the ratio of the variance of the vertical velocity deviation and TKE cannot be smaller than that corresponding to the regime of vanishing turbulence. The TKE production/dissipation differential equation is solved iteratively. The empirical constants have been revised as well (Janjic, 1996, 2002). This scheme is also enabled with fluxes from layers other than the surface for use with the BEP and BEM urban models.

8.6.3 Quasi-Normal Scale Elimination (QNSE) scheme with EDMF

The QNSE scheme for the stable boundary is combined with an eddy-diffusivity mass-flux (EDMF) scheme for thermals in the unstable boundary layer. The QNSE scheme (Sukoriansky et al., 2005) is a theoretically derived scheme for the stably stratified boundary layer. The scheme is a Mellor-Yamada TKE-based method that modifies the vertical diffusion with a function of the

Richardson number to incorporate the theory. For unstable conditions an eddy-diffusivity mass flux approach has been adopted (Pergaud et al., 2009) that considers non-local thermals which may include cumulus clouds in additional to local TKE-based mixing. The shallow convective mass-flux scheme is called after the local TKE-based calculations in the QNSE scheme.

8.6.4 Mellor-Yamada-Nakanishi-Niino (MYNN) Levels 2.5 and 3

The MYNN2.5 and MYNN3 schemes (Nakanishi and Niino, 2006, 2009) are TKE-based schemes where Level 2.5 predicts TKE as an extra prognostic variable, while Level 3 adds variances of potential temperature, moisture and their covariance. However in both schemes only TKE is advected, but the TKE advection option is a unique aspect of this scheme. The scheme is used operationally as part of the NOAA HRRR physics and has included many newer updates including shallow convection and EDMF options (Olson et al., 2019) as well as updated options for computing mixing length scales. The schemes can be used with the MYNN or MM5 surface-layer schemes.

An additional option related to the MYNN PBL scheme is a wind-farm parameterization (Fitch et al., 2012) that accounts for the additional drag and turbulence generation by wind-farm rotors.The scheme is customizable to different rotor characteristics as a function of wind speed.

8.6.5 Asymmetrical Convective Model version 2 (ACM2) PBL

The ACM2 (Pleim, 2007) is a combination of the ACM, which is a simple transilient model that was originally a modification of the Blackadar convective model, and an eddy diffusion model. Thus, in convective conditions the ACM2 can simulate rapid upward transport in buoyant plumes and local shear induced turbulent diffusion. The partitioning between the local and non-local transport components is derived from the fraction of non-local heat flux according to the model of Holtslag and Boville (1993). The algorithm transitions smoothly from eddy diffusion in stable conditions to the combined local and non-local transport in unstable conditions. The ACM2 is particularly well suited for consistent PBL transport of any atmospheric quantity including both meteorological (u, v,θ , qv) and chemical trace species.

8.6.6 Bougeault-Lacarrere PBL

The BouLac PBL (Bougeault and Lacarrere, 1989) is a 1.5-order (level 2.5) scheme with a prognostic TKE equation and a method of calculating length scales that defines both upwards and downwards lengths scales affected by the PBL top and ground and uses the lesser of these for a length scale. The scheme has also been adapted for use with the BEP and BEM urban models that can represent buildings higher than the lowest model level thickness.

8.6.7 University of Washington (UW) PBL

The scheme of Bretherton and Park (2009) is part of the CAM climate model physics suite. It is a TKE-based scheme that includes a moist turbulence parameterization. The TKE is a diagnostic quantity. The scheme defines convectively mixed sets of layers and includes a method for explicit entrainment related to the convective velocity.

8.6.8 Total Energy Mass Flux (TEMF) PBL

Angevine et al. (2010) use total energy rather than TKE as a prognostic variable in each column. This includes potential energy and kinetic energy to give total energy as a prognostic variable. The scheme includes the effects of shallow cumulus convection and is also coupled with its own surface-layer scheme.

8.6.9 Shin-Hong PBL

Shin and Hong (2015) have developed a scale-aware PBL option based on the YSU PBL scheme. At larger grid sizes it resembles YSU, but as the grid size becomes much less than the PBL depth, the nonlocal term is reduced in strength to allow the resolved scales to do a fraction of the transport consistent with resolution.

8.6.10 Grenier-Bretherton-McCaa (GBM) PBL

This is a moist PBL scheme Grenier and Bretherton (2001) that can also represent cloud-topped boundary layers such as marine stratocumulus. The scheme includes a TKE equation and the effect of cloud-top radiative cooling that modifies the entrainment and TKE, an important process for stratocumulus clouds.

8.6.11 Medium Range Forecast Model (MRF) PBL

The scheme is described by Hong and Pan (1996). This PBL scheme employs a so-called counter-gradient flux for heat and moisture in unstable conditions. It uses enhanced vertical flux coefficients in the PBL, and the PBL height is determined from a critical bulk Richardson number. It handles vertical diffusion with an implicit local scheme, and it is based on local Ri in the free atmosphere.

8.6.12 3DTKE PBL

This scheme is a scale-aware, three-dimensional TKE subgrid mixing scheme (Zhang et al., 2018). It extends the original 1.5-order TKE-closure subgrid model from LES (km_opt = 2) to mesoscale. In the LES limit, this option is the same as km_opt = 2. Going towards the mesoscale limit, the horizontal diffusion transitions to the first-order 2D Smagorinsky and a strengthening non-local term, following Shin-Hong, is added to the vertical diffusion, which is also made implicit to allow for longer time steps and thin model layers.

8.6.13 E-ϵ PBL

This scheme (Zhang et al., 2020) predicts TKE (E) as well as TKE dissipation rate (ϵ) with a 1.5-order closure. It follows Langland et al. (1996) with some modification and improvements.

It uses different coefficients for the epsilon equation. The scheme chooses maximum of shear production versus the sum of shear and buoyancy productions in the epsilon equation to avoid oscillation, and enhances the buoyancy term in both equations when clouds are present. It also includes TKE dissipative rate as an additional heat source. A nonlocal term is considered for potential temperature and moisture in vertical mixing.

8.6.14 Gravity Wave Drag

For grid sizes that exceed about 10 km and for longer simulations that include significant orography, gravity wave drag may be an important process to include. This accounts for the momentum flux due to unresolved mountain waves that may affect jet-stream level winds, and mountains also have a low-level flow-blocking effect. WRF has an option for these effects (Choi and Hong, 2015) that uses sub-grid orographic data provided by *geogrid*. The sub-grid information includes direction-sensitive statistics related to the orientation of the orography.

8.6.15 GSL Gravity Wave Drag

This is an extended and scale-aware gravity-wave drag scheme developed by Global Systems Laboratory NOAA. In addition to the traditional gravity wave drag effect due to unresolved topography and low-level blocking that remain similar to the older scheme, this scheme has two parameterizations for grid sizes down to 1 km. One of these is the turbulent orographic form drag based on Beljaars et al. (2004), due to pressure perturbations and shape of the orography (note that this is not gravity wave drag despite being included in this option). The other parameterization is for small-scale gravity wave drag in the stable PBL (Tsiringakis et al., 2017) which allows vertical propagation of gravity waves at smaller scales. The scheme also considers ramping down the large scale gravity wave drag as the grid sizes decrease to 5 km, and the smaller scale drags are turned off at 1 km. This option uses a different set of sub-grid orographic data based on GMTED provided by *geogrid*.

8.7 Atmospheric Radiation

The radiation schemes provide atmospheric temperature tendencies due to radiative flux divergence and surface downward longwave and shortwave radiation for the ground heat budget. Longwave radiation includes infrared or thermal radiation absorbed and emitted by gases and surfaces. Upward longwave radiative flux from the ground is determined by the surface emissivity that in turn depends upon land-use type, as well as the ground (skin) temperature. Shortwave radiation includes visible and surrounding wavelengths that make up the solar spectrum. Hence, the only source is the Sun, but processes include absorption, reflection, and scattering in the atmosphere and at surfaces. For shortwave radiation, the upward flux is the reflection due to surface albedo. For higher resolutions, the shortwave schemes can represent slope effects that modify the surface downward shortwave flux according to slope aspect angles. There are also diagnostic outputs of the diffuse and direct components of solar radiation at the surface. Diagnostics for the RRTMG and CAM3 options also include TOA/surface, longwave/shortwave, clearsky/allsky, upward/downward accumulated fluxes for radiation budgets.

Within the atmosphere the radiation responds to model-predicted cloud and water vapor distributions, (diagnostic) cloud fraction, as well as specified carbon dioxide, ozone, and (optionally) trace gas concentrations. Some schemes can handle aerosols. All the radiation schemes in WRF currently are column (one-dimensional) schemes, so each column is treated independently, and the fluxes correspond to those in infinite horizontally uniform planes with cloud fractions at leach layer, which is a good approximation if the vertical thickness of the model layers is much less than the horizontal grid length. This assumption would become less accurate at high horizontal resolution.

In addition to radiative transfer schemes listed below, WRF also has idealized temperature relaxation methods for the Held-Suarez global test case and the idealized tropical cyclone case.

8.7.1 Rapid Radiative Transfer Model (RRTM) Longwave

This RRTM, which is taken from MM5, is based on Mlawer et al. (1997) and is a spectral-band scheme using the correlated-k method. It uses pre-set tables to accurately represent longwave processes due to water vapor, ozone, CO_2, and trace gases (if present), as well as accounting for cloud optical depth.

8.7.2 CAM3 Longwave and Shortwave

These are spectral-band longwave and shortwave schemes used in the NCAR Community Atmosphere Model (CAM 3.0) for climate simulations. It has the potential to handle several trace gases including time variation as in climate-change scenarios. It interacts with resolved clouds and cloud fractions, and is documented fully by Collins et al. (2004). It has the ability to handle optical properties of several aerosol types and trace gases. It uses cloud fractions and overlap assumptions in unsaturated regions, and has a monthly zonal ozone climatology.

Note that in more recent versions of CAM, currently used in CESM, this scheme has been replaced by RRTMG radiation.

8.7.3 RRTMG Longwave and Shortwave

The Rapid Radiative Transfer Model for GCMs (RRTMG, Iacono et al. (2008)) is a state-of-the-art widely used radiative model for weather and climate applications both globally and regionally. The schemes use spectral bands and the k-distribution method of integration with look-up tables for efficiency. For clouds with cloud fractions that vary vertically it uses the Monte Carlo Independent Column Approximation (MCICA) together with a maximum-random overlap assumption by default (random, maximum, exponential and expotential-random methods are also available). It can also make use of effective radii of cloud water, ice and snow if they come from the microphysics or it will use its own assumptions if these are not provided. It includes the effect of trace gases and has an option for their time variation for climate projections. For ozone there is a global monthly climatology option that comes from the CAM3 data. Aerosols can use a global monthly climatology (Tegen or Eidhammer/Thompson) or can come from optical properties computed by WRF-Chem or can be specified/input in other ways. The longwave scheme has been modified at the top-of-atmosphere to account for the significant downward flux originating from above the model top (Cavallo et al., 2011).

8.7.4 RRTMG-K Longwave and Shortwave

A version of RRTMG provided by KIAPS (Korea) that is optimized and improved in several ways as detailed by Baek (2017). The scheme optimizes the MCICA cloud column calculations using a method called G-Packed MCICA that reduces the number of random samples and uses the same ones for both longwave and shortwave. Several improvements have also been made to the shortwave scheme that uses a revised two-stream approximation and reduces errors by adjusting the scattering of microphysical and aerosol particles.

8.7.5 Eta Geophysical Fluid Dynamics Laboratory (GFDL) Longwave and Shortwave

This longwave radiation scheme is from GFDL. It follows the simplified exchange method of Fels and Schwarzkopf (1975) and Schwarzkopf and Fels (1991), with calculation over spectral bands associated with carbon dioxide, water vapor, and ozone. Included are Schwarzkopf and Fels (1985) transmission coefficients for carbon dioxide, a Roberts et al. (1976) water vapor continuum, and the effects of water vapor-carbon dioxide overlap and of a Voigt line-shape correction. The Rodgers (1968) formulation is adopted for ozone absorption. Clouds are randomly overlapped. This scheme is implemented to conduct comparisons with the operational Eta model.

The shortwave radiation is a GFDL version of the Lacis and Hansen (1974) parameterization. Effects of atmospheric water vapor, ozone (both from Lacis and Hansen, 1974), and carbon dioxide (Sasamori et al., 1972) are employed. Clouds are randomly overlapped. Shortwave calculations are made using a daylight-mean cosine solar zenith angle over the time interval (given by the radiation call frequency).

8.7.6 MM5 (Dudhia) Shortwave

This scheme is based on Dudhia (1989) and is taken from MM5. It has a simple downward integration of solar flux, accounting for tunable clear-air scattering, as well as water vapor absorption (Lacis and Hansen, 1974), and cloud albedo and absorption. It uses look-up tables for clouds from Stephens (1978) but does not use sub-grid cloud fractions, only uniformly clear or cloudy within a model layer. The scheme has no ozone, so it should not be used with model tops in the mid-stratosphere.

8.7.7 Old Goddard Shortwave

This scheme is based on Chou and Suarez (1994). It has a total of 11 spectral bands and considers diffuse and direct solar radiation components in a two-stream approach that accounts for scattered and reflected components. Ozone is considered with several climatological one-dimensional profiles available. The scheme can also take aerosol optical properties provided by WRF-Chem.

8.7.8 New Goddard Longwave and Shortwave

These spectral-band schemes provided by NASA Goddard are advanced and relatively efficient while also being accurate. The shortwave and longwave schemes are based on Chou and Suarez (1999) and Chou et al. (2001) respectively. It does not interact with WRF-Chem but 2D aerosol optical depth information can be used for aerosol effects. It includes trace gases and uses ozone climatology profiles. Cloud fractions in layers are also accounted for with low, middle and high layers maximally overlapped within these grouped layers and randomly between them. The newest version of the Goddard radiation scheme (Matsui et al., 2018) involves three major improvements. First, a size-, shape-, and radiation-spectrum-consistent single scattering database (Yang et al., 2013) has been incorporated to represent hydrometeor-consistent optical properties (including rain, snow, graupel, and hail). Second, the molecular absorption database has been updated from HITRAN1996 to HITRAN2012, which reduces the biases for clear-sky radiation flux. Third, the radiation code has been vectorized for improved computational efficiency.

8.7.9 Fu-Liou-Gu (FLG) Longwave and Shortwave

These are spectral band schemes provided by UCLA (Gu et al., 2011; Fu and Liou, 1992) that also contain capabilities for fractional clouds and aerosols, but these are off by default, so clouds are either present or absent in a layer. Ozone uses profiles similar to the Goddard schemes. CO2 and trace gases are specified. A correlated-k distribution method is used for the longwave scheme.

8.8 Physics Interactions

While the model physics parameterizations are categorized in a modular way, it should be noted that there are many interactions between them via the model state variables (potential temperature, moisture, wind, etc.) and their tendencies, and via the surface fluxes, as shown in Fig.8.1. Table 8.1 summarizes how the various physics processes interact in the model. In the table, *i* indicates that the state variable or flux is required input for the physics scheme, and *o* indicates that the tendency or flux is a probable output of the scheme. It can be seen that all the physical schemes interact in some way with the surface physics (land-surface models, and, potentially, coupled ocean models). The surface physics, while not explicitly producing tendencies of atmospheric state variables, is responsible for updating the land-state variables.

Note also that, as mentioned, the microphysics does not output tendencies, but updates the atmospheric state at the end of the model time-step. Unlike for other physics, there is no option in ARW to call microphysics at lower frequencies than the model time step mainly because of its important saturation adjustment function that interacts with the dynamics especially in rseolved convection. However, the rest of the *o*'s in the upper half of the table are representative of the physical tendencies of these variables in the model.

The radiation, boundary-layer and cumulus parameterization schemes all output tendencies, but the tendencies are not added until later in the solver where their sum contributes to the forcing for the dynamics, so from this perspective the order of call is not important. Moreover, these physics schemes do not have to be called at the same frequency as each other or the model

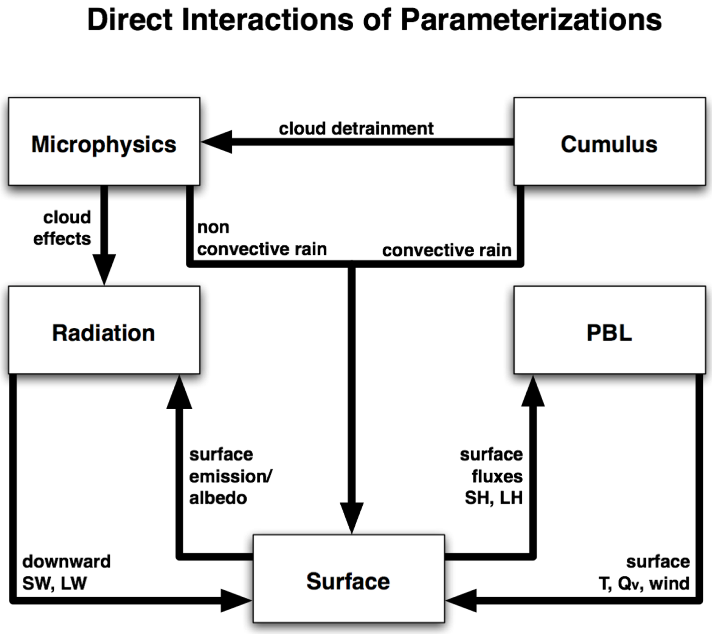

Figure 8.1: Diagram showing interactions between various physics components.

Table 8.1: Physics Interactions. Columns correspond to model physical processes: radiation (Rad), microphysics (MP), cumulus parameterization (CP), planetary boundary layer/vertical diffusion (PBL), and surface physics (Sfc). Rows corresponds to model variables where *i* and *o* indicate whether a variable is input or output (updated) by a physical process.

		Rad	MP	CP	PBL	Sfc
Atmospheric State or Tendencies	Momentum			io	io	
	Pot. Temp.	io	io	io	io	
	Water Vapor	i	io	io	io	
	Cloud	i	io	o	io	
	Precip	i	io	o		
Surface Fluxes	Longwave Up	i				o
	Longwave Down	o				i
	Shortwave Up	i				o
	Shortwave Down	o				i
	Sfc Convective Rain			o		i
	Sfc Resolved Rain		o			i
	Heat Flux				i	o
	Moisture Flux				i	o
	Surface Stress				i	o

time step. When lower frequencies are used, their tendencies are kept constant between calls. This is typically done for the radiation schemes, which are too expensive to call every timestep, and often for the cumulus schemes, for which it may only be necessary to update the convective columns every five minutes or so. However, the surface/boundary-layer schemes are normally called every step in ARW because this is likely to give the best results, but the option is available to use a less frequent call that may be useful for the more expensive CLM4 LSM.

The radiation is called first because of the required radiative fluxes that are input to the land-surface scheme. The land-surface also requires rainfall from the microphysics and cumulus schemes, but that is from the previous time-step since it is called before the cumulus scheme and the microphysics is at the end of the time-step. The boundary-layer scheme is necessarily after the land-surface scheme because it requires the heat and moisture fluxes. Some cumulus schemes (Grell options) also use the boundary-layer tendencies.

Chapter 9

Stochastic Parameterization Suite

Physical parameterization schemes represent averages over unresolved, subgrid-scale processes, and those averages necessarily fluctuate depending on the precise realization of subgrid-scale fields. Hence, physical parameterization schemes should include a random, “stochastic” component. To represent this random contribution to forecast error, ensemble prediction systems now routinely use stochastic parameterization schemes. Stochastic parameterization schemes have been shown to improve the probabilistic skill of weather forecasts on short- and medium-length forecast timescales (e.g. Berner et al., 2009, 2011; Leutbecher et al., 2017). Less known, however, is the fact that stochastic parameterization schemes also have the potential to reduce systematic model error (e.g. Berner et al., 2017).

The stochastic parameterization suite in WRF comprises a number of stochastic parameterization schemes, targeted at representing different aspects of uncertainty (see Table 9.1). Generally, one or more random perturbation fields are generated and used to perturb tendencies or parameters in the physical parameterization schemes. The random perturbation fields are characterized by spatial and temporal correlations as well as an overall perturbation amplitude, which can be prescribed by namelist parameters. Figure 9.1 provides an example for perturbation patterns with different spatial length-scales.

The benefits of stochastic parameterization schemes are most evident in ensemble prediction systems, where the added ensemble diversity leads to more reliable ensemble spread and improved probabilistic forecast skill (e.g. Berner et al., 2015).

Table 9.1: Stochastic parameterization suite

Scheme	Name	Perturbations to
SPPT	Stochastically perturbed parameterization tendencies	u-,v-,θ- and q_v-tendencies from PBL and convection scheme
SKEBS	Stochastic kinetic-energy backscatter scheme	Full (= physics + dynamics) u_{rot}-,v_{rot}- and θ- tendencies
SPP	Stochastically perturbed parameterization scheme	Select parameters from PBL and convective scheme
RPF	Random perturbation field	Creates perturbation pattern only; interface must be provided by user

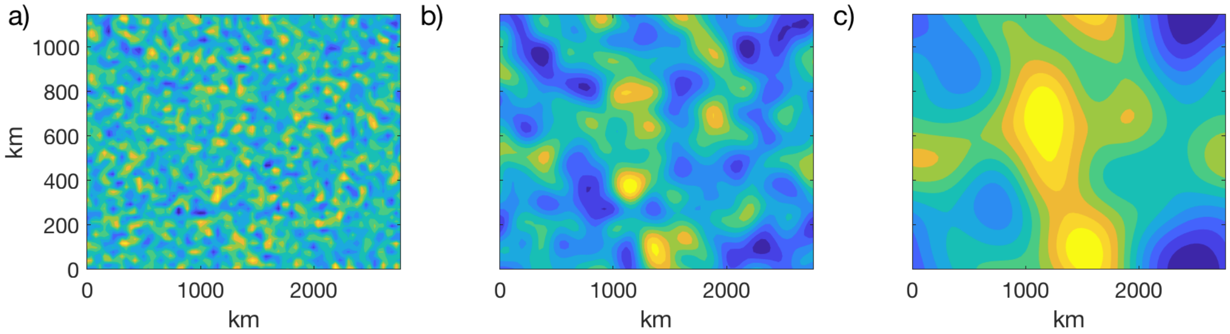

Figure 9.1: Perturbation patterns for three different spatial scales: a) convection-scale, b) mesoscale, c) synoptic scale.

9.1 Stochastically Perturbed Physics Tendencies (SPPT)

The Stochastically Perturbed Parameterization Tendency scheme (SPPT) is based on the assumption that there is uncertainty in the parameterized physics tendencies and that this uncertainty is proportional to the net physics tendency (Buizza et al., 1999; Palmer et al., 2009). Consequently, SPPT perturbs the net physical tendency of temperature, humidity, and the wind components at each time step with a multiplicative random coefficient:

$$\frac{\partial X}{\partial t} = D + (1 + r) \sum_i P_i \, . \tag{9.1}$$

Here, $\partial X/\partial t$ denotes the total tendency in variable X, D is the tendency from the dynamical core, P_i the tendency from the i-th physics scheme, and r is a two-dimensional, Gaussian distributed zero-mean random perturbation field with spatial and temporal correlations (as in Fig.**??**). Depending on the implementation, the SPPT scheme can use up to three patterns with different spatial and time scales, as well as a vertical tapering function which tapers perturbations near the surface and for the highest model levels. The WRF implementation by default uses only a single perturbation field (Berner et al., 2015), and it perturbs the tendencies from the PBL and convection schemes, but not those from the radiation or microphysics schemes. For multiple domains, the perturbation pattern of the parent domain is interpolated to the nested domains.

9.2 Stochastic Kinetic-Energy Backscatter Scheme (SKEBS)

The Stochastic Kinetic Energy Backscatter scheme (SKEBS) aims to represent the interactions of turbulent eddies near or below the truncation level with the resolved state. Some of the eddy-eddy interactions will dissipate, but others will lead to a resolved-scale effect. Originally developed for large-eddy simulation applications, these ideas were adapted for numerical weather prediction by Shutts (2005) and Berner et al. (2009). SKEBS generates streamfunction perturbations with spatio-temporal correlations, which perturb the rotational wind. These can be weighted with the dissipation rate from numerical diffusion, convection, and orographic wave drag. In the WRF implementation, no dissipation weighting is used and the perturbations are extended to the potential temperature field (Berner et al., 2011). Wind component perturbations are proportional to the square root of the kinetic-energy backscatter rate, and temperature perturbations are proportional to the potential energy backscatter rate.

A comparison of SKEBS and SPPT shows that SKEBS introduces the most model diversity in the free atmosphere and for dynamical variables, while SPPT is most active in regions with large tendencies (e.g., in areas with convection and near the surface) (Berner et al., 2015).

9.3 Stochastically Perturbed Parameterization Scheme (SPP)

To describe the statistics of the unresolved, subgrid-scale processes, physical parameterization schemes have a number of deterministic parameters. While some of these have no uncertainty (e.g., the gravitational constant), others have large uncertainties due to measurement errors and heterogeneities in the underlying physical process. Examples are the processes represented by the parameter "roughness length" in the PBL scheme or the shape parameter characterizing the particle size distribution in many microphysics schemes.

The stochastically perturbed parameterization scheme (SPP) perturbs the values of uncertain key parameters and thus provides a way to represent uncertainties within a particular parameterization scheme (Bowler et al., 2008; Hacker et al., 2011). Perturbations in the convection scheme (e.g., to the vertical mass flux profile) or in the microphysics scheme (e.g., to the shape parameter of the particle size distribution) in principle allow the representation of structural model error. The statistical sciences fundamentally distinguish between "parameter error" and "structural error". This distinction is blurred when some parameters in the physical schemes are perturbed, since parameter changes can change the structural model error. Hence the scheme is referred to as "Stochastically perturbed *parameterization* scheme" rather than "Stochastically perturbed *parameter* scheme".

The SPP released in WRF has been designed in close collaboration with developers of physical parameterization and is under active development. Hence, it is only available for selected physics packages, namely the Grell-Freitas convection scheme and the MYNN PBL scheme (Jankov et al., 2017).

The perturbations introduced by SPP tend to be smaller than those introduced by SKEBS and SPPT and are by themselves typically not enough to generate reliable ensemble spread (Berner et al., 2015). However, SPP can be used to study forecast sensitivity to a particular parameter setting and/or can be augmented by one of the other model-error schemes.

9.4 Random Perturbation field (RPT)

WRF enables the user to generate a 3-D Gaussian random perturbation field with prescribed spatial and temporal correlations and use to it perturb parameters or variables of interest. The interface to the perturbed quantity has to be provided by the user.

9.5 Stochastic Perturbations to the Lateral Boundary Conditions

The stochastic tendencies in WRF are typically treated as physics tendencies, and they change the perturbed fields at each time step within the WRF domain. However, since the stochastic perturbation field is also generated on the boundary, it can be used to perturb the lateral boundary specified and relaxation zones.

Chapter 10

Nudging

Nudging, also known as four-dimensional data assimilation (FDDA), is a method of keeping simulations close to analyses and/or observations or forcing data over the course of an integration by applying extra forcing terms to the model equations. There are three types of nudging and some can be used in combination. Grid- or analysis-nudging simply forces the model simulation towards a series of analyses grid-point by grid-point. Observational- or station-nudging locally forces the simulation towards observational data. Spectral nudging only forces the model to the selected spectra of waves in the analysis. These methods provide a four-dimensional analysis that is somewhat balanced dynamically, and in terms of continuity, while allowing for complex local topographical or convective variations. Such datasets can cover long periods, and have particular value in driving off-line air quality or atmospheric chemistry models.

10.1 Grid Nudging or Analysis Nudging

The grid-nudging method is specifically three-dimensional analysis nudging, whereby the atmospheric model is nudged towards time- and space-interpolated analyses using a point-by-point relaxation term. The method can be used to nudge wind component u and v, temperature and water vapor mixing ratio. Stauffer and Seaman (1990) originally developed the technique for MM5.

The grid-nudging technique has several major uses.

a) Four-dimensional datasets. The model is run with grid-nudging for long periods, e.g. months, to provide a four-dimensional meteorologically self-consistent dataset that also stays on track with the driving analyses. In this way, the model is used as an intelligent interpolator of analyses between times, and also accounting better for topographic and convective effects. As mentioned, the primary use for such datasets is in air quality where the wind fields may be used to drive off-line chemistry models.

b) Boundary conditions. A nested simulation is run with the outer domain nudged towards analyses, and the nest running un-nudged. This provides better temporal detail at the nest boundary than driving it directly from linearly interpolated analyses, as it would be if it were the outer domain. This technique could also be used in forecasting, where an outer domain is nudged towards global forecast fields that are available in advance of the regional forecast.

c) Dynamic initialization. A pre-forecast period (e.g., -6 hours to 0 hours) is run with nudging using analyses at those times that are already available. This is probably better than a cold-start using just the 0 hour analysis because it gives the model a chance to spin up. In particular, the model will have six hours to adjust to topography, and produce cloud fields by hour 0, whereas with a cold start there would be a spin-up phase where waves are produced and clouds are developed. This method could also be combined with 3D-Var techniques that may provide the hour 0 analysis.

Grid nudging has been added to ARW using the same input analyses as the WPS preprocessing systems can provide. Since it works on multiple domains in a nesting configuration, it requires multiple time-periods of each nudged domain as input analyses. Given these analyses, the *real* program produces another input file which is read by the model as nudging is performed. This file contains the gridded analysis 3d fields of the times bracketing the current model time as the forecast proceeds. The four nudged fields are the two horizontal wind components (u and v), temperature, and specific humidity.

The method is implemented through an extra tendency term in the nudged variable's equations, e.g.

$$\frac{\partial \theta}{\partial t} = F(\theta) + G_\theta W_\theta (\hat{\theta}_0 - \theta)$$

where $F(\theta)$ represents the normal tendency terms due to physics, advection, etc., G_θ is a timescale controlling the nudging strength, and W_θ is an additional weight in time or space to limit the nudging as described more below, while $\hat{\theta}_0$ is the time- and space-interpolated analysis field value towards which the nudging relaxes the solution.

Several options are available to control the nudging.

a) Nudging end-time and ramping. Nudging can be turned off during the simulation, as in dynamical initialization. Since turning nudging off suddenly can lead to noise, there is a capability for ramping the nudging down over a period, typically 1-2 hours to reduce the shock.

b) Strength of nudging. The timescale for nudging can be controlled individually for winds, temperature and moisture. Typically the namelist value of 0.0003 s-1 is used, corresponding to a timescale of about 1 hour, but this may be reduced for moisture where there may be less confidence in the analysis versus the details in the model.

c) Nudging in the boundary layer. Sometimes, since the analysis does not resolve the diurnal cycle, it is better not to nudge in the boundary layer to let the model PBL evolve properly, particularly the temperature and moisture fields. Each variable can therefore be selectively not nudged in the model boundary layer, the depth of which is given by the PBL physics.

d) Nudging at low levels. Alternatively the nudging can be deactivated for any of the variables below a certain layer throughout the simulation. For example, the lowest ten layers can be free of the nudging term.

e) Nudging and nesting. Each of these controls is independently set for each domain when nesting, except for the ramping function, which has one switch for all domains.

10.2 Surface Analysis Nudging

The method used in surface analysis nudging is similar to that for 3-dimensional analysis nudging, except it only applies to the variables in the boundary layer. It utilizes a surface analysis file produced by an auxiliary program which may have higher temporal frequency than the 3-dimensional atmospherice analysis.

10.3 Flux-Adjusting Surface Analysis Nudging

This is a surface analysis nudging method that not only nudges temperature and water mixing ratio at the first model level, but it also corrects soil temperature and moisture based on the differences in temperature and water vapor mixing ratio at the first model level (also refered to as Flux-Adjusting Surface Data Assimilation System or FASDAS). The differences of temperature and water vapor mixing ratio at the first model level are converted to surface flux adjustments that are applied to the prognostic equations of soil temperature and soil moisture. Through this indirect nudging, the surface temperature and water vapor mixing ratio from the model will become closer to the analysis. This method was developed for MM5 by Alapaty et al. (2008).

10.4 Observational or Station Nudging

The observation-nudging capability allows the model to effectively assimilate temperature, wind and moisture observations from all platforms, measured at any location within the model domains and any time within a given data assimilation periods. With the observation-nudging formulation, each observation directly interacts with the model equations and thus the scheme yields dynamically and diabatically initialized analyses to support the applications that need regional 4-D full-field weather and/or to start regional NWP with spun-up initial conditions. The observation-nudging scheme, which is an enhanced version of the standard MM5 observation-nudging scheme, was originally implemented into ARW in Version 2.2 with additional enhancements applied in later versions. More details of the methods can be found in Liu et al. (2008) and Deng et al. (2009), though not all of the modifications are included in the standard release.

Similar to analysis nudging, observation nudging is applied via an additional tendency term:

$$\frac{\partial a\mu_d}{\partial t}\left(x,y,z,t\right) = F_a\left(x,y,z,t\right) + \mu_d G_a \frac{\sum\limits_{i=1}^{N} W_a^2\left(i,x,y,z,t\right)\left[a_o\left(i\right) - a_m\left(x_i,y_i,z_i,t\right)\right]}{\sum\limits_{i=1}^{N} W_a\left(i,x,y,z,t\right)}$$

where a is the quantity being nudged (which can be water vapor mixing ratio, potential temperature, u wind component, or v wind component), μ_d is the mass of the dry air in the column, F_a represents the physical tendency terms for a, G_a is the nudging strength for a, N is the total number of observations, i is the index to the current observation, W_a is the spatiotemporal weighting function based on the temporal and spatial separation between the observation (located at (x_i, y_i, z_i, t_i)) and the current model location (x, y, z, t), a_o is the observed value of a, and $a_m(x_i, y_i, z_i, t)$ is the model value of a interpolated to the observation location. The innovation $(a_o - a_m)$ for a given observation is calculated once at each time the nudging tendency term is updated and that innovation is then spread spatially. The nudging strength G_a is the inverse of the e-folding time of the innovation (assuming that the physical tendency terms $[F_a]$ were all zero and thus the observation nudging was the only factor modifying the variable a). Note that while ARW reads in temperature observations it converts them to potential temperature for application in observation nudging. Also, surface temperature and surface wind observations are adjusted to the lowest prognostic level for calculation of the innovation.

The user specifies the time period within the model integration over which observation nudging will be applied. The user also specifies whether the strength at which the nudging is applied ramps down linearly with time at the end of the observation nudging period. Within the time period the user specifies for application of observation nudging, individual observations are applied over a time window of user-specified length centered on the time of the observation. Full weighting is applied over the half of the window centered at the observation time, and weighting ramps linearly with time in the quarters of the time window on either end of the time window. A different time-length can be specified for surface observations than other observations.

Vertically, innovations from surface observations are spread based on user settings and can be dependent on the depth of the PBL and the current PBL regime. Innovations from multi-level observations are vertically interpolated in pressure to model levels. For single-level above-surface observations the innovation is applied from 75 hPa below the observation to 75 hPa above the observation with weights linearly decreasing with the difference in pressure between the observation and the level at which the innovation is being applied. Single-level above-surface observations above (below) the PBL will not be spread below (above) the PBL since errors within the PBL may not be well-correlated with errors above the PBL. The user can also choose to prevent any nudging of any observations from being applied within the PBL.

Horizontally, innovations from surface observations are spread along the surface, whereas innovations from above-surface observations are spread in pressure space (the vertical spreading described above is applied wherever the innovations are horizontally spread). The user specifies the horizontal radius of influence for above-surface observations and specifies a factor that this will be multiplied by to determine the radius of influence for surface observations. The weighting of the innovation decreases non-linearly with distance from the observation within the radius of influence. The horizontal radius of influence for above-surface observations increases with decreasing pressure up until reaching double the specified radius of influence at 500 hPa. An innovation from a single-level above-surface observation above (below) the PBL will not be spread horizontally to locations where it would be below (above) the PBL since errors within the PBL may not be well-correlated with errors above the PBL. Since innovations calculated in a valley may not be representative of the error on a mountain top, the weighting for surface observations is decreased based on the difference between the surface pressure at the location of the observation and at the location the innovation is being applied.

More details regarding observation nudging in ARW can be found in a brief guide on this topic (http://www2.mmm.ucar.edu/wrf/users/docs/ObsNudgingGuide.pdf).

10.5 Spectral Nudging

Spectral nudging is another way to nudge the model solution to either analysis or any forcing data. The key difference between this method and that of grid- or obs-nudging is that it is more selective in the scales one would like to nudge. In contrast to directly nudge model variables toward analysis or observation, this method decomposes the difference fields spectrally, and nudges toward the longer waves that correspond to the analysis. The spectral coefficients from the selected waves are then transformed back from the wave space to physical space and added to the model as tendencies. This technique was originally implemented by Miguez-Macho et al. (2004) to the Reginoal Atmospheric Modeling System, and later to ARW in 2010.

Spectral nudging uses the same input data as for grid-nudging, and nudges model variables u, v, temperature, and geopotential height. Water mixing ratio nudging was added in Version 4.0. Applications described above for grid-nudging can be considered using spectral nudging too.

Options to control the grid-nudging are also used for spectral nudging (such as nudging end time and ramping, nudging strength, controls of nudging in the boundary layer or lower levels and so on). In addition, there is an option to control the ramping in the vertical between the layer without nudging to the layer where the nudging is on. The number of waves to nudge in the x and y directions are user-defined.

Chapter 11

Data Assimilation

An introduction to the basic ideas of variational data assimilation and the WRF Data Assimilation (WRFDA) system (Barker et al., 2012) is given in this chapter, followed by a brief overview of recent major improvements to WRFDA. This overview supplements the original description of the three-dimensional variational (3D-Var) algorithm found in Barker et al. (2004) with several important additions and modifications, including a utility *gen_be* for calculating background error covariances, several new data assimilation algorithms, and new and improved capabilities to assimilate satellite radiance and radar observations.

11.1 Introduction

The basic goal of any variational data assimilation system is to produce an optimal estimate of the true atmospheric state at analysis time through iterative solution of a prescribed cost-function (Ide et al., 1997):

$$J(\mathbf{x}) = J_b(\mathbf{x}) + J_o(\mathbf{x}) = \frac{1}{2}(\mathbf{x} - \mathbf{x}^b)^T \mathbf{B}^{-1} (\mathbf{x} - \mathbf{x}^b) + \frac{1}{2}(\mathbf{y} - \mathbf{y}^o)^T (\mathbf{E} + \mathbf{F})^{-1} (\mathbf{y} - \mathbf{y}^o). \tag{11.1}$$

The variational problem can be summarized as the iterative minimization of (11.1) to find the analysis state $\mathbf{x}$ that minimizes $J(\mathbf{x})$. This solution represents the *a posteriori* maximum likelihood (minimum variance) estimate of the true state of the atmosphere given the two sources of *a priori* data: the first guess (or background) $\mathbf{x^b}$ and observations $\mathbf{y^o}$ (Lorenc, 1986). The fit to individual data points is weighted by estimates of their errors: $\mathbf{B}$, $\mathbf{E}$, and $\mathbf{F}$ are the background, observation (instrumental), and representative error covariance matrices, respectively. The representative error is an estimate of inaccuracies introduced via the observation operator H used to transform the gridded analysis $\mathbf{x}$ to observation space $\mathbf{y} = H(\mathbf{x})$ for comparison against observations. This error will be resolution dependent and may also include a contribution from approximations (e.g., linearizations) in H.

As described in Barker et al. (2004), the particular variational data assimilation algorithm adopted in WRFDA is a model-space, incremental formulation of the variational problem. In this approach, observations, previous forecasts, their errors, and physical laws are combined to produce analysis increments $\mathbf{x^{a'}}$, which are added to the first guess $\mathbf{x^b}$ to provide an updated analysis.

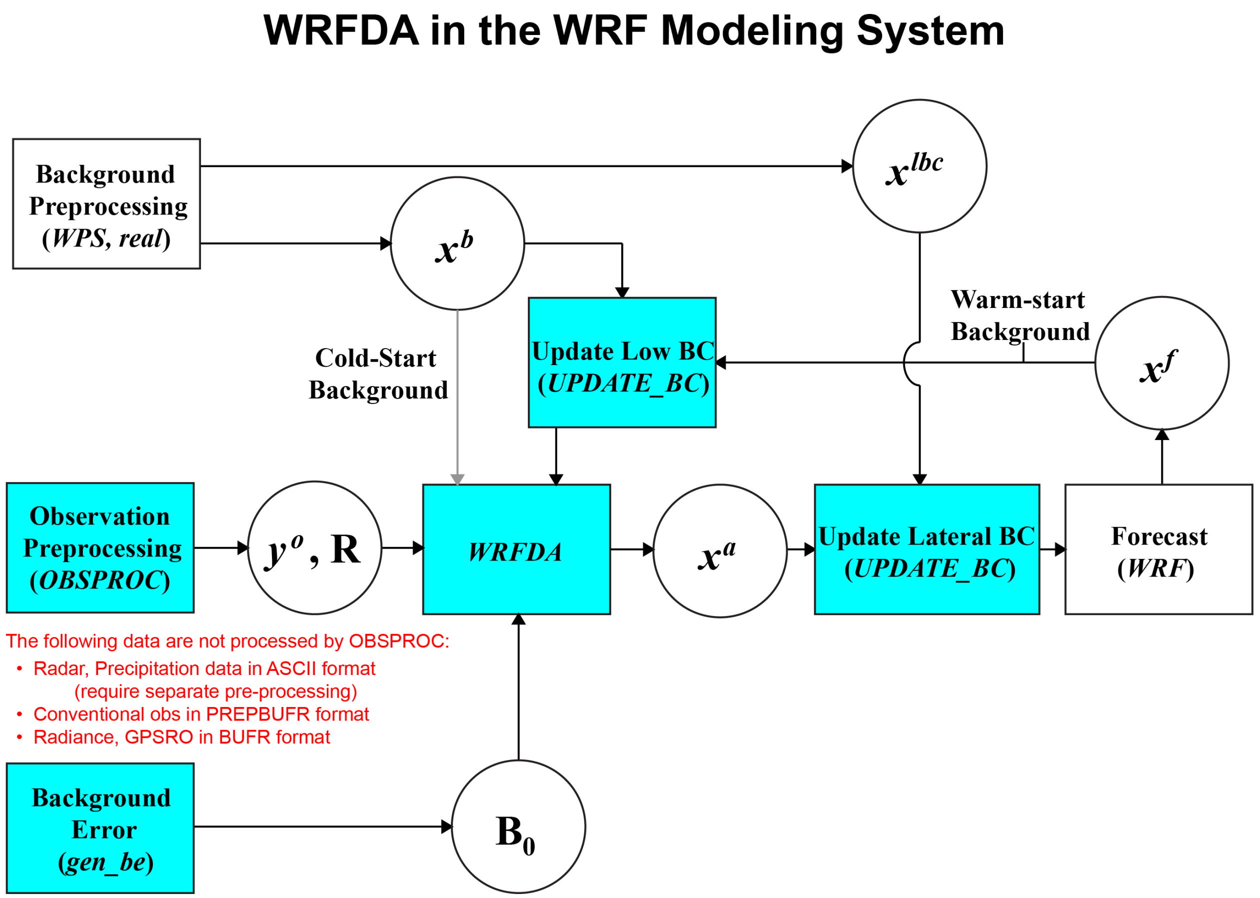

Figure 11.1: Sketch showing the relationship between datasets (circles), and algorithms (rectangles) of ARW system.

Figure 11.1 illustrates the relationship between WRFDA, the various datasets, and the other components of a typical NWP system (here ARW). The WRFDA assimilation proceeds as described in Barker et al. (2004). A number of recent upgrades to the WRFDA algorithm will be described in Section 11.2.

The three inputs to WRFDA are:

a) First guess $\mathbf{x^b}$— In cold-start mode, this is typically a forecast/analysis from another model interpolated to ARW grid (and variables) via the WPS and ARW *real* programs. In cycling mode, the first guess is a short-range (typically 1–6 hour) ARW forecast.

b) Observations $\mathbf{y^o}$— In the current version of WRFDA, observations may be supplied either in PREPBUFR format (*ob_format=1*) or an ASCII "little_r" format (*ob_format=2*). An observation preprocessor (OBSPROC) is supplied with the code release to perform basic quality control, assign "total" observation errors ($\mathbf{R} = \mathbf{E} + \mathbf{F}$ in Fig. 11.1), and reformat observations from the MM5 *little_r* text format into WRFDA's own text format. Details can be found in Barker et al. (2003, 2004).

c) Background error covariances $\mathbf{B}$— used to define the spatial and multivariate response of the analysis to an observation. In variational systems, these covariances are typically calculated off-line, and significant tuning is required to optimize performance for a particular application (e.g., Ingleby (2001); Wu et al. (2002)). The amount of work required to do this satisfactorily is significant, and should not be underestimated. In order to assist the user, the WRFDA developers supply the following: i) a default set of statistics used for the initial set up of a domain; ii) a utility *gen_be* (described in Section 11.3) to process ensembles of forecasts into the appropriate control variable space; and iii) diagnostic routines to assess the accuracy of observation and background error statistics. These routines include both innovation vector-based approaches (Hollingsworth and Lonnberg, 1986) and variational tuning approaches (Desroziers and Ivanov, 2001).

Following assimilation of all data, an analysis $\mathbf{x^a}$ is produced that must be merged with the existing lateral boundary conditions $\mathbf{x^{lbc}}$ in the *UPDATE_BC* utility (Barker et al. (2003)). At this stage, the *wrfbdy* lateral boundary condition files ($\mathbf{x^{lbc}}$) output of WPS/real is updated to make the lateral boundaries consistent with the analysis, and surface fields (e.g. SST) are also updated in the *wrfinput* analysis file.

11.2 Improvements to the WRFDA Algorithm

Relative to that described in the MM5 3DVAR technical note (Barker et al., 2003) and the ARW technical note Version 3 (Skamarock et al., 2008), the latest version of WRFDA (V4) contains a number of improvements, including four-dimensional variational (4D-Var) and hybrid variational/ensemble (hybrid-EnVar) data assimilation techniques, the direct assimilation of satellite radiances, improvements on radar data assimilation, and more choices of control variables among other new capabilities. These will be briefly overviewed below and more details can be found in cited references.

11.2.1 4D-Var and forecast sensitivity to observations

Initial capability of 4D-Var was introduced in WRFDA 3.1 (Huang et al., 2009), which has been further improved by Zhang et al. (2013, 2014a). WRFDA 4D-Var allows the use of LBC control variables and Jc-DFI (to control the gravity wave). WRFDA analysis in 4D-Var mode involves forward integration of the tangent linear model (TLM) and backward integration of the adjoint model (ADJ) of ARW during the minimization in the assimilation time window. In Version 4.0, WRFPlus code (i.e., TLM/ADJ of WRF) is fully integrated into the WRF main code repository, which will ease future code maintenance and development. While the TLM/ADJ (located under **wrftladj** directory of WRF source code) of the full ARW dynamics is available in WRFPlus code, only a few WRF physics schemes have corresponding TLM/ADJ, including the large-scale condensation and modified Kessler (warm-rain) (Wang et al., 2013b) scheme for microphysics, a simplified cumulus parameterization scheme, vertical diffusion, and gravity wave drag. TLM/ADJ of the two new features in ARW V4, hybrid vertical coordinate and moist potential temperature, is not implemented yet in WRFPlus V4, but expected to be available in a future release. It is worth noting that precipitation data can be assimilated with 4D-Var since version 3.4 (Ban et al., 2017).

Prior to version 4.3, WRFDA's 4D-Var analysis can only be run at the same horizontal resolution as that of running the WRF model forecast. This limits 4D-Var's application at high resolution due to its high computational demand. From version 4.3, an option of running incremental 4D-Var analysis (i.e., iterative minimization process) at a lower resolution than that for the model forecast is available to speed up 4D-Var and the stand-alone interpolation utility is also provided to obtain high-resolution analysis from the low-resolution analysis. With mutiple outer loops, incremental 4D-Var analysis can have gradually increased minimization resolutions for different outer loops. This new 4D-Var capability is referred to as the Multi-Resolution Incremental 4D-Var (MRI-4DVAR) and its implementation details are documented by Liu et al. (2020). MRI-4DVAR was first applied to severe storm events at convective-scale (Liu et al., 2020; Wu et al., 2020)).

The capability of computing the forecast sensitivity to observations (FSO) was also introduced in WRFDA (Zhang et al., 2015). FSO allows the calculation of the forecast impact of different observations using the adjoint of ARW and WRFDA. Notice that the Lanczos minimization algorithm instead of the Conjugate Gradient Method needs to be used when calculating FSO with WRFDA.

11.2.2 Hybrid variational/ensemble techniques

WRFDA's 4D-Var provides implicitly flow-dependent forecast error covariance through the use of the linear forecast model to evolve perturbations through a short time window. However, this comes at a cost; there are both computational as well as human resources required to maintain a linear forecast model and its adjoint.

Hybrid variational/ensemble data assimilation attempts to combine the benefits of ensemble data assimilation (flow dependence and flexibility) with those of variational systems (simultaneous treatment of observations, dynamical/physical constraints, complex quality control, treatment of nonlinearities via an outer loop, etc.). The WRFDA hybrid algorithm (Wang et al., 2008a,b) adopts the so-called α control variable formulation, implemented first at UK MetOffice. WRFDA hybrid can run in 3D (i.e., hybrid-3DEnVar) or 4D (i.e., hybrid-4DEnVar) mode and allows a dual-resolution configuration (Schwartz et al., 2015), i.e., the deterministic background and analysis at high resolution and ensemble input at lower resolution.

It is worth noting that the hybrid-EnVar algorithm produces a single deterministic analysis with flow-dependent background error covariance formed by the ensemble input, which can be obtained in different ways. The easiest way is to obtain the ensemble input from a "third-party" ensemble prediction system (EPS), e.g., NCEP's Global Ensemble Forecast System (GEFS). In that case, computational cost is significantly reduced because there is no need to run the own ensemble forecasts. An arguably better way is to produce your own ensemble analysis and forecast with your choice of model and resolution. The WRFDA package includes a program to perform the ensemble transform Kalman filter (ETKF) to produce the ensemble analysis and then ensemble forecasts can be generated and used as the input of the WRFDA hybrid analysis. Another possibility of producing ensemble analyses is to run an ensemble of WRFDA hybrid-EnVar with perturbed observations for each member analysis.

11.2.3 Satellite radiance data assimilation

The capability of radiance data assimilation was introduced in WRFDA 3.1 (Liu and Barker, 2006). Most of the BUFR format radiance data (HIRS, AMSU-A/B, MHS, AIRS, IASI, ATMS, SSMIS, and SEVIRI) used operationally in the NCEP's GFS model can be ingested by WRFDA. In addition, AMSR2 radiance data in HDF format (Yang et al., 2016) and GOES-Imager radiances (Yang et al., 2017) and Himawari-AHI radiances (Wang et al., 2018; Xu et al., 2021) in NETCDF format can also be assimilated. The WRFDA system is unique in that it interfaces to the two most widely used fast Radiative Transfer Models (RTMs): the Radiative Transfer for TOVS (RTTOV) and the Community Radiative Transfer Model (CRTM), developed and maintained by the European Organisation for the Exploitation of Meteorological Satellites (EUMETSAT) and the U.S. Joint Center for Satellite Data Assimilation (JCSDA), respectively. A flexible interface to both RTTOV and CRTM ensures that WRFDA users can assimilate radiance data from all sensors that can be simulated by either RTM, provided that corresponding data interface and quality control have been implemented.

Satellite radiance measurements and RTMs are prone to systematic errors (i.e., biases) that must be corrected before radiances can be assimilated. Biases typically vary with platform, instrument, channel, scan angle, and atmospheric conditions. WRFDA adopts the so-called variational bias correction (VarBC) algorithm for adaptive and online radiance bias correction, which updates the bias correction coefficients within the linear regression as a part of the variational minimization (Dee, 2004; Auligne et al., 2007). It is worth mentioning that an offline VarBC functionality is provided within WRFDA to generate statistics for bias correction coefficients without running an actual WRFDA analysis, which is useful when conducting data assimilation experiments for a short period (Liu et al., 2012).

For radiance assimilation under clear-sky condition, three advanced cloud detection methods for hyperspectral infrared sensors such as AIRS and IASI were implemented in WRFDA (Xu et al., 2013, 2014, 2015, 2016; Auligne, 2014a,b), which allows the assimilation of the channels peaking above the cloud. In version 3.9, all-sky radiance assimilation capability was introduced for AMSR2 radiance data (Yang et al., 2016) with the development of the so-called "symmetric error model" for all-sky data (Geer and Bauer, 2011).

11.2.4 Radar data assimilation

The initial capability to assimilate Doppler radar radial velocity and reflectivity observations is available in WRFDA v3 (Xiao et al., 2005, 2007a,b, 2008). In order to analyze the vertical velocity as a result of assimilating radar radial velocity, the Richarson balance equation and its linear and adjoint codes were introduced. For reflectivity assimilation, total water is used as a control variable. This requires a partitioning between water vapor and hydrometeor increments during the minimization procedure. A warm-rain parameterization is included to assist the calculation of hydrometeors, which includes condensation of water vapor into cloud, accretion of cloud by rain, automatic conversion of cloud to rain, and evaporation of rain to water vapor. The observation operators for Doppler radial velocity and reflectivity are included.

Since version 3.7, WRFDA includes an additional option to assimilate radar reflectivity retrieved hydrometeor profiles in 3D-Var or 4D-Var mode (Wang et al., 2013a,b; Sun and Wang, 2013). A preliminary capability to assimilate null-echo radar reflectivity is also implemented.

In version 4.2, a new option was introduced for directly assimilating radar reflectivity using a radar operator and its TLM/ADJ, which takes into account the ice-phase hydrometeors (dry and wet snow and graupel) (Wang and Liu, 2019).

11.2.5 Aerosol/Chemical data assimilation

Aerosol/Chemical data assimilation capability is added in version 4.3. Currently it allows the assimilation of 6 types of surface measurements (PM2.5, PM10, O3, CO, NO2, SO2) with 3D-Var, which can provide the analyzed initial conditions for WRF-Chem. This new capability is documented by Sun et al. (2020). The four gas-phase analysis variables include O3, CO, NO2 and SO2. For aerosols, it works with either GOCART or MOSAIC (4 bin) aerosol scheme in WRF-Chem, consisting of either 15 or 32 species, respectively. Note that the standard gen_be package included in WRFDA cannot obtain the background error statistics for aerosol/chemical variables. Users will need to use another standalone package https://github.com/wrf-model/GENBE_2.0 to generate a be.dat file that contains the background errors of aerosol/chemical variables.

11.2.6 Choice of control variables

WRFDA uses the square root B preconditioning such that $\mathbf{B} = \mathrm{U}\mathrm{U}^{\mathrm{T}}$ (see 11.3 for more details). The background error covariance matrix $\mathbf{B}$ is never explicitly computed in model space $\mathbf{x}'$: u, v, T, q, p_s. WRFDA's cost function is iteratively minimized in control variable space $\mathbf{v}$, which is related to model space via the control variable transform U, i.e.,

$$\mathbf{x}' = \mathrm{U}\mathbf{v} = \mathrm{U}_p\mathrm{U}_v\mathrm{U}_h\mathbf{v}. \tag{11.2}$$

The expansion $\mathrm{U} = \mathrm{U}_p\mathrm{U}_v\mathrm{U}_h$ represents the various stages of covariance modeling: horizontal correlations U_h through recursive filter, vertical covariances U_v through EOF decomposation, and multivariate covariances U_p through statistical regression.

The components of $\mathbf{v}$ are chosen so that their error cross-correlations are negligible, thus permitting the matrix $\mathbf{B}$ to be block-diagonalized. There are three choices of control variables in WRFDA through a namelist parameter "cv_options":

- cv_options=5: Streamfunction ψ', unbalanced velocity potential χ'_u, unbalanced temperature T'_u, pseudo relative humidity rh', unbalanced surface pressure ps'_u. This option allows the statistical cross-correlation between mass and wind field and univariate rh analysis (i.e., no cross correlation between rh and other variables).
- cv_options=6 (Chen et al., 2013): Streamfunction ψ', unbalanced velocity potential χ'_u, unbalanced temperature T'_u, unbalanced pseudo relative humidity rh'_u, unbalanced surface pressure ps'_u. In addition to mass-wind balance, this option allows the cross-correlation between moisture and other variables, which may be more important in tropical regions.
- cv_options=7 (Sun et al., 2015): zonal wind u', meridional wind v', temperature T', pseudo relative humidity rh', surface pressure ps'. There is no cross-correlation between those variables (so completely univariate analysis).

An additional cv_options=3 is similar to cv_options=5 except that it uses recursive filter instead of EOF decomposition for vertical covariance and the corresponding background error covariance statistics (provided with WRFDA release) was not based upon ARW forecasts. This option is useful when debugging code for new development (e.g., adding a new observation type), but not recommended for operational setting, in which the analysis and forecast performance is critical. For optimal performance, it is recommended to follow the procedure described in subsection (11.3) to obtain the background error covariance statistics for selected cv_options=5, 6, or 7 with appropriate ARW model setting.

In addition to five control variables whose setting is controlled by **cv_options**, WRFDA can analyze variables related to the hydrometeors (*qcloud*, *qrain*, *qice*, *qsnow*, and *qgraupel*) and vertical velocity w. These control variables are needed for assimilating cloud/precipitation-affected observations (e.g., radar reflectivity, all-sky radiances) and radar radial velocity data. The analysis of hydrometeor variables and vertical velocity is controlled by the namelist parameters **cloud_cv_options** (=0, 1, 2, or 3) and **use_cv_w** (=true or false), respectively.

11.2.7 Other improvements

Several other improvements are briefly described below.

a) Introduced in Version 3.8, the "weak penalty constraint" (WPEC) option (Li et al., 2015) aims to enforce quasi-gradient balance on the analysis. It was designed with the specific purpose of improving the assimilation of radar data within tropical cyclones, but may be useful for other weather phenomena of similar scales. It can be used with 3D-Var or hybrid-3DEnVar (4D-Var is not compatible with this capability).

b) In Version 4.0, a divergence constraint (DIVC) term was added to model the correlation between u and v. The DIVC was implemented by adding a term in the cost function that constrains the horizontal divergence (Tong et al., 2016).

c) Introduced in Version 4.0, the large scale analysis constraint (LSAC) option (Vendrasco et al., 2016) ensures that the convective-scale analysis does not distort the underlining large-scale balance and eliminates possible large-scale bias in the ARW background. The global analysis or forecast, such as that from GFS or FNL, is treated as bogus observations and assimilated via WRFDA. The input data for LSAC is prepared using WPS/REAL, the same as preparing for ARW input data.

d) A new option to assimilate GPS Radio Occultation (GPSRO) refractivity data using the GPS Excess Phase (GPSEPH) nonlocal operator (Chen et al., 2009) is added in Version 4.0 with a parallelization strategy described in (Zhang et al., 2014b).

e) Since Version 3.5, WRFDA can assimilate wind observations in terms of wind speed and direction (Huang et al., 2013; Gao et al., 2015), in addition to originally assimilating u and v components.

f) Version 4.2 introduced the capability for the variational bias correction of TAMDAR aircraft temperature observations (Gao et al., 2019).

g) A version of the package for the background error covariance statistics and ensemble perturbation generation (called gen_be_v3) was introduced in version 4.2 and then updated in version 4.3. The major advantage of gen_be_v3 is that it is much more computationally efficient than the existing gen_be package.

11.3 Background Error Covariances

Forecast ("first guess" or "background") error covariances are a vital input to variational data assimilation systems. They influence the analysis fit to observations and also completely define the analysis response away from observations. The latter impact is particularly important in data-sparse areas of the globe. Unlike ensemble filter data assimilation techniques (e.g., the Ensemble Adjustment Kalman Filter, the Ensemble Transform Kalman Filter), 3/4D-Var systems do not explicitly evolve forecast error covariances in real-time (although both 4D-Var and hybrid variational/ensemble data assimilation techniques currently being developed within WRFDA implement flow-dependent covariances implicitly). Instead, climatologic statistics are usually estimated offline. The "NMC-method", in which forecast error covariances are approximated using forecast difference (e.g., T+48 minus T+24) statistics, is a commonly used approach (Parrish and Derber, 1992). Experiments at ECMWF (Fisher, 2003) indicate superior statistics may be obtained using a cycling analysis/forecast ensemble prediction system based on perturbed observations/physics.

Recent advances permit the use of flow-dependent forecast error covariances in 3D/4D-Var through, for example, grid transformations (Desroziers, 1997), anisotropic recursive filters (Wu et al., 2002; Purser et al., 2003), or observation-space formulations of the variational problem (Daley and Barker, 2001). Flow-dependence may be enhanced in 4D-Var through the use of the forecast model to provide dynamical consistency to the evolving forecast state during 4D-Var's time window (Rabier et al., 1998). Still, the practical effort required to specify and implement flow-dependent error covariances in 3/4D-Var is significant.

The development of a unified global/regional WRFDA system, and its widespread use in the WRF community has necessitated the development of an efficient, portable forecast background error covariance calculation code. Numerous applications have also indicated that superior results are obtained if one invests effort in calculating domain-specific error covariances, instead of using the the default statistics supplied with the WRFDA release. In this section, the *gen_be* code developed by NCAR/MMM to generate forecast error statistics for use with the WRFDA system is described.

The background error covariance matrix is defined as

$$\mathbf{B} = \overline{\epsilon\epsilon^T} \simeq \overline{\mathbf{x}'\mathbf{x}'^T}, \tag{11.3}$$

where the overbar denotes an average over time and/or geographical area. The true background error ϵ is not known in reality, but is assumed to be statistically well-represented by a model state perturbation $\mathbf{x}'$. In the standard NMC-method (Parrish and Derber, 1992), the perturbation $\mathbf{x}'$ is given by the difference between two forecasts (e.g., 24 hour minus 12 hour) verifying at the same time. Climatological estimates of background error may then be obtained by averaging such forecast differences over a period of time (e.g., one month). An alternative strategy proposed by (Fisher, 2003) makes use of ensemble forecast output, defining the $\mathbf{x}'$ vectors as ensemble perturbations (ensemble minus ensemble mean). In either approach, the

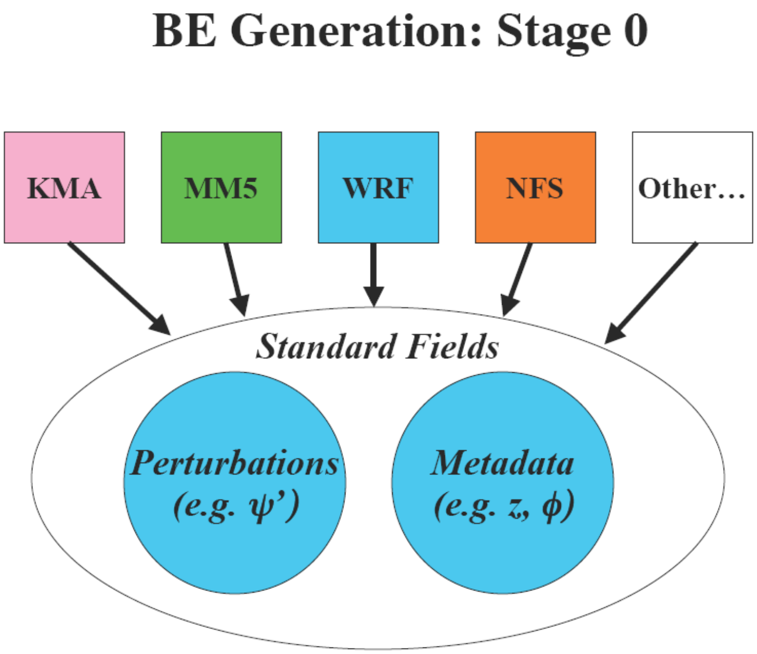

Figure 11.2: Sketch of the role of Stage 0 converters in transforming model-specific data (e.g., ARW, KMA global model, etc.) to standard perturbation fields and relevant metadata (e.g., latitude, height, land/sea, etc.).

end result is an ensemble of model perturbation vectors from which estimates of background error may be derived. The *gen_be* utility has been designed to work with either forecast difference, or ensemble-based, perturbations. Using the NMC-method, $\mathbf{x}' = \mathbf{x_{T2}} - \mathbf{x_{T1}}$ where $T2$ and $T1$ are the forecast difference times (e.g., 48h minus 24h for global, 24h minus 12h for regional). Alternatively, for an ensemble-based approach, $\mathbf{x_k}' = \mathbf{x_k} - \bar{\mathbf{x}}$, where the overbar is an average over ensemble members $k = 1, n_e$. The total number of binary files produced by this stage is $n_f \times n_e$ where n_f is the number of forecast times used (e.g., for 30 days with forecast every 12 hours, $n_f = 60$). Using the NMC-method, $n_e = 1$ (1 forecast difference per time). For ensemble-based statistics, n_e is the number of ensemble members.

As described above, the WRFDA background error covariances are specified not in model space $\mathbf{x}'$, but in a control variable space $\mathbf{v}$, which is related to the model variables (e.g., wind components, temperature, humidity, and surface pressure) via the control variable transform defined in (11.2). Both (11.2) and its adjoint are required in WRFDA. To enable this, the (offline) background error utility is used to compute components of the forecast error covariance matrix modeled within the U transform. This process is described in the following subsections.

The background error covariance generation code *gen_be* is designed to process data from a variety of regional/global models (e.g., ARW, MM5, KMA global model, NFS, etc.), and process it in order to provide error covariance statistics for use in variational data assimilation systems. The initial, model-dependent "stage 0" is illustrated in Fig. 11.2.

Alternative models use different grids, variables, data formats, etc., and so initial converters are required to transform model output into a set of standard perturbation fields (and metadata), and to output them in a standard binary format for further, model-independent processing. The standard grid-point fields are as follows.

- Perturbations: Streamfunction $\psi'(i,j,k)$, velocity potential $\chi'(i,j,k)$, temperature $T'(i,j,k)$, relative humidity $r'(i,j,k)$, surface pressure $p'_s(i,j)$.
- Full-fields: height $z(i,j,k)$, latitude $\phi(i,j)$. (These are required for the production of background error statistics stored in terms of physics variables, rather than tied to a specific grid. This flexibility is included in *gen_be* through a namelist option to define the bins over which data is averaged in a variety of ways (e.g., latitude height, grid points). Land-sea and orographic effects may also be represented in this way.

In general, the *stage_0* converters are developed and maintained by those supporting individual models. Only the WRF-to-standard-fields converter *gen_be_stage0_wrf* is maintained and supported by ARW effort.

11.3.1 Removal of time-mean

In order to calculate covariances between fields, the average value must first be removed. This is performed in the first stage utility *gen_be_stage1*.

11.3.2 Multivariate Covariances: Regression coefficients and unbalanced variables

The second stage of *gen_be (gen_be_stage2)* provides statistics for the unbalanced fields χ_u, T_u, and P_{su} used as control variables in WRFDA. The unbalanced control variables are defined as the difference between full and balanced (or correlated) components of the field. In this stage of the calculation of background errors, the balanced component of particular fields is modeled via a regression analysis of the field using specified predictor fields (e.g., streamfunction; see Wu et al. (2002) for further details). The resulting regression coefficients are output for use in WRFDA's U_p transform. Currently, three regression analyses are performed resulting in three sets of regression coefficients (note: The perturbation notation has been dropped for the remainder of this chapter for clarity.):

- Velocity potential/streamfunction regression: $\chi_b(k) = c(k)\psi(k)$;
- Temperature/streamfunction regression: $T_b(k) = \sum_{k1} G(k1,k)\psi(k1)$; and
- Surface pressure/streamfunction regression: $p_{sb} = \sum_{k1} W(k1)\psi(k1)$.

The summation over the vertical index $k1$ relates to the integral (hydrostatic) relationship between mass fields and the wind field. By default, the regression coefficients c, G, and W do not vary horizontally, however options exists to relax this assumption via the *bin_type* namelist variable in order to allow representation of differences between, for example, polar, mid-latitude, and tropical dynamical and physical processes. The scalar coefficient c used to estimate velocity potential errors from those of streamfunction is permitted to vary with model level in order to represent, for example, the impact of boundary-layer physics. Latitudinal/height smoothing of the resulting coefficients may be optionally performed to avoid artificial discontinuities at the edges of latitude/height boxes.

Having computed regression coefficients, the unbalanced components of the fields are calculated as $\chi_u(k) = \chi(k) - c(k)\psi(k)$, $T_u(k) = T(k) - \sum_{k1} G(k1,k)\psi(k1)$, and $p_{su} = p_s - \sum_{k1} W(k1)\psi(k1)$. These fields are output for the subsequent calculation of the spatial covariances as described below.

11.3.3 Vertical Covariances: Eigenvectors/eigenvalues and control variable projections

The third stage (*gen_be_stage3*) of *gen_be* calculates the statistics required for the vertical component of the control variable transform. This calculation involves the projection of 3D fields on model-levels onto empirical orthogonal functions (EOFs) of the vertical component of background error covariances Barker et al. (2004). For each 3D control variable (ψ, χ_u, T_u, and r), the vertical component of $\mathbf{B}$, is calculated and an eigenvector decomposition performed. The resulting eigenvectors $\mathbf{E}$ and eigenvalues Λ are saved for use in WRFDA.

The *gen_be* code calculates both domain-averaged and local values of the vertical component of the background error covariance matrix. Eigendecomposition of the resulting $K \times K$ (K is the number of vertical levels) climatological vertical error covariance matrix $\mathbf{B} = \mathbf{E}\Lambda\mathbf{E}^T$ results in both domain-averaged and local eigenvectors $\mathbf{E}$ and eigenvalues Λ. Both sets of statistics are included in the dataset supplied to WRFDA, allowing the choice between homogeneous (domain-averaged) or local (inhomogeneous) background error variances and vertical correlations to be chosen at run time Barker et al. (2004). Having calculated and stored eigenvectors and eigenvalues, the final part of *gen_be_stage3* is to project the entire sequence of 3D control variable fields into EOF space $\mathbf{v_v} = U_v^{-1}\mathbf{v_p} = \Lambda^{-1/2}\mathbf{E}^T\mathbf{v_p}$.

11.3.4 Horizontal Covariances: Recursive filter lengthscale (regional), or power spectra (global)

The last aspect of the climatological component of background error covariance data required for WRFDA is the horizontal error correlations, the representation of which forms the largest difference between running WRFDA in regional and global mode - the rest of *gen_be* is essentially the same for both regional and global models.

In a global application (*gen_be_stage4_global*), power spectra are computed for each of the K vertical modes of the 3D control variables ψ, χ_u, T_u, and relative humidity r, and for the 2D control variable p_{su} data. In contrast, in regional mode, horizontal correlations are computed between grid-points of each 2D field, binned as a function of distance. A Gaussian curve is then fitted to the data as described in Barker et al. (2004) to provide correlation lengthscales for use in the recursive filter algorithm.

Appendix A

Physical Constants

The following is a list of physical constants used in the model.

π	$=$	3.1415926	Pi
k	$=$	0.4	Von Karman constant
r_e	$=$	$6.370 \times 10^6 \quad \mathrm{m}$	Radius of earth
g	$=$	$9.81 \quad \mathrm{m\,s^{-2}}$	Acceleration due to gravity
Ω_e	$=$	$7.2921 \times 10^{-5} \quad \mathrm{s^{-1}}$	Angular rotation rate of the earth
σ_B	$=$	$5.67051 \times 10^{-8} \quad \mathrm{W\,m^{-2}\,K^{-4}}$	Stefan − Boltzmann constant
R_d	$=$	$287 \quad \mathrm{J\,kg^{-1}\,K^{-1}}$	Gas constant for dry air
R_v	$=$	$461.6 \quad \mathrm{J\,kg^{-1}\,K^{-1}}$	Gas constant for water vapor
c_p	$=$	$7 \times R_d/2 \quad \mathrm{J\,kg^{-1}\,K^{-1}}$	Specific heat of dry air at constant pressure
c_v	$=$	$c_p - R_d \quad \mathrm{J\,kg^{-1}\,K^{-1}}$	Specific heat of dry air at constant volume
c_{pv}	$=$	$4 \times R_v \quad \mathrm{J\,kg^{-1}\,K^{-1}}$	Specific heat of water vapor at constant pressure
c_{vv}	$=$	$c_{pv} - R_v \quad \mathrm{J\,kg^{-1}\,K^{-1}}$	Specific heat of water vapor at constant volume
c_{liq}	$=$	$4190 \quad \mathrm{J\,kg^{-1}\,K^{-1}}$	Specific heat capacity of water
c_{ice}	$=$	$2106 \quad \mathrm{J\,kg^{-1}\,K^{-1}}$	Specific heat capacity of ice
L_v	$=$	$2.5 \times 10^6 \quad \mathrm{J\,kg^{-1}}$	Latent heat of vaporization
L_s	$=$	$2.85 \times 10^6 \quad \mathrm{J\,kg^{-1}}$	Latent heat of sublimation
L_f	$=$	$3.50 \times 10^5 \quad \mathrm{J\,kg^{-1}}$	Latent heat of fusion
ρ_w	$=$	$1.0 \times 10^3 \quad \mathrm{kg\,m^{-3}}$	Density of liquid water

Appendix B

List of Symbols

Symbols used in this document are listed in alphabatical order in this appendix.

Symbols	*Definition*
a	generic variable
A	coefficient (Chapter 4), base-state lapse rate constant (Chapter 5)
B	Vertical profile in hydrid coordinate definition (Chapter 2)
$\mathbf{B}$	background error covariance matrix
c	scalar coefficient
c_s	speed of sound
C_k	a constant used in TKE closure
Cr	Courant number
Cr_{max}	maximum Courant number
Cr_{theory}	Courant number from Table 3.1
Cr_β	activation Courant number in vertical velocity damping
C_s	a constant used in eddy viscosity calculation
D	deformation
D_{nm}	deformation tensor, where n, m = 1, 2 and 3
e	cosine component of the Coriolis term (Chapters 2, 3); turbulent kinetic energy (Chapter 4)
$\mathbf{E}$	observation error covariance matrix
f	sine component of the Coriolis term
F	forcing terms for U, V, W, Θ and Q_m
$\mathbf{F}$	representivity error covariance matrix
$F_{X_{cor}}$	Coriolis forcing terms for $X = U$, V, and W
$F_{1,2}$	coefficients for weighting functions in specified boundary condition
g	acceleration due to gravity
G_k	regression coefficient
H	observation operator
J	cost function
$K_{dh,dv}$	horizontal and vertical eddy viscosity for gravity wave absorbing layer
$K_{h,v}$	horizontal and vertical eddy viscosities

Symbols	*Definition*
l_0	minimum length scale for dissipation
$l_{h,v}$	horizontal and vertical length scales for turbulence
l_{cr}	critical length scale for dissipation
L	latent heat of condensation
$L_{x,y}$	periodicity length in x and y
m	map scale factor
n_s	ratio of the RK3 time step to the acoustic time step
N	Brunt-Väisälä frequency
p	pressure
p'	perturbation pressure
p_0	reference sea-level pressure
p_c	dry hydrostatic pressure difference between the surface and the model top
p_d	dry hydrostatic pressure
$p_{t,s}$	dry hydrostatic pressure at the top and surface of the model
P_r	Prandtl number
q	generic scalar
$q_{c,i,r,s}$	mixing ratios for cloud water, ice, rain water and snow
q_m	generic mixing ratios for moisture
q_v	mixing ratio for water vapor
q_{vs}	saturation mixing ratio for water vapor
Q_m	generic coupled moisture variable
r	relative humidity
r_e	radius of earth
R	remaining terms in equations
R_d	gas constant for dry air
R_v	gas constant for water vapor
t	time
Δt	a full model time step
T	temperature
T_0	reference sea-level temperature
u	horizontal component of velocity in x-direction
U	coupled horizontal component of velocity in x-direction (Chapters 2, 3, 6, 7); control variable transform (Chapter 11)
U_h	horizontal correlation
U_p	multivariate covariance
U_v	vertical covariance
v	horizontal component of velocity in y-direction
$\mathbf{v}$	three dimensional vector velocity
V	coupled horizontal component of velocity in y-direction
$\mathbf{V}$	three dimensional coupled vector velocity
w	vertical component of velocity
W	coupled vertical component of velocity

Symbols	*Definition*
W_k	regression coefficient
z	height
z_d	depth of damping layer
z_{top}	height of model top
α	inverse density of air
α'	perturbation inverse density of air
$\bar{\alpha}$	inverse density of air for the reference state
α_d	inverse density of dry air
α_r	local rotation angle between y-axis and the meridian
β	off-centering coefficient for semi-implicit acoustic step
γ	ratio of heat capacities for dry air at constant pressure and volume
γ_d	divergence damping coefficient
γ_e	external mode damping coefficient
γ_g	damping coefficient for upper boundary gravity wave absorbing layer
γ_r	Rayleigh damping coefficient
ϵ	molecular weight of water over the molecular weight of dry air (Chapter 4); true background error (Chapter 11)
η	terrain-following hybrid sigma-pressure vertical coordinate
$\dot{\eta}$	contravariant 'vertical' velocity or coordinate velocity
θ	potential temperature
θ_e	equivalent potential temperature
θ_m	moist potential temperature
Θ_m	coupled moist potential temperature
$\bar{\mu}_d$	reference state vertical coordinate metric
μ_d	vertical coordinate metric
τ	acoustic time (Chapter 3), vertical structure function for Rayleigh damping (Chapter 4)
τ_{nm}	stress tensor (Chapter 4) where $n.m = 1$, 2 and 3
$\Delta\tau$	acoustic time step
ϕ	geopotential (Chapters 2, 3, 5); latitude (Chapter 11)
$\bar{\phi}$	geopotential for reference state
ϕ'	perturbation geopotential
Φ	generic prognostic variable (coupled)
ψ	generic variable (Chapter 6)
ψ'	streamfunction increment
χ'	velocity potential increment
ω	same as $\dot{\eta}$
Ω	coupled coordinate velocity
Ω_e	angular rotation rate of the earth

Subscripts/Superscripts	*Definition*
$()_d$	dry
$()_h$	hydrostatic
$()_0$	base state sea-level constant
$\overline{()}$	reference state
$()'$	perturbation from reference state
$()^{t^*}$	full value at a Runge-Kutta step
$()''$	perturbation from Runge-Kutta step value in acoustic steps

Appendix C

Acronyms

AFWA	Air Force Weather Agency
API	Application Program Interface
ARPS	Advanced Regional Prediction System
ARW	Advanced Research WRF
BUFR	Binary Universal Form for the Representation of Meteorological Data
CAM	Community Atmosphere Model
CAPE	Convectively Available Potential Energy
CAPS	Center for the Analysis and Prediction of Storms
CG	Coarse grid (also referred to as the parent domain)
CGM	Conjugate Gradient Method
COAMPS	Coupled Ocean / Atmosphere Mesoscale Prediction System
COMET	Cooperative Program for Operational Meteorology, Education, and Training
DFI	Digital Filtering Initialization
DTC	Developmental Testbed Center
ECMWF	The European Centre for Medium-Range Weather Forecasts
EOF	Empirical Orthogonal Function
ESMF	Earth System Modeling Framework
FAA	Federal Aviation Administration
FG	Fine grid (also referred to as the child domain)
FGAT	First Guess at Appropriate Time
FSL	Forecast System Laboratory
GFDL	Geophysical Fluid Dynamics Laboratory
GFS	Global Forecast System
GRIB	Gridded Binary
GRIMs	The Global and Regional Integrated Model System
IFS	The Integrated Forecast System
KIAPS	Korean Institute of Atmospheric Prediction Systems
KMA	Korean Meteorological Administration
LSM	Land Surface Model
MKS	Meter Kilogram Second
MM5	Pennsylvania State / NCAR Mesoscale Model Version 5
MMM	Mesoscale and Microscale Meteorology Division
MRF	Medium Range Forecast Model
NAM	North American Mesoscale Model
NCAR	National Center for Atmospheric Research
NCEP	National Centers for Environmental Prediction
NFS	Non-hydrostatic Forecast System (Central Weather Bureau of Taiwan)

NMM	Nonhydrostatic Mesoscale Model
NOAA	National Oceanographic and Atmospheric Administration
NRL	Navy Research Laboratory
NWP	Numerical Weather Prediction
OSU	Oregon State University
PBL	Planetary Boundary Layer
PPM	Piecewise Parabolic Method
QNM	Quasi Newton Method
RHS	Right Hand Side
RRTM	Rapid Radiative Transfer Model
RUC	Rapid Update Cycle
TKE	Turbulent Kinetic Energy
UCAR	University Corporation for Atmospheric Research
YSU	Yonsei University (Korea)
VAR	Variational Data Assimilation
WPS	WRF Preprocessing System (programs geogrid, ungrib, metgrid)
WRF	Weather Research and Forecasting Model
WSF	WRF Software Framework

Bibliography

Alapaty K, D. Niyogi, F. Chen, P. Pyle, A. Chandrasekar, and N. Seaman, 2008: Development of the flux-adjusting surface data assimilation system for mesoscale models. *J. Appl. Meteorol. Climatol.*, **47**, 2331–2350, doi:10.1175/2008JAMC1831.1.

Alapaty, K., J. A. Herwehe, T. L. Otte, C. G. Nolte, O. R. Bullock, M. S. Mallard, J. S. Kain, and J. Dudhia, 2012: Introducing subgrid-scale cloud feedbacks to radiation for regional meteorological and climate modeling. *Geophys. Res. Lett.*, **39**, L24809, doi:https://doi.org/10.1029/2012GL054031.

Angevine, W. M., H. Jiang, and T. Mauritsen, 2010: Performance of an eddy diffusivity-mass flux scheme for shallow cumulus boundary layers. *Mon. Wea. Rev.*, **138**, 2895–2912.

Auligne, T. D., 2014: Multivariate minimum residual method for cloud retrieval. Part I: Theoretical aspects and simulated observation experiments. *Mon. Wea. Rev.*, **142**, 4383–4398.

Auligne, T. D., 2014: Multivariate minimum residual method for cloud retrieval. Part II: Real observations experiments. *Mon. Wea. Rev.*, **142**, 4399–4415.

Auligne, T., A. P. McNally, and D. P. Dee, 2007: Adaptive bias correction for satellite data in a numerical weather prediction system. *Q. J. R. Meteorol. Soc.*, **133**, 631–642.

Bae, S. Y., S.-Y. Hong, and W.-K. Tao, 2018: Development of a single-moment cloud microphysics scheme with prognostic hail for the Weather Research and Forecasting (WRF) model. *Asia-Pac. J. Atmos. Sci.*, https://doi.org/10.1007/s13143-018-0066-3.

Baek, S., 2017: A revised radiation package of G-packed McICA and two-stream approximation: Performance evaluation in a global weather forecasting model. *J. Adv. Model. Earth Syst.*, **9**, 1–13, doi:10.1002/2017MS000994.

Beljaars A.C.M., Brown A.R., Wood N. (2004) A new parametrization of turbulent orographic form drag. *Q. J. R. Meteorol Soc.*, **130**, 1327–1347. doi:10.1256/qj.03.73.

Ban, J., Z. Liu, X. Zhang, X.-Y. Huang, and H. Wang, 2017: Precipitation data assimilation in WRFDA 4D-Var: implementation and application to convection-permitting forecasts over United States. *Tellus A: Dynamic Meteorology and Oceanography*, **69:1**, 1368310, DOI: 10.1080/16000870.2017.1368310.

Barker, D. M., W. Huang, Y.-R. Guo, and A. Bourgeois, 2003: A Three-Dimensional Variational (3DVAR) Data Assimilation System for Use with MM5. NCAR Tech Note, NCAR/TN-453+STR, 68 pp, http://dx.doi.org/10.5065/D6CF9N1J.

Barker, D. M., W. Huang, Y.-R. Guo, A. Bourgeois, and X. N. Xiao, 2004: A Three-Dimensional Variational Data Assimilation System for MM5: Implementation and Initial Results *Mon. Wea. Rev.*, **132**, 897–914.

Barker, D. M., X.-Y. Huang, Z. Liu, T. Auligne, X. Zhang, S. Rugg, A. A. AL KATHERI, A. Bourgeios, J. Bray, Y. Chen, M. Demirtas, Y. Guo, T. Henderson, W. Huang, H.-C. Lin, J. Michalakes, S. Rizvi, X.-Y. Zhang, 2012: The Weather Research and Forecasting (WRF) Model's Community Variational/Ensemble Data Assimilation System: WRFDA *Bull. Amer. Meteor. Soc.*, **93**, 831–843.

Beljaars, A.C.M., 1994: The parameterization of surface fluxes in large-scale models under free convection, *Quart. J. Roy. Meteor. Soc.*, **121**, 255–270.

Berg, L.K., W.I. Gustafson, E.I. Kassianov, E. I., and L. Deng (2013), Evaluation of a modified scheme for shallow convection: Implementation of CuP and case studies, *Mon. Wea. Rev.*, **141**, 134-147, 10.1175/mwr-d-12-00136.1.

Berg, L.K, M. Shrivastava, R.C. Easter, J.D. Fast, E.G. Chapman, and Y. Liu, 2015: A new WRF-Chem treatment for studying regional scale impacts of cloud-aerosol interactions in parameterized cumuli. *Geophys. Model Devel.*, **8**, 409-429. doi:10.5194/gmd-8-409-2015.

Berner, J., K. R. Fossell, S.-Y. Ha, J. P. Hacker, and C. Snyder, 2015: Increasing the skill of probabilistic forecasts: Understanding performance improvements from model-error representations. *Mon. Wea. Rev.*, **143**, 1295–1320.

Berner, J., S.-Y. Ha, J. P. Hacker, A. Fournier, and C. Snyder, 2011: Model uncertainty in a mesoscale ensemble prediction system: Stochastic versus multi-physics representations. *Mon. Wea. Rev.*, **139**, 1972–1995.

Berner, J., G. Shutts, M. Leutbecher, and T. Palmer, 2009: A spectral stochastic kinetic energy backscatter scheme and its impact on flow-dependent predictability in the ECMWF ensemble prediction system. *J. Atmos. Sci.*, **66**, 603–626.

Berner, J., and Coauthors, 2017: Stochastic parameterization: Toward a new view of weather and climate models. *Bulletin of the American Meteorological Society*, **98 (3)**, 565–588.

Betts, A. K., 1986: A new convective adjustment scheme. Part I: Observational and theoretical basis. *Quart. J. Roy. Meteor. Soc.*, **112**, 677–691.

Betts, A. K., and M. J. Miller, 1986: A new convective adjustment scheme. Part II: Single column tests using GATE wave, BOMEX, and arctic air-mass data sets. *Quart. J. Roy. Meteor. Soc.*, **112**, 693–709.

Bougeault, P., and P. Lacarrere, 1989: Parameterization of orography-induced turbulence in a mesobeta-scale model. *Mon. Wea. Rev.*, **117**, 1872–1890.

Bowler, N. E., A. Arribas, K. R. Mylne, K. B. Robertson, and S. E. Beare, 2008: The MOGREPS short-range ensemble prediction system. *Quart. J. Roy. Meteor. Soc.*, **134**, 703–722.

Bretherton, C. S., and S. Park, 2009: A new moist turbulence parameterization in the Community Atmosphere Model. *J. Climate*, **22**, 3422–3448.

Buizza, R., M. Miller, and T. N. Palmer, 1999: Stochastic representation of model uncertainties in the ECMWF Ensemble Prediction System.

Carpenter, R. L., K. K. Droegemeier, P. R. Woodward, and C. E. Hane, 1990: Application of the Piecewise Parabolic Method (PPM) to meteorological modeling. *Mon. Wea. Rev.*, **118**, 586–612.

Cavallo, S. M., J. Dudhia and C. Snyder, 2011: A multi-layer upper boundary condition for longwave radiative flux to correct temperature biases in a mesoscale model. *Mon. Wea. Rev.*, **139**, 1952–1959.

Chen, F., and J. Dudhia, 2001: Coupling an advanced land-surface/ hydrology model with the Penn State/ NCAR MM5 modeling system. Part I: Model description and implementation. *Mon. Wea. Rev.*, **129**, 569–585.

Chen, S. Y., C. Y. Huang, Y. H. Kuo, Y. R. Guo, and S. Sokolovskiy, 2009: Assimilation of GPS refractivity from FORMOSAT-3/COSMIC using a nonlocal operator with WRF 3DVAR and its impact on the prediction of a typhoon event. *Terr. Atmos. Ocean. Sci.*, **20**, 133–154.

Chen, F., M. Tewari, H. Kusaka, and T. T. Warner, 2006: Current status of urban modeling in the community Weather Research and Forecast (WRF) model. Joint with Sixth Symposium on the Urban Environment and AMS Forum: Managing our Physical and Natural Resources: Successes and Challenges, Atlanta, GA, USA, Amer. Meteor. Soc., CD-ROM. J1.4.

Chen, S.-H., and W.-Y. Sun, 2002: A one-dimensional time dependent cloud model. *J. Meteor. Soc. Japan*, **80**, 99–118.

Chen, Y., S. R. H. Rizvi, X.-Y. Huang, J. Min, and X. Zhang, 2013: Balance characteristics of multivariate background error covariances and their impact on analyses and forecasts in tropical and Arctic regions. *Meteor. Atmos. Phys.*, **121**, 79–98.

Choi H., and S. Hong, 2015: An updated subgrid orographic parameterization for global atmospheric forecast models. *J. Geophys. Res.*, **120**, 12445–12457.

Chou M.-D., and M. J. Suarez, 1994: An efficient thermal infrared radiation parameterization for use in general circulation models. NASA Tech. Memo. 104606, 3, 85 pp.

Chou M.-D., and M. J. Suarez, 1999: A solar radiation parameterization for atmospheric studies. NASA Tech. Memo. 104606, 15, 40 pp.

Chou, M. D., M. J. Suarez, X. Z. Liang, and M. M. H. Yan, 2001: A thermal infrared radiation parameterization for atmospheric studies. NASA Tech. Memo. 104606, 19, 68 pp.

Collins, W.D. et al., 2004: Description of the NCAR Community Atmosphere Model (CAM 3.0), NCAR Technical Note, NCAR/TN-464+STR, 226 pp.

Cooper, W. A., 1986: Ice initiation in natural clouds. *Precipitation Enhancement — A Scientific Challenge*, Meteor. Monogr., No. 43, Amer. Met. Soc., 29–32.

Daley, R., and E. Barker, 2001: NAVDAS: Formulation and Diagnostics. *Mon. Wea. Rev.*, **129**, 869–883.

Daniels, M., K. Lundquist, J. Mirocha, D. Wiersema, and F. Chow, 2016. A new vertical grid nesting capability in the Weather Research and Forecasting (WRF) model. *Mon. Wea. Rev.*, **144**, 3725—3747. DOI:10.1175/MWR-D-16-0049.1

Davies, H. C., and R. E. Turner, 1977: Updating prediction models by dynamical relaxation: An examination of the technique. *Quart. J. Roy. Meteor. Soc.*, **103**, 225–245.

Deardorff, J. W., 1972 Numerical investigation of neutral and unstable planetary boundary layers, *J. Atmos. Sci.*, **29**, 91–115.

Dee, D. P.,2004: Variational bias correction of radiance data in the ECMWF system. em In: Proc. of the ECMWF Workshop on Assimilation of High Spectral Resolution Sounders in NWP, Reading, U. K., 28 June–1 July.

Deng, A., N. L. Seaman, and J. S. Kain, 2003: A shallow-convection parameterization for mesoscale models. Part I: Submodel description and preliminary applications. J. Atmos. Sci., 60, 34–56.

Deng, A., D. Stauffer, B. Gaudet, J. Dudhia, C. Bruyere, W. Wu, F. Vandenberghe, Y. Liu, and A. Bourgeois, 2009: Update on WRF-ARW end-to-end multi-scale FDDA system. *Preprints, 10th WRF Users' Workshop*, 23–26 June, Boulder, CO, National Center for Atmospheric Research. 1.9. [Available at http://www2.mmm.ucar.edu/wrf/users/workshops/WS2009/abstracts/1-09.pdf.]

Desroziers, G., 1997: A coordinate change for data assimilation in spherical geometry of frontal structures. *Mon. Wea. Rev.*, **125**, 3030–3039.

Desroziers, G., and S. Ivanov, 2001: Diagnosis and adaptive tuning of observation-error parameters in a variational assimilation. *Quart. J. Roy. Meteor. Soc.*, **127**, 1433–1452.

Dudhia, J., 1989: Numerical study of convection observed during the winter monsoon experiment using a mesoscale two-dimensional model, *J. Atmos. Sci.*, **46**, 3077–3107.

Dudhia, J., 1995: Reply, *Mon. Wea. Rev.*, **123**, 2571–2575.

Dudhia, J., S.-Y. Hong, and K.-S. Lim, 2008: A new method for representing mixed-phase particle fall speeds in bulk microphysics parameterizations. *J. Met. Soc. Japan*, **86**, 33–44.

Durran, R. D., and J. B. Klemp, 1983: A compressible model for the simulation of moist mountain waves, *Mon. Wea. Rev.*, **111**, 2341–2361.

Dyer, A. J., and B. B. Hicks, 1970: Flux-gradient relationships in the constant flux layer, *Quart. J. Roy. Meteor. Soc.*, **96**, 715–721.

Easter, R. C., 1993: Two modified versions of Bott's positive definite numerical advection scheme. *Mon. Wea. Rev.,* **121,** 297–304.

Fels, S. B. and M. D. Schwarzkopf, 1975: The Simplified Exchange Approximation: A New Method for Radiative Transfer Calculations, *J. Atmos. Sci.*, **32**, 1475–1488.

Fisher, M., 2003: Background error covariance modeling. *Seminar on Recent Development in Data Assimilation for Atmosphere and Ocean*, 45–63, ECMWF.

Fitch, A. C., J. B. Olson, J. K. Lundquist, J. Dudhia, A. K. Gupta, J. Michalakes, and I. Barstad, 2012: Local and mesoscale impacts of wind farms as parameterized in a mesoscale NWP model. *Mon. Wea. Rev.*, **140**, 3017–3038.

Fletcher, N. H., 1962: *The Physics Of Rain Clouds.* Cambridge University Press, 386 pp.

Fu, Q., and K. N. Liou, 1992: On the correlated k-distribution method for radiative transfer in nonhomogeneous atmospheres. *J. Atmos. Sci.*, **49**, 2139–2156.

Gao, F., X.-Y. Huang, N. A. Jacobs, and H. Wang, 2015: Assimilation of wind speed and direction observations: results from real observation experiments. *Tellus A*, **67**, 27132, doi:10.3402/tellusa.v67.27132.

Gao, F., Z. Liu, J. Ma, A. N. Jacobs, P. P. Childs, and H. Wang, 2019: Variational Bias Correction of TAMDAR Temperature Observations in the WRF Data Assimilation System. *Mon. Wea. Rev.*, **147**, 1927–1945.

Geer, A. J. and Bauer, P., 2011: Observation errors in all-sky data assimilation. *Q. J. Roy. Meteorol. Soc.*, **137**, 2024–2037.

Gilmore, M. S., J. M. Straka, and E. N. Rasmussen, 2004: Precipitation uncertainty due to variations in precipitation particle parameters within a simple microphysics scheme. *Mon. Wea. Rev.*, **132**, 2610–2627.

Glotfelty, T., K. Alapaty, J. He, P. Hawbecker, X. Song, and G. Zhang, 2019: The Weather Research and Forecasting Model with Aerosol Cloud Interactions (WRF-ACI): Development, Evaluation, and Initial Application. *Mon. Wea. Rev.*, in press.

Grell, G. A., 1993: Prognostic evaluation of assumptions used by cumulus parameterizations. *Mon. Wea. Rev.*, **121**, 764-787, doi:10.1175/1520-0493(1993)121¡0764:PEOAUB¿2.0.CO;2.

Grell, G. A., and D. Devenyi, 2002: A generalized approach to parameterizing convection combining ensemble and data assimilation techniques. *Geophys. Res. Lett.*, **29(14)**, Article 1693.

Grell, G.A., S.E. Peckham, R. Schmitz, S.A. McKeen, G. Frost, W.C. Skamarock and B. Eder, 2005: Fully coupled online chemistry within the WRF model. *Atmos. Environ.*, **39**, 6957-6975.

Grell, G. A. and Freitas, S. R., 2014: A scale and aerosol aware stochastic convective parameterization for weather and air quality modeling. *Atmos. Chem. Phys.*, **14**, 5233-5250, doi:10.5194/acp-14-5233-2014.

Grenier, H., and C. S. Bretherton, 2001: A moist PBL parameterization for large-scale models and its application to subtropical cloud-topped marine boundary layers. *Mon. Wea. Rev.*, *129*, 357–377.

Gu, Y., K. N. Liou, S. C. Ou, and R. Fovell, 2011: Cirrus cloud simulations using WRF with improved radiation parameterization and increased vertical resolution. *J. Geophys. Res.*, **116**, D06119.

Hacker, J. P., C. Snyder, S.-Y. Ha, and M. Pocernich, 2011: Linear and nonlinear response to parameter variations in a mesoscale model. *Tellus A*, **63**, 429–444.

Haltiner, G. J., and R. T. Williams, 1980: *Numerical prediction and dynamic meteorology.* John Wiley & Sons, Inc., 477 pp.

Han, Jongil and Hua–Lu Pan, 2011: Revision of convection and vertical diffusion schemes in the NCEP Global Forecast System. *Wea. Forecasting*, **26**, 520–533. doi:10.1175/WAF-D-10-05038.1.

Hollingsworth, A., and P. Lonnberg, 1986: The Statistical Structure Of Short-Range Forecast Errors As Determined From Radiosonde Data. Part I: The Wind Field. *Tellus*, **38A**, 111–136.

Holtslag, A. A. M. and B. A. Boville, 1993: Local versus non-local boundary layer diffusion in a global climate model, *J. Climate*, **6**, 1825–1842.

Hong, S.-Y., 2007: Stable Boundary Layer Mixing in a Vertical Diffusion Scheme. The Korea Meteor. Soc., Fall conference, Seoul, Korea, Oct. 25-26.

Hong, S.-Y. and J.-O. J. Lim, 2006: The WRF Single-Moment 6-Class Microphysics Scheme (WSM6), *J. Korean Meteor. Soc.*, **42**, 129–151.

Hong, S.-Y. and H.-L. Pan, 1996: Nonlocal boundary layer vertical diffusion in a medium-range forecast model, *Mon. Wea. Rev.*, **124**, 2322–2339.

Hong, S.-Y., H.-M. H. Juang, and Q. Zhao, 1998: Implementation of prognostic cloud scheme for a regional spectral model, *Mon. Wea. Rev.*, **126**, 2621–2639.

Hong, S.-Y., J. Dudhia, and S.-H. Chen, 2004: A Revised Approach to Ice Microphysical Processes for the Bulk Parameterization of Clouds and Precipitation, *Mon. Wea. Rev.*, **132**, 103–120.

Hong, S.-Y., Y. Noh, and J. Dudhia, 2006: A new vertical diffusion package with an explicit treatment of entrainment processes. *Mon. Wea. Rev.*, **134**, 2318–2341.

Hong, S.-Y. and J.-H. Jang, 2018: Impacts of shallow convection processes on a simulated Boreal summer climatology in a global atmospheric model. *Asia-Pacific J. Atmos. Sci.* (2018) 54(Suppl 1): 361. doi:10.1007/s13143-018-0013-3.

Huang, X.-Y. and P. Lynch, 1993: Diabatic Digital-Filtering Initialization: Application to the HIRLAM Model., *Mon. Wea. Rev.*, **121**, 589–603.

Huang, X.-Y., Q. Xiao, D. M. Barker, X. Zhang, J. Michalakes, W. Huang, T. Henderson, J. Bray, Y. Chen, Z. Ma, J. Dudhia, Y. Guo, X. Zhang, D.-J. Won, H.-C. Lin, and Y.-H. Kuo, 2009: Four-Dimensional Variational Data Assimilation for WRF: Formulation and Preliminary Results. *Mon. Wea. Rev.*, **137**, 299–314.

Huang, X.-Y., F. Gao, N. A. Jacobs, and H. Wang, 2013: Assimilation of wind speed and direction observations: a new formulation and results from idealised experiments. *Tellus A*, **65**, 19936, doi:10.3402/tellusa.v65i0.19936.

Iacono, M. J., J. S. Delamere, E. J. Mlawer, M. W. Shephard, S. A. Clough, and W. D. Collins, 2008: Radiative forcing by long-lived greenhouse gases: Calculations with the AER radiative transfer models. *J. Geophys. Res.*, **113**, D13103.

Ide, K., P. Courtier, M. Ghil, and A. C. Lorenc, 1997: Unified notation for data assimilation: Operational, sequential and variational. *J. Met. Soc. Japan*, **75**, 181–189.

Ingleby, N. B., 2001: The statistical structure of forecast errors and its representation in the Met. Office global 3-D variational data assimilation scheme. *Quart. J. Roy. Meteor. Soc.*, **127**, 209–232.

Jankov, I., and Coauthors, 2017: A performance comparison between multiphysics and stochastic approaches within a north american rap ensemble. *Monthly Weather Review*, **145**, 1161–1179.

Janjic, Z. I., 1990: The step-mountain coordinate: physical package, *Mon. Wea. Rev.*, **118**, 1429–1443.

Janjic, Z. I., 1994: The step-mountain eta coordinate model: further developments of the convection, viscous sublayer and turbulence closure schemes, *Mon. Wea. Rev.*, **122**, 927–945.

Janjic, Z. I., 1996: The surface layer in the NCEP Eta Model, *Eleventh Conference on Numerical Weather Prediction*, Norfolk, VA, 19–23 August; Amer. Meteor. Soc., Boston, MA, 354–355.

Janjic, Z. I., 2000: Comments on "Development and Evaluation of a Convection Scheme for Use in Climate Models", *J. Atmos. Sci.*, **57**, p. 3686.

Janjic, Z. I., 2002: Nonsingular Implementation of the Mellor–Yamada Level 2.5 Scheme in the NCEP Meso model, *NCEP Office Note*, **No. 437**, 61 pp.

Jensen, A. A., J. Y. Harrington, H. Morrison, and J. A. Milbrandt, 2017: Predicting ice shape evolution in a bulk microphysics model. *J. Atmos. Sci.*, **74**, 2081–2104, https://doi.org/10.1175/JAS-D-16-0350.1.

Jimenez, P., J. Dudhia, J. F. Gonzalez-Ruoco, J. Navarro, J. P. Montavez, and E. Garcia-Bustamente, 2012: A revised scheme for the WRF surface layer formulation. *Mon. Wea. Rev.,* **140,** 898–918.

Jimenez, P. A., and J. Dudhia, 2012: Improving the representation of resolved and unresolved topographic effects on surface wind in the WRF model. *J. Appl. Meteor. Climatol.*, **51**, 300–316.

Kain, J. S., and J. M. Fritsch, 1990: A one-dimensional entraining/ detraining plume model and its application in convective parameterization, *J. Atmos. Sci.*, **47**, 2784–2802.

Kain, J. S., and J. M. Fritsch, 1993: Convective parameterization for mesoscale models: The Kain-Fritcsh scheme, *The representation of cumulus convection in numerical models*, K. A. Emanuel and D.J. Raymond, Eds., Amer. Meteor. Soc., 246 pp.

Kain, J. S., 2004: The Kain-Fritsch convective parameterization: An update. *J. Appl. Meteor.*, **43**, 170–181.

Kessler, E., 1969: On the distribution and continuity of water substance in atmospheric circulation, *Meteor. Monogr.*, **32**, Amer. Meteor. Soc., 84 pp.

Khain, A., B. Lynn, and J. Dudhia, 2010: Aerosol effects on intensity of landfalling hurricanes as seen from simulations with the WRF model with spectral bin microphysics. *J. Atmos. Sci.*, **67**, 365–384.

Khain, A., A. Pokrovsky, M. Pinsky, A. Seifert, and V. Phillips, 2004: Simulation of effects of atmospheric aerosols on deep turbulent convective clouds using a spectral microphysics mixed-phase cumulus cloud model. Part I: model description and possible applications. *J. Atmos. Sci.*, **61**, 2963–2982.

Klemp, J. B., and D. K. Lilly, 1978: Numerical simulation of hydrostatic mountain waves, *J. Atmos. Sci.*, **35**, 78–107.

Klemp, J. B., and R. Wilhelmson, 1978: The simulation of three-dimensional convective storm dynamics, *J. Atmos. Sci.*, **35**, 1070–1096.

Klemp, J. B., W. C. Skamarock, and J. Dudhia, 2007: Conservative split-explicit time integration methods for the compressible nonhydrostatic equations, *Mon. Wea. Rev..*, **135,** 2897–2913.

Klemp, J. B., J. Dudhia, and A. Hassiotis, 2008: An Upper Gravity Wave Absorbing Layer for NWP Applications. *Mon. Wea. Rev..*, **136**, 3987–4004.

Knievel, J. C., G. H. Bryan, and J. P. Hacker, 2007: Explicit numerical diffusion in the WRF Model. *Mon. Wea. Rev.*, **135**, 3808–3824.

Kusaka, H. and F. Kimura, 2004: Coupling a single-layer urban canopy model with a simple atmospheric model: Impact on urban heat island simulation for an idealized case. *J. Meteor. Soc. Japan*, **82**, 67–80.

Kusaka, H., H. Kondo, Y. Kikegawa, and F. Kimura, 2001: A simple single-layer urban canopy model for atmospheric models: Comparison with multi-layer and slab models. *Bound.-Layer Meteor.*, **101**, 329–358.

Kwon, Y.-C. and S.-Y. Hong, 2017: A mass-flux cumulus parameterization scheme across gray-zone resolutoins. *Mon. Wea. Rev.* **145**, 583-598, doi:0.1175/MWR-D-16-0034.1

Lacis, A. A., and J. E. Hansen, 1974: A parameterization for the absorption of solar radiation in the earth's atmosphere. *J. Atmos. Sci.*, **31**, 118–133.

Lang, S., W.-K. Tao, J.-D. Chern, D. Wu, and X. Li, 2014: Benefits of a 4th ice class in the simulated radar reflectivities of convective systems using a bulk microphysics scheme. *J. Atmos. Sci.*, **71**, 3583–3612, https://doi.org/10.1175/JAS-D-13-0330.1

Langland, R. H., and C. S. Liou, 1996: Implementation of an E–ϵ parameterization of vertical subgrid-scale mixing in a re- gional model. *Mon. Wea. Rev.*, **124**, 905–918, https://doi.org/10.1175/1520-0493(1996)124,0905:IOAPOV.2.0.CO;2.

Laprise R., 1992: The Euler Equations of motion with hydrostatic pressure as as independent variable, *Mon. Wea. Rev.*, **120**, 197–207.

Lawrence, D. M., et al., 2011: Parameterization improvements and functional and structural advances in Version 4 of the Community Land Model. *J. Adv. Model. Earth Syst.*, **3**, M03001.

Lee, C.-Y. and S. S. Chen, 2012: Symmetric and asymmetric structures of hurricane boundary layer in coupled atmosphere-wave-ocean models and observations. *J. Atmos. Sci.*, **69**, 3576–3594.

Lee, M.-S., D. Barker, W. Huang and Y.-H. Kuo, 2004: First Guess at Appropriate Time (FGAT) with WRF 3DVAR. *WRF/MM5 Users Workshop*, 22–25 June 2004, Boulder, Colorado.

Leutbecher, M., and Coauthors, 2017: Stochastic representations of model uncertainties at ECMWF: State of the art and future vision. *Quart. J. Roy. Meteor. Soc.*,**143**, 2315-2339.

Li, D., E. Bou-Zeid, M. Barlage, F. Chen, and J. A. Smith, 2013: Development and Evaluation of a Mosaic Approach in the WRF-Noah Framework. *J. Geophys. Res.*, **118**, 11918–11935.

Li, X., J. Ming, M. Xue, Y. Wang, and K. Zhao, 2015: Implementation of a dynamic equation constraint based on the steady state momentum equations within the WRF hybrid ensemble-3DVar data assimilation system and test with radar T-TREC wind assimilation for tropical Cyclone Chanthu (2010). *J. Geophys. Res. Atmos.*, **120**, 4017–4039.

Lim, K.-S. S., and S.-Y. Hong, 2010: Development of an effective double-moment cloud microphysics scheme with prognostic cloud condensation nuclei (CCN) for weather and climate models. *Mon. Wea. Rev.*, **138**, 1587–1612.

Lin, Y., and B. A. Colle, 2011: A new bulk microphysical scheme that includes riming intensity and temperature-dependent ice characteristics. *Mon. Wea. Rev.* , **139**, 1013–1035.

Lin, Y.-L., R. D. Farley, and H. D. Orville, 1983: Bulk parameterization of the snow field in a cloud model. *J. Climate Appl. Meteor.*, **22**, 1065–1092.

Lin, S.-J., and R. B. Rood, 1996: Multidimensional flux-form semi-Lagrangian transport schemes. *Mon. Wea. Rev.*, **124**, 2046–2070.

Liu, Y., T.T. Warner, J. F. Bowers, L. P. Carson, F. Chen, C. A. Clough, C. A. Davis, C. H. Egeland, S. Halvorson, T.W. Huck Jr., L. Lachapelle, R.E. Malone, D. L. Rife, R.-S. Sheu, S. P. Swerdlin, and D.S. Weingarten, 2008: The operational mesogamma-scale analysis and forecast system of the U.S. Army Test and Evaluation Command. Part 1: Overview of the modeling system, the forecast products. *J. Appl. Meteor. Clim.*, **47**, 1077–1092.

Liu, Z., J. Ban, J.-S. Hong, and Y.-H. Kuo, 2020: Multi-resolution incremental 4D-Var for WRF: Implementation and application at convective scale. *Quart. J. Roy. Meteor. Soc.*, **146**, 3661–3674.

Liu Z. and Barker D. M., 2006: Radiance Assimilation in WRF-Var: Implementation and Initial Results, *Preprints, 7th WRF Users' Workshop*, Boulder, CO, National Center for Atmospheric Research.

Liu, Z., C. S. Schwartz, C. Snyder, and S.-Y. Ha, 2012: Impact of assimilating AMSU-A radiances on forecasts of 2008 Atlantic tropical cyclones initialized with a limited-area ensemble Kalman filter. *Mon. Wea. Rev.*, **140**, 4017–4034.

Lorenc, A. C., 1986: Analysis methods for numerical weather prediction. *Quart. J. Roy. Meteor. Soc.*, **112**, 1177–1194.

Lorente-Plazas, R., P. A. Jimenez, J. Dudhia, and J. P. Montavez, 2016: Evaluating and improving the impact of the atmospheric stability and orography on surface winds in the WRF model. *Mon. Wea. Rev.*, **144**, 2685–2693.

Lynch, P., and X.-Y. Huang, 1992: Initialization of the HIRLAM Model Using a Digital Filter. *Mon. Wea. Rev.*, **120**, 1019–1034.

Lynch, P., and X.-Y. Huang, 1994: Diabatic initialization using recursive filters. *Tellus*, **46A**, 583–597.

Lynch, P., 1997: The Dolph-Chebyshev Window: A Simple Optimal Filter. *Mon. Wea. Rev.*, **125**, 655–660.

Ma, L.-M. and Z.-M. Tan, 2009: Improving the behavior of the cumulus parameterization for tropical cyclone prediction: Convection trigger. *Atmospheric Research*, **92**, 190–211, doi:10.1016/j.atmosres.2008.09.022.

Mahalov, A., and M. Moustaoui, 2009: Vertically nested nonhydrostatic model for multiscale resolution of flows in the upper troposphere and lower stratosphere. *J. Comput. Phys.*, **228**, 1294–1311, doi:10.1016/j.jcp.2008.10.030.

Mansell, E. R., C. L. Ziegler, and E. C. Bruning, 2010: Simulated electrification of a small thunderstorm with two-moment bulk microphysics. *J. Atmos. Sci.*, **67**, 171–194.

Martilli A, Clappier A, and Rotach M.W., 2002: An urban surface exchange parameterization for mesoscale models. *Bound.-Layer Meteorol.*, **104**, 261–304.

Matsui, T., S. Q. Zhang, W.-K. Tao, S. Lang, C. Ichoku, and C. Peters-Lidard, 2018: Impact of Radiation Frequency, Precipitation Radiative Forcing, and Radiation Column Aggregation on Convection-Permitting West African Monsoon Simulations. *Clim. Dyn.*, 1-21, https://doi.org/10.1007/s00382-018-4187-2

McCumber, M., W.-K. Tao, J. Simpson, R. Penc, and S.-T. Soong, 1991: Comparison of ice-phase microphysical parameterization schemes using numerical simulations of tropical convection. *J. Appl. Meteor.*, **30**, 985–1004.

Mellor, G. L., and T. Yamada, 1982: Development of a turbulence closure model for geophysical fluid problems. *Rev. Geophys. Space Phys.*, **20**, 851–875.

Michalakes, J., J. Dudhia, D. Gill, J. Klemp, and W. Skamarock, 1999: Design of a next-generation regional weather research and forecast model, *Towards Teracomputing*, World Scientific, River Edge, New Jersey, 117–124.

Michalakes, J., J. Dudhia, D. Gill, T. Henderson, J. Klemp, W. Skamarock, and W. Wang, 2004: The Weather Research and Forecast Model: Software Architecture and Performance. To appear in proceeding of *the Eleventh ECMWF Workshop on the Use of High Performance Computing in Meteorology.* 25–29 October 2004, Reading, U.K., Ed. George Mozdzynski.

Miguez-Macho, G., G. L. Stenchikov, and A. Robock, 2004: Spectral nudging to eliminate the effects of domain position and geometry in regional climate model simulations. *J. Geophys. Res.*, **109**, D13104. doi:10.1029/2003JD004495.

Milbrandt, J. A., and M. K. Yau, 2005: A multimoment bulk microphysics parameterization. Part I: Analysis of the role of the spectral shape parameter. *J. Atmos. Sci.*, **62**, 3051–3064.

Mlawer, E. J., S. J. Taubman, P. D. Brown, M. J. Iacono, and S. A. Clough, 1997: Radiative transfer for inhomogeneous atmosphere: RRTM, a validated correlated-k model for the longwave. *J. Geophys. Res.*, **102** (D14), 16663–16682.

Monin, A.S. and A.M. Obukhov, 1954: Basic laws of turbulent mixing in the surface layer of the atmosphere. *Contrib. Geophys. Inst. Acad. Sci.*, USSR, **(151)**, 163–187 (in Russian).

Morrison, H., J. A. Curry, and V. I. Khvorostyanov, 2005: A new double-moment microphysics parameterization for application in cloud and climate models, Part I: Description. *J. Atmos. Sci.*, **62**, 1665–1677.

Morrison, H., and J. O. Pinto, 2006: Intercomparison of bulk microphysics schemes in mesoscale simulations of springtime Arctic mixed-phase stratiform clouds. *Mon. Wea. Rev.*, **134**, 1880–1900.

Morrison, H., and A. Gettelman, 2008: A New Two-Moment Bulk Stratiform Cloud Microphysics Scheme in the Community Atmosphere Model, Version 3 (CAM3). Part I: Description and Numerical Tests. *J. Clim.*. **21**, 3642–3659.

Morrison, H. and J.A. Milbrandt, 2015: Parameterization of ice microphysics based on the prediction of bulk particle properties. Part 1: Scheme description and idealized tests. *J. Atmos. Sci.*, **72**, 287–311.

Morrison, H., G. Thompson, and V. Tatarskii, 2008: Impact of cloud microphysics on the development of trailing stratiform precipitation in a simulated squall line: Comparison of one- and two-moment schemes. *Mon. Wea. Rev.* , **137**, 991–1007.

Nakanishi, M., and H. Niino, 2006: An improved Mellor-Yamada level 3 model: its numerical stability and application to a regional prediction of advecting fog. *Bound. Layer Meteor.*, **119**, 397–407.

Nakanishi, M., and H. Niino, 2009: Development of an improved turbulence closure model for the atmospheric boundary layer. *J. Meteor. Soc. Japan*, **87**, 895–912.

Niu, G.-Y, Z.-L. Yang, K. E. Mitchell, F. Chen, M. B. Ek, M. Barlage, A. Kumar, K. Manning, D. Niyogi, E. Rosero, M. Tewari, Y. Xia, 2011: The community Noah land surface model with multiparameterization options (Noah-MP): 1. Model description and evaluation with local-scale measurements. *J. Geophys. Res.*, **116**, D12109.

Noh, Y., W.G. Cheon, S.-Y. Hong, and S. Raasch, 2003: Improvement of the K-profile model for the planetary boundary layer based on large eddy simulation data. *Bound.-Layer Meteor.*, **107**, 401–427.

Noilhan, J., and S. Planton, 1989: A simple parameterization of land surface processes for meteorological models. *Mon. Wea. Rev.*, **117**, 536–549.

Oleson, K. W., et al., 2010: Technical description of version 4 of the Community Land Model (CLM). NCAR Tech. Note NCAR/TN-478+STR. 266 pp.

Olson, J. B., J. S. Kenyon, W.. A. Angevine, J. M. Brown, M. Pagowski, and K. Sušelj, 2019: A Description of the MYNN-EDMF Scheme and the Coupling to Other Components in WRF-ARW. NOAA Technical Memorandum (in preparation).

Ooyama K. V., 1990: A thermodynamic foundation for modeling the moist atmosphere, *J. Atmos. Sci.*, **47**, 2580–2593.

Palmer, T. N., R. Buizza, F. Doblas-Reyes, T. Jung, M. Leutbecher, G. Shutts, M. Steinheimer, and A. Weisheimer, 2009: Stochastic Parametrization and Model Uncertainty. *ECMWF Technical Memorandum*, **598**. [Available at http://www.ecmwf.int/publications/].

Pan, H.-L., and W.-S. Wu, 1995: Implementing a mass flux convective parameterization package for the NMC Medium-Range Forecast model. NMC Office Note 409, 40 pp.

Park, Sungsu, and Christopher S. Bretherton, 2009: The University of Washington shallow convection and moist turbulence schemes and their impact on climate simulations with the Community Atmosphere Model. J. Climate, 22, 3449–3469. doi:10.1175/2008JCLI2557.1

Park, S.-H., W. Skamarock, J. Klemp, L. Fowler, and M. Duda, 2013: Evaluation of global atmospheric solvers using extensions of the Jablonowski and Williamson baroclinic wave test case. *Mon. Wea. Rev.*, **141**, 3116–3129.

Parrish, D. F., and J. C. Derber, 1992: The National Meteorological Center's Spectral Statistical Interpolation analysis system. *Mon. Wea. Rev.*, **120**, 1747–1763.

Paulson, C. A., 1970: The mathematical representation of wind speed and temperature profiles in the unstable atmospheric surface layer. *J. Appl. Meteor.*, **9**, 857–861.

Pergaud J, V. Masson, S. Malardel, and F. Couvreux, 2009: A parameterization of dry thermal and shallow cumuli for mesoscale numerical weather prediction. *Boundary-Layer Meteorol.*, **132**, 83–106.

Pleim, J. E., 2006: A simple, efficient solution of flux-profile relationships in the atmospheric surface layer, *J. Appl. Meteor. and Clim.*, **45**, 341–347

Pleim, J. E., 2007: A combined local and non-local closure model for the atmospheric boundary layer. Part 1: Model description and testing, *J. Appl. Meteor. and Climatol.*, **46**, 1383–1395.

Pleim, J.E. and R.C. Gilliam, 2008: An indirect data assimilation scheme for deep soil temperature in the Pleim-Xiu land surface model. *J. Appl. Meteor. Climatol.*, **48**, 1362–1376.

Pleim, J. E. and A. Xiu, 1995: Development and testing of a surface flux and planetary boundary layer model for application in mesoscale models. *J. Appl. Meteor.*, **34**, 16–32.

Pleim, J. E., and A. Xiu, 2003: Development of a land surface model. Part II: Data Assimilation. *J. Appl. Meteor.*, **42**, 1811–1822.

Pollard, R. T., P. B. Rhines and R. O. R. Y. Thompson, 1973: The deepening of the wind-mixed layer. *Geophys. Fluid Dyn.*, **3**, 381–404.

Powers, J. G., J. B. Klemp, W. C. Skamarock, C. A. Davis, J. Dudhia, D. O. Gill, J. L. Coen, D. J. Gochis, R. Ahmadov, S. E. Peckham, G. A. Grell, J. Michalakes, S. Trahan, W. Wang, C. S. Schwartz, G. S. Romine, Z.-Q. Liu, C. Snyder, F. Chen, M. J. Barlage, W. Yu, and M. G. Duda, 2017: The Weather Research and Forecasting (WRF) Model: Overview, system efforts, and future directions. *Bull. Amer. Meteor. Soc.,***98,** 1717–1737.

Price, J. F., T. B. Sanford, and G. Z. Forristall, 1994: Forced stage response to a moving hurricane. *J. Phy. Oceanogr.*, **24**, 233–260.

Purser, R. J., W. -S. Wu, D. F. Parrish, and N. M. Roberts, 2003: Numerical aspects of the application of recursive filters to variational statistical analysis. Part I: Spatially homogeneous and isotropic Gaussian covariances. *Mon. Wea. Rev.*, **131**, 1524–1535.

Rabier, F., H., J. N. Thepaut, and P. Courtier, 1998: Extended assimilation and forecast experiments with a four-dimensional variational assimilation system. *Quart. J. Roy. Meteor. Soc.*, **124**, 1861–1887.

Reisner, J. R., R. M. Rasmussen, and R. T. Bruintjes, 1998: Explicit forecasting of supercooled liquid water in in winter storms using the MM5 mesoscale model. *Quart. J. Roy. Meteor. Soc.*, **124**, 1071–1107.

Roberts, R. E., J. E. A. Selby, and L. M. Biberman, 1976: Infrared continuum absorption by atmospheric water-vapor in 8–12 um window. *Applied Optics*, **15 (9)**, 2085–2090.

Rodgers, C. D., 1968: Some extensions and applications of the new random model for molecular band transmission. *Quart. J. Roy. Meteor. Soc.*, **94**, 99–102.

Rutledge, S. A., and P. V. Hobbs, 1984: The mesoscale and microscale structure and organization of clouds and precipitation in midlatitude cyclones. XII: A diagnostic modeling study of precipitation development in narrow cloud-frontal rainbands. *J. Atmos. Sci.*, **20**, 2949–2972.

Ryan, B. F., 1996: On the global variation of precipitating layer clouds. *Bull. Amer. Meteor. Soc.*, **77**, 53–70.

Salamanca, F., and A. Martilli, 2010: A new building energy model coupled with an urban canopy parameterization for urban climate simulations – part II. Validation with one dimension off-line simulations. *Theor. Appl. Climatol.*, **99**, 345–356.

Sasamori, T., J. London, and D. V. Hoyt, 1972: Radiation budget of the Southern Hemisphere. *Meteor. Monogr.*, **13**, No. 35, 9–23.

Schwartz, C. S., Z. Liu, X.-Y. Huang, 2015: Sensitivity of Limited-Area Hybrid Variational-Ensemble Analyses and Forecasts to Ensemble Perturbation Resolution. *Mon. Wea. Rev.*, **143**, 3454–3477.

Schwarzkopf, M. D., and S. B. Fels, 1985: Improvements to the algorithm for computing CO2 transmissivities and cooling rates. *J. Geophys. Res.*, **90** (ND6), 541–550.

Schwarzkopf, M. D., and S. B. Fels, 1991: The simplified exchange method revisited — An accurate, rapid method for computation of infrared cooling rates and fluxes. *J. Geophys. Res.*, **96** (D5), 9075–9096.

Shin, H. H., and S.-Y. Hong, 2015: Representation of the subgrid-scale turbulent transport in convective boundary layers at gray-zone resolutions. *Mon. Wea. Rev.*, **143**, 250–271.

Shutts, G. J., 2005: A kinetic energy backscatter algorithm for use in ensemble prediction systems. *Quart. J. Roy. Meteor. Soc.*, **612**, 3079–3102.

Skamarock W. C. and J. B. Klemp, 1992: The Stability of Time-Split Numerical Methods for the Hydrostatic and the Nonhydrostatic Elastic Equations, *Mon. Wea. Rev.*: **120**, 2109–2127.

Skamarock, W. C., J. B. Klemp, J. Dudhia, D. O. Gill, D. M. Barker, M. G. Duda, X.-Y. Huang, W. Wang, J. G. Powers, 2008: A Description of the Advanced Research WRF Version 3. NCAR Tech Note, NCAR/TN-475+STR, 113 pp, http://dx.doi.org/10.5065/D68S4MVH.

Skamarock W. C. and M. L. Weisman, 2008: The impact of positive-definite moisture transport on NWP precipitation forecasts, *Mon. Wea. Rev.*, **137**, 488–494.

Skamarock, W. C, J. B. Klemp, M. G. Duda, L. Fowler, S.-H. Park, and T. D. Ringler, 2012: A Multi-scale Nonhydrostatic Atmospheric Model Using Centroidal Voronoi Tesselations and C-Grid Staggering. *Mon. Wea. Rev.*, **240**, 3090-3105, doi: 10.1175/MWR-D-11-00215.1.

Smirnova, T. G., J. M. Brown, and S. G. Benjamin, 1997: Performance of different soil model configurations in simulating ground surface temperature and surface fluxes. *Mon. Wea. Rev.*, **125**, 1870–1884.

Smirnova, T. G., J. M. Brown, S. G. Benjamin, and D. Kim, 2000: Parameterization of cold-season processes in the MAPS land-surface scheme. *J. Geophys. Res.*, **105** (D3), 4077–4086.

Smolarkiewicz, P. K., and G. A. Grell, 1990: A class of monotone interpolation schemes, *J. Comp. Phys.*, **101**, 431–440.

Stauffer D. R., and N. L. Seaman, 1990: Use of four-dimensional data assimilation in a limited-area mesoscale model. Part I: Experiments with synoptic-scale data. *Mon. Wea. Rev.*, **118**, 1250–1277.

Stauffer D. R., and N. L. Seaman, 1994: Multiscale four-dimensional data assimilation. *J. Appl. Meteor.*, **33**, 416–434.

Stephens, G. L., 1978: Radiation profiles in extended water clouds. Part II: Parameterization schemes, *J. Atmos. Sci.*, **35**, 2123–2132.

Subin, Z.M., Riley, W.J. and Mironov, D. 2012. Improved lake model for climate simulations, *J. Adv. Model. Earth Syst.*, **4**, M02001.

Sukoriansky, S., B. Galperin, and V. Perov, 2005: Application of a new spectral model of stratified turbulence to the atmospheric boundary layer over sea ice. *Bound.-Layer Meteor.*, **117**, 231–257.

Sun, J., and H. Wang, 2013: Radar Data Assimilation with WRF 4D-Var. Part II: Comparison with 3D-Var for a Squall Line over the U.S. Great Plains. *Mon. Wea. Rev.*, **141**, 2245?-2264.

Sun, J., H. Wang, W. Tong, Y. Zhang, C. Lin, and D. Xu, 2016: Comparison of the Impacts of Momentum Control Variables on High-Resolution Variational Data Assimilation and Precipitation Forecasting. *Mon. Wea. Rev.*, **144**, 149–169.

Sun, S., and Y. Xue, 2001: Implementing a new snow scheme in Simplified Simple Biosphere Model (SSiB), *Adv. Atmos. Sci.*, **18**, 335–354.

Sun, W., Z. Liu, D. Chen, P. Zhao, and M. Chen, 2020: Development and application of the WRFDA-Chem three-dimensional variational (3DVAR) system: aiming to improve air quality forecasting and diagnose model deficiencies. *Atmos. Chem. Phys.*, **20**, 9311–9329.

Tao, W.-K., and J. Simpson, 1993: The Goddard cumulus ensemble model. Part I: Model description. *Terr. Atmos. Oceanic Sci.*, **4**, 35–72.

Tao, W.-K,, J. Simpson, D. Baker, S. Braun, M.-D. Chou, B. Ferrier, D. Johnson, A. Khain, S. Lang, B. Lynn, C.-L. Shie, D. Starr, C.-H. Sui, Y. Wang, and P. Wetzel, 2003: Microphysics, radiation and surface processes in the Goddard Cumulus Ensemble (GCE) model. *Meteor. and Atmos. Phys.*, **82**, 97–137.

Tao, W.-K., J. Simpson, and M. McCumber 1989: An ice-water saturation adjustment, *Mon. Wea. Rev.*, **117**, 231–235.

Tao, W.-K., D. Wu, S. Lang, J.-D. Chern, C. Peters-Lidard, A. Fridlind, and T. Matsui (2016), High-resolution NU-WRF simulations of a deep convective-precipitation system during MC3E: Further improvements and comparisons between Goddard microphysics schemes and observations. *J. Geophys. Res. Atmos.*, **121**, 1278–1305, doi:10.1002/2015JD023986.

Tiedtke, M., 1989: A comprehensive mass flux scheme for cumulus parameterization in large–scale models. *Mon. Wea. Rev.*, **117**, 1779–1800. doi:10.1175/1520-0493(1989)117¡1779:ACMFSF¿2.0.CO;2.

Thompson, G., R. M. Rasmussen, and K. Manning, 2004: Explicit forecasts of winter precipitation using an improved bulk microphysics scheme. Part I: Description and sensitivity analysis. *Mon. Wea. Rev.*, **132**, 519–542.

Thompson, G., P. R. Field, R. M. Rasmussen, and W. D. Hall, 2008: Explicit Forecasts of Winter Precipitation Using an Improved Bulk Microphysics Scheme. Part II: Implementation of a New Snow Parameterization. *Mon. Wea. Rev.*, **136**, 5095–5115.

Thompson, G., and T. Eidhammer, 2014: A study of aerosol impacts on clouds and precipitation development in a large winter cyclone. *J. Atmos. Sci.*, **71**, 3636–3658.

Tong, W., G. Li, J. Sun, X. Tang and Y. Zhang, 2016: Design Strategies of an Hourly Update 3DVAR Data Assimilation System for Improved Convective Forecasting. *Weather and Forecasting*, **31**, 1673–1695.

Tsai, T.C. and J.P. Chen, 2020: Multi-moment ice bulk microphysics scheme with consideration for particle shape and apparent density. Part I: Methodology and idealized simulation. *J. Atmos. Sci.*, **77**, 1821–1850, doi:10.1175/JAS-D-19-0125.1.

Tsiringakis, A., Steeneveld, G. J., Holtslag, A. A. M., 2017: Small-scale orographic gravity wave drag in stable boundary layers and its impact on synoptic systems and near-surface meteorology, *Q. J. R. Meteorol. Soc.*, **143**, 704, https://doi.org/10.1002/qj.3021.

Vendrasco, E. P., J. Sun, D. L. Herdies, and C. F. de Angelis, 2016: Constraining a 3DVAR Radar Data Assimilation System with Large-Scale Analysis to Improve Short-Range Precipitation Forecasts. *J. Appl. Meteor. Climatol.*, **55**, 673–690.

Walko, R. L., W. R. Cotton, M. P. Meyers, and J. Y. Harrington, 1995: Newe RAMS cloud microphysics parameterization. Part I: The single-moment scheme. *Atmos. Res.,* **38**, 29–62.

Wang, H., Skamarock, W. C., Feingold, G., 2009: Evaluation of scalar advection schemes in the Advanced Research WRF model using large-eddy simulations of aerosol-cloud interactions. *Mon. Wea. Rev.*, **137**, 2547–2558.

Wang, H., J. Sun, S. Fan, and X.-Y. Huang, 2013: Indirect Assimilation of Radar Reflectivity with WRF 3D-Var and Its Impact on Prediction of Four Summertime Convective Events. *J. Appl. Meteor. Climatol.*, **52**, 889–902.

Wang, H., J. Sun, X. Zhang, X.-Y. Huang, and T. Auligne, 2013: Radar data assimilation with WRF 4D-Var: Part I. System development and preliminary testing. *Mon. Wea. Rev.*, **141**, 2224–2244.

Wang, S. and Z. Liu, 2019: A radar reflectivity operator with ice-phase hydrometeors for variational data assimilation (version 1.0) and its evaluation with real radar data. *Geosci. Model Dev.*, **12**, 4031–4051.

Wang, X., D. M. Barker, C. Snyder, and T. M. Hamill, 2008: A hybrid ETKF-3DVAR data assimilation scheme for the WRF model. Part I: Observing system simulation experiment. *Mon. Wea. Rev.*, **136**, 5116–5131.

Wang, X., D. M. Barker, C. Snyder, and T. M. Hamill, 2008: A Hybrid ETKF-3DVAR Data Assimilation Scheme for the WRF Model. Part II: Real Observation Experiments. *Mon. Wea. Rev.*, **136**, 5132–5147.

Wang, Y., Z. Liu, S. Yang, J. Min, L. Chen, Y. Chen, and T. Zhang, 2018: Added value of assimilating Himawari-8 AHI water vapor radiances on analyses and forecasts for "7.19" severe storm over north China. *J. Geophys. Res. Atmos.*, **123**, 3374–3394.

Webb, E. K., 1970: Profile relationships: The log-linear range, and extension to strong stability, *Quart. J. Roy. Meteor. Soc.*, **96**, 67–90.

Wicker, L. J. and W. C. Skamarock, 2002: Time splitting methods for elastic models using forward time schemes, *Mon. Wea. Rev.*, **130**, 2088–2097.

Wicker, L. J., and R. B. Wilhelmson, 1995: Simulation and analysis of tornado development and decay within a three-dimensional supercell thunderstorm. *J. Atmos. Sci.*, **52**, 2675–2703.

Wilson, T. H., and R. G. Fovell, 2018: Modeling the evolution and life cycle of radiative cold pools and fog. *Weather and Forecasting.* **33**, 203–220.

Wu, W. -S., R. J. Purser, and D. F. Parrish, 2002: Three-Dimensional Variational Analysis with Spatially Inhomogeneous Covariances. *Mon. Wea. Rev.*, **130**, 2905–2916.

Wu, Y., Z. Liu, and D. Li, 2020: Improving Forecasts of a Record-Breaking Rainstorm in Guangzhou by Assimilating Every 10-min AHI Radiances with WRF 4DVAR *Atmospheric Research*, **239**, 104912.

Xiao, H, S. Endo, M. Wong, W. C. Skamarock, J. B. Klemp, J. D. Fast, W. I. Gustafson Jr., A. M. Vogelmann, H. Wang, Y. Liu, 2015: Modifications to WRF's dynamical core to improve the treatment of moisture for large-eddy simulations. *J. Adv. Model Earth Syst.*, **7**, 1627–1642. (DOI: 10.1002/2015MS000532)

Xiao, Q. N., Y. H. Kuo, J. Sun, W. C. Lee, E. Lim, Y. R. Guo, and D. M. Barker, 2005: Assimilation of Doppler Radar Observations with a Regional 3D–Var System: Impact of Doppler Velocities on Forecasts of a Heavy Rainfall Case. *J. Appl. Met.*, **44(6)**, 768–788.

Xiao, Q., Ying-Hwa Kuo, Juanzhen Sun, Wen-Chau Lee, D. M. Barker, and Eunha Lim, 2007: An approach of radar reflectivity data assimilation and its assessment with the inland QPF of Typhoon Rusa (2002) at landfall. *J. Appl. Meteor. Climat.*, **46**, 14–22.

Xiao, Q., J. Sun, 2007: Multiple radar data assimilation and short-range quantitative precipitation forecasting of a squall line observed during IHOP 2002. *Mon. Wea. Rev.*, **135**, 3381–3404.

Xiao, Q., Eunha Lim, D.-J. Won, J. Sun, W.-C. Lee, M.-S. Lee, W.-J. Lee, J.-Y. Cjo, Y.-H. Kuo, D. M. Barker, D.-K. Lee, and H.-S. Lee, 2008: Doppler radar data assimilation in KMAs operational forecasting. *Bull. Amer. Meteor. Soc.*, **89**, 39–43.

Xiu, A. and J. E. Pleim, 2001: Development of a land surface model part I: Application in a mesoscale meteorology model. *J. Appl. Meteor.*, **40**, 192–209.

Xu, D., Z. Liu, X.-Y. Huang, J. Min, and H. Wang, 2013: Impact of Assimilating IASI Radiance Observations on Forecasts of Two Tropical Cyclones. *Meteorology and Atmospheric Physics*, **122**, 1–18.

Xu, D., Huang, X.-Y., Liu, Z., Min, J. 2014: Comparisons of Two Cloud Detection Schemes for Infrared Radiance Observations. *Atmospheric and Oceanic Science Letters*, **7(4)**, 358–363.

Xu, D., T. D. Auligne, and X. -Y. Huang, 2015: A validation of the multivariate and minimum residual method for cloud retrieval using radiance from multiple satellites. *Advances in Atmospheric Sciences*, **32**, 349–362.

Xu, D., T. D. Auligne, G. Descombes, and C. Snyder, 2016: A method for retrieving clouds with satellite infrared radiances using the particle filter. *Geosci. Model Dev.*, **9**, 3919–3932.

Xu, D., Z. Liu, S. Fan, M. Chen, and F. Shen, 2021: Assimilating all-sky infrared radiances from Himawari-8 using the 3DVar method for the prediction of a severe storm over North China. *Advances in Atmospheric Sciences*, **38**, 661–676.

Xu, M., Y. Liu, C. Davis and T. Warner, 2002: Sensitivity of nudging parameters on the performance of a mesoscale FDDA system: A case study. 15th Conference on Numerical Weather Prediction, 12-16 August, 2002, San Antonio, Texas, 127-130.

Xue, M., 2000: High-order monotonic numerical diffusion and smoothing. *Mon. Wea. Rev.*, **128**, 2853–2864.

Xue, Y., P. J. Sellers, J. L. Kinter, and J. Shukla, 1991: A simplified biosphere model for global climate studies. *J. Climate*, **4**, 345–364.

Yang, P., L. Bi, B.A. Baum, K.-N. Liou, G.W. Kattawar, M.I. Mishchenko, and B. Cole, 2013: Spectrally consistent scattering, absorption, and polarization properties of atmospheric ice crystals at wavelengths from 0.2 to 100 μm. *J. Atmos. Sci.*, **70**, 330–347, doi:10.1175/JAS-D-12-039.1

Yang, C., Z. Liu, J. Bresch, S.R.H. Rizvi, X.-Y. Huang, and J. Min, 2016: AMSR2 all-sky radiance assimilation and its impact on the analysis and forecast of Hurricane Sandy with a limited-area data assimilation system. *Tellus A*, **68**, 30917.

Yang, C., Z. Liu, F. Gao, P. P. Childs, and J. Min, 2017: Impact of assimilating GOES imager clear-sky radiance with a rapid refresh assimilation system for convection-permitting forecast over Mexico. *J. Geophys. Res. Atmos.*, **122**, 5472–5490.

Yang, Z.-L., G.-Y. Niu, K. E. Mitchell, F. Chen, M. B. Ek, M. Barlage, L. Longuevergne, K. Manning, D. Niyogi, M. Tewari, and Y. Xia, 2011: The community Noah land surface model with multiparameterization options (Noah-MP): 2. Evaluation over global river basins. *J. Geophys. Res.*, **116**, D12110.

Zalesak, S. T., 1979: Fully multidimensional flux-corrected transport algorithms for fluids. *J. Comp. Phys.*, **31**, 335–362.

Zhang, C,, Y. Wang, and Kevin Hamilton, 2011: Improved representation of boundary layer clouds over the southeast pacific in ARW–WRF using a modified Tiedtke cumulus parameterization scheme. *Mon. Wea. Rev.*, **139**, 3489–3513. doi:10.1175/MWR-D-10-05091.1.

Zhang, C. and Y. Wang, 2017: Projected Future Changes of Tropical Cyclone Activity over the Western North and South Pacific in a 20-km-Mesh Regional Climate Model. *J. Climate*, **30**, 5923-5941. doi:10.1175/JCLI-D-16-0597.1.

Zhang, C., Wang, Y., and Xue, M., 2020: Evaluation of an E–ϵ and Three Other Boundary Layer Parameterization Schemes in the WRF Model over the Southeast Pacific and the Southern Great Plains, *Mon. Wea. Rev.*, **148(3)**, 1121-1145. doi.org/10.1175/MWR-D-19-0084.1.

Zhang, D.-L., and R.A. Anthes, 1982: A high-resolution model of the planetary boundary layer–sensitivity tests and comparisons with SESAME–79 data. *J. Appl. Meteor.*, **21**, 1594–1609.

Zhang, G. J., and N. A. McFarlane, 1995: Sensitivity of climate simulations to the parameterization of cumulus convection in the Canadian Climate Centre general circulation model. *Atmos.–Ocean*, **33**, 407–446, doi:10.1080/07055900.1995.9649539

Zhang, X., X.-Y. Huang, and N. Pan., 2013: Development of the Upgraded Tangent Linear and Adjoint of the Weather Research and Forecasting (WRF) Model. *J. Atmos. Oceanic Technol.* **30**, 1180–1188.

Zhang, X., , X.-Y. Huang, J. Liu, J. Poterjoy, Y. Weng, F. Zhang, and H. Wang, 2014: Development of an Efficient Regional Four-Dimensional Variational Data Assimilation System for WRF. *J. Atmos. Oceanic Technol.*, **31**, 2777–2794.

Zhang, X.,Y.-H. Kuo, S.-Y. Chen, X.-Y. Huang, and L.F. Hsiao, 2014: Parallelization Strategies for the GPS Radio Occultation Data Assimilation with a Nonlocal Operator in the Weather Research and Forecasting Model. *J. Atmos. Oceanic Technol.*, **31**, 2008–2014.

Zhang, X., H. Wang, X.-Y. Huang, F. Gao, and N. A. Jacobs, 2015: Using Adjoint-Based Forecast Sensitivity Method to Evaluate TAMDAR Data Impacts on Regional Forecasts. *Adv. Meteorol.*, **2015**, doi:10.1155/2015/427616.

Zhang, X., Bao, J., Chen, B., and Grell, E., 2018: A Three-Dimensional Scale-Adaptive Turbulent Kinetic Energy Scheme in the WRF-ARW Model. *Mon. Wea. Rev.*, **146(7)**, 2023-2045, https://doi.org/10.1175/MWR-D-17-0356.1.

Zheng, Y., K. Alapaty, J.A. Herwehe, A.D. Del Genio, and D. Niyogi, 2016: Improving high-resolution weather forecasts using the Weather Research and Forecasting (WRF) Model with an updated Kain-Fritsch scheme. *Mon. Wea. Rev.*, **144**, 833-860.

Zilitinkevich, S. S., 1995: Non-local turbulent transport: pollution dispersion aspects of coherent structure of convective flows, *Air Pollution III* — Volume I. Air Pollution Theory and Simulation, Eds. H. Power, N. Moussiopoulos and C.A. Brebbia. Computational Mechanics Publications, Southampton Boston, 53–60.